UiT THE ARCTIC UNIVERSITY OF NORWAY

Department of Geosciences, Faculty of Science and Technology

Cryosphere-controlled methane release throughout the last glacial cycle

—

Pavel Serov

A dissertation for the degree of Philosophiae Doctor – December 2018

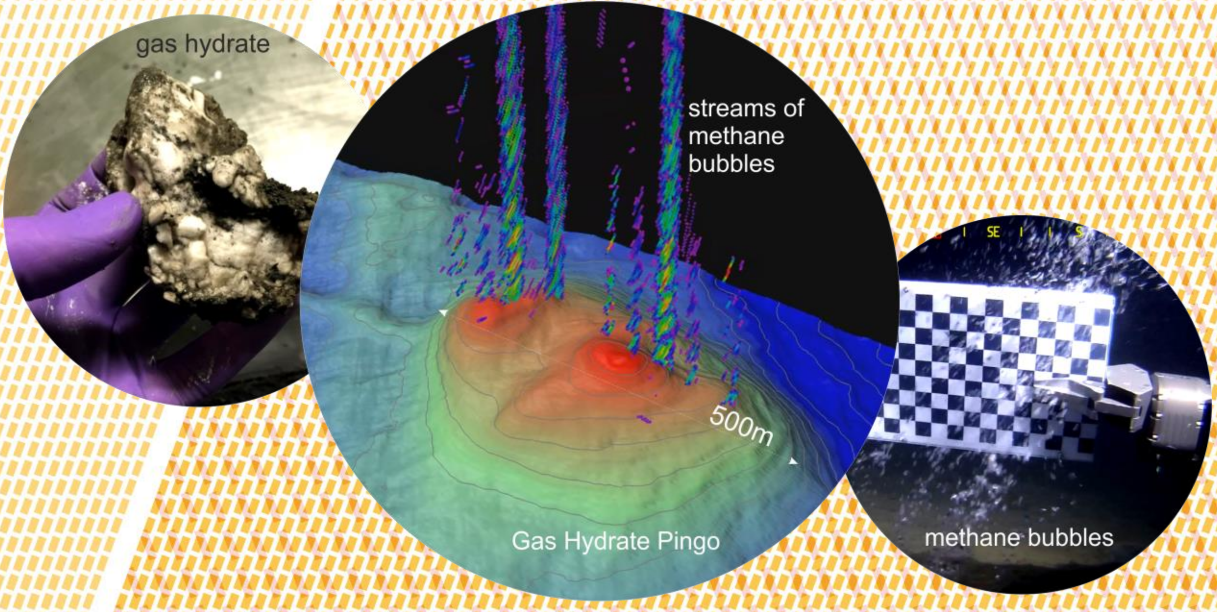

Table of Contents

Preface

The cryosphere of Arctic regions is undergoing rapid change due to century-scale global warming superimposed on millennial-scale natural climatic perturbations that started at the end of the last glacial cycle approximately 20,000 years ago [*Slaymaker and Kelly*, 2009]. The cryosphere refers to areas where low temperatures freeze water and form ice in the ocean (sea ice), on land (glaciers, permafrost, snow cover) and beneath the seabed (offshore permafrost) [*Harris and Murton*, 2005]. These areas may modulate release of greenhouse gases, such as methane and CO_2 into the atmosphere, both from the ocean through a barrier effect of sea ice, and also from land through a sealing effect of permafrost, glaciers and associated gas hydrates. Today's cryosphere shows rapid degradations in various regions of the Arctic, which may act as a climate change amplifier if outgassing of greenhouse gases from formerly stable gas hydrates and biogenic and thermogenic sources reaches the atmosphere [*Callaghan et al.*, 2011]. While gas hydrates are widely distributed within cryosphere, they are only stable under low temperature and high pressure conditions [*Ginsburg*, 1998]. Gas hydrate of natural gas is a crystalline water-based structure physically resembling ice and incorporating large concentrations of hydrocarbon gases (predominantly methane; 1 cm^3 of methane hydrate contains 150 cm^3 of methane) [*Sloan*, 2008]. With this in mind, the doctoral thesis focuses on gas hydrate dynamics in response to the degradation of the cryosphere across the Barents Sea and South Kara Sea continental shelves throughout the last 35,000 years. This doctoral thesis was undertaken at the Department of Geoscience, UiT – The Arctic University of Norway, Tromsø, from January 2015 to December 2018. The research was part of CAGE – Centre for Arctic Gas Hydrate, Environment and Climate funded by the Norwegian research council (grant 223259). CAGE and UiT provided full technical support in acquiring most of the data used in this thesis. Additionally, unique geological, geophysical and geochemical data from the South Kara Sea came from The All-Russian Research Institute of Geology and Mineral Resources of the World Ocean "VNIIOkeangelogia named after I.S. Gramberg".

During the four years of my doctoral education I participated in 10 research cruises onboard *RV Helmer Hanssen* (nine cruises, 2015-2018) and *RV Kronprins Haakon* (one cruise, 2018) to the northwestern and central Barents Sea for geological and water column sampling and collection of geophysical data (2D high-resolution seismic, P-cable 3D seismic, single- and multibeam echosounder). Participation in these cruises enabled both the collection of necessary multidisciplinary datasets that were used in this doctoral thesis and also the broadening of my understanding of subseafloor gas hydrate and fluid flow systems, the nature of seabed methane release, and the fate of methane in the water column. The collection of empirical data, which was later supported by advanced numerical modeling are deemed fundamental for the five research articles (four published and one manuscript) included in this doctoral thesis. Five evenly important research articles (2 published, 3 submitted) are not included in this thesis to keep the thesis focused. The results from this multidisciplinary research attracted attention in both the media and on seven international research conferences and workshops. Dissemination efforts of our research resulted in a number of publications in online and printed media sources, including ‘The Washington Post’ and ‘Nauka’ (in Russian).

This doctoral thesis is composed of an introduction and five research articles with short annotations revealing natural environmental changes controlling extensive seabed methane release across the Arctic Ocean Continental margins during the last ~35000 years.

RV Helmer Hanssen off Kvitøya Island (Arctic Ocean; 80.3° N, 31.8 ° E). Photo by Bjørn Runar Olsen

Supervisors

Prof. Karin Andreasson

CAGE – Centre for Arctic Gas Hydrate, Environment and Climate,
Department of Geosciences,
UiT – the Arctic University of Norway, Tromsø, Norway

Prof. Jürgen Mienert

CAGE – Centre for Arctic Gas Hydrate, Environment and Climate,
Department of Geosciences,
UiT – the Arctic University of Norway, Tromsø, Norway

Prof. JoLynn Carroll

Akvaplan-niva, FRAM – Hight North Research Centre
for Climate and the Environment, Tromsø, Norway

Department of Geosciences,
UiT – the Arctic University of Norway, Tromsø, Norway

Acknowledgements

First of all, I would like to thank my academic advisors, who made it possible for me to start and complete the PhD program. I was truly lucky to work with three excellent advisors without whom my education would not be as exciting and diverse as it was, or would not be possible at all. I would like to express my deep gratitude to Prof. Jürgen Mienert who supervised me from the first day of the PhD training and until the very last hour before this thesis was submitted. His unique way of thinking, creativity and incredibly deep understanding of nature guided me through my work. Prof. Jürgen Mienert believed in me even when I could not find reasons to believe in myself. Working with him was a great adventure that I will remember and be proud of. I would also thank Prof. Karin Andreassen, who accepted a challenge becoming my main supervisor at the last and the most critical year of the PhD project. Her energy and enthusiasm in research always admired me, while her solicitude and support helped me completing the last and the most difficult steps towards finishing this dissertation. Also, my research and education would not be possible without Prof. JoLynn Carroll who started this PhD project and guided my first steps in academia. She showed me a beauty of multidisciplinary approach in science, which I tried to implement throughout my work. These people made my development as a scientist possible.

I am grateful to Prof. Giuliana Panieri, who organized and leaded my first CAGE cruise onboard RV *Helmer Hanssen*, which became the most exciting research cruise I have ever had. I would also like to thank Prof. Stefan Bünz whose expertise helped me at different stage of this PhD project and at planning the future research.

I would like to thank crew of RV *Helmer Hanssen* and research engineers Steinar Iversen and Bjørn Runar Olsen who helped us collecting truly unique data. I will always remember RV *Helmer Hanssen* where I spent more than 100 days, where discoveries were made, and where new friendships started.

My PhD in Tromsø would not be possible without knowledge, experience and support of Dr. Boris Vanshtein and Prof. Georgy Cherkashov with whom I worked for 7 years. Dr. Boris Vanshtein took me to my first research cruise in the Arctic Ocean when I was 17 years old, after which I never doubted becoming a marine geologist.

I would like to thank my colleagues who helped me developing scientific articles – Alexey Portnov, Sunil Vadakkepuliyambatta, Henry Patton, Alun Hubbard, Calvin Shackleton and Anna Silyakova. I very much appreciate our large group of friends coming from all over the world to Northern Norway to work, explore the nature, ski, climb mountains and enjoy life: Alexey Pavlov, Alexey Portnov, Anna, Dasha, Calvin, Mariana, Giacomo, Kate, Carly, Arunima, Friederike, Emmelie, Sunny, Warren, Henry.

I owe an immeasurable gratitude to my family and friends from Russia who always supported me despite my work did not allow me spending as much time with them as they deserve.

Yet, my biggest acknowledgement goes to my partner, friend, colleague, ski companion and everlasting motivator – Malin Waage, who always inspires, supports, and loves.

List of Articles

1. Pavel Serov, Alexey Portnov, Jürgen Mienert, Petr Semenov, Polina Ilatovskaya (2015). **Methane release from pingo-like features across the South Kara Sea shelf, an area of thawing offshore permafrost**. *Journal of Geophysical Research: Earth Surface*. DOI: 10.1002/2015JF003467

2. Pavel Serov, Sunil Vadakkepuliyambatta, Jürgen Mienert, Henry Patton, Alexey Portnov, Anna Silyakova, Giuliana Panieri, Michael L. Carroll, JoLynn Carroll, Karin Andreassen, Alun Hubbard (2017). **Postglacial response of Arctic Ocean gas hydrates to climatic amelioration.** *Proceedings of the National Academy of Science of the United States of America (PNAS)*. DOI: 10.1073/pnas.1619288114

3. Karin Andreassen, Alun Hubbard, Monica Winsborrow, Henry Patton, Sunil Vadakkepuliyambatta, Andreia Plaza-Faverola, Eythor Gudlaugsson, Pavel Serov, Alexey Deryabin, Rune Mattingsdal, Jürgen Mienert, Stefan Bünz (2017). **Massive blow-out crater formed by hydrate-controlled methane expulsion from the Arctic seafloor.** *Science*. DOI: 10.1126/science.aal4500

4. Wei-Li Hong, Marta E. Torres, JoLynn Carroll, Antoine Crémière, Giuliana Panieri, and Pavel Serov (2017). **Seepage from an arctic shallow marine gas hydrate reservoir is insensitive to momentary ocean warming.** *Nature Communications.* DOI: 10.1038/ncomms15745

5. Pavel Serov, Henry Patton, Malin Waage, Calvin Shackleton, Jürgen Mienert, Karin Andreassen (manuscript) **Subglacial denudation of gas hydrate bearing sediments on an Arctic Ocean continental margin.**

1 Introduction

1.1 Scope

This doctoral thesis focuses on gas hydrate dynamics in response to the evolution of the cryosphere across the Barents Sea and South Kara Sea continental shelves throughout the last ~35,000 years until the 21st century. Within this time, our study sites, an area of relic subsea permafrost in the South Kara Sea, and a previously ice-sheet dominated region of the Barents Sea experienced significant climatic amelioration. It led to the ice-sheet retreat from the Barents Sea continental shelf and flooding of Arctic coast, e.g. Siberian coast bearing permafrost. The removal of the ice-sheet load from the Barents Sea shelf and flooding of permafrost on the South Kara Sea coast with water ~ 15 C° warmer than air triggered a destabilization of pressure and/or temperature sensitive gas hydrate and permafrost, and subsequently promoted the release of methane – this is a process that has far reaching consequences until today. There are several aspects of considerable interest relating to the research of cryosphere – controlled methane release:

1. **Scientific aspect**. While it is evident that terrestrial permafrost contains enormous amounts of carbon stored as organic matter, free gas and gas hydrates, the fate of relic subsea permafrost and its role in modulating seabed methane release across the various Arctic regions remains unclear. In light of recent discoveries of methane-related blow-out craters in thawing terrestrial permafrost on Yamal Peninsula close to the Kara Sea [*Moskvitch*, 2014], the continental shelf areas bearing its natural continuation might likewise experience abrupt release of methane caused by ocean warming and/or pressure changes [*Portnov et al.*, 2018]. Thus, observations of fluid/gas release within and from the seabed are important for reconstructing postglacial permafrost dynamics and associated methane release across the underexplored South Kara Sea shelf.

   In contrast, seabed expressions of past fluid release (pockmarks, craters, mounds, etc.) across the northwestern Barents Sea are better known due to hydrocarbon exploration in these regions. Despite common understanding that they result from vertical migration and seabed discharge of free gas, the mechanisms that produced the gas remains under discussion, since many of the pockmarks observed inactive today. The combination of an of ice-sheet evolution model with a gas hydrate model yields new insights on whether deglaciation caused wide spread gas hydrate dissociation and methane release resulting in abundant fluid escape features.
2. **Climate change aspect**. 21st century and future gradual ocean warming and short-term seasonal temperature changes may force dissociation of gas hydrates within a narrow (< ~10 m) water depth interval, contributing some amounts of greenhouse gas methane to the atmosphere, yet less than previously thought (~6 TG CH_4 yr^{-1} equal to ~1% of total annual flux from all

sources) [*Ruppel and Kessler*, 2017]. However, rapid depressurization due to Last Glacial Maximum ice-sheets retreat combined with ocean warming is a potentially stronger mechanism for gas hydrate decomposition on a longer time scale. This could cause release of gas hydrate bound methane at quantities and rates fundamentally different from what is observed today. Given that ice core carbon isotope records cannot distinguish gas hydrate methane from wetland methane (both are <60‰ $\delta^{13}C$ [*Chappellaz et al.*, 2013]) and δD records only indicate marine source of methane regardless whether it is related to hydrates or not [*Sowers*, 2006], the question about postglacial gas hydrate methane contribution to atmospheric budget remains open.

3. **Geotechnical aspect**. Decomposition of gas hydrates and thawing of permafrost may shape seafloor and change geotechnical properties of the sediments [*Nelson et al.*, 2001; *Sultan et al.*, 2004]. With a growing number of planned seabed constructions in polar regions (e.g. fiber cables, wind mills) it has become even more important to understand potential consequences of phase changes from ice and hydrate to water and gas within pore space of sediments. Studying seabed imprints of past gas hydrate decomposition and permafrost thaw may therefore yield insights into the extent and magnitude of seabed and subseabed deformations in areas of importance for seabed developments in the 21st century and beyond.
4. **Geohazard aspect**. Since 1 cm^3 of gas hydrates contains ~150 cm^3 of methane gas, the decomposition of gas hydrates in sediments can cause a rapid volume increase leading to gas accumulations with pressures significantly exceeding hydrostatic pressure. It is critical to identify the likely locations for these gas accumulations in order to reduce the risk for blow-outs during drilling operations. Moreover, over-pressured gas in pore spaces of sediments may compensate for part of the lithostatic stress and decrease strain of sediments leading to submarine mass movements.
5. **Biological aspect**. Seabed methane seeps are key energy sources for chemosynthesis based biological communities in deep water regions devoid of sun light [*Levin et al.*, 2016]. Recent studies of arctic cold seeps showed appreciable increases in the abundance and diversity of infaunal and megafaunal species compared to surrounding areas without seeps [*Åström et al.*, 2018]. In deep-water regions of the continental margins, depletion of conventional food sources may urge conventional heterotrophs to capitalize on the rich biomass of chemosynthesis based ecosystems. Thus, the occurrence of wide-spread seeps across the Barents Sea shelf can play a major role in benthic biological community distributions.

1.2 Key concepts and definitions

Arctic continental margins contain large amount of hydrocarbons [*Gautier et al.*, 2009] and organic matter [*Bröder et al.*, 2018] genuinely fueling seepage of thermogenic and biogenic gas [*Ruppel and Kessler*, 2017]. Thermogenic hydrocarbons (e.g. **thermogenic methane**) form due to thermal cracking of organic molecules (kerogen) at a temperature of > 60 °C and depth of > 1.5 km. In contrast, **biogenic methane** is a result of organic matter decomposition through metabolic activity of methanogenic microbial communities in shallower subsurfaces (<1 km) [*Inagaki et al.*, 2006]. Since it is not related to substantial burial and high temperatures, biogenic methane generation implies a comparatively rapid turnover of organic matter. Reported ages of biogenic methane are often <1000 years, while the youngest thermogenic hydrocarbon source rocks are of Neogene Age (> 2.6 million years old).

Regardless of its origin, methane may migrate through cracks and effective porosity in lithified rocks or unconsolidated sediments as free gas or in dissolved phase. Diffusion is deemed comparatively inefficient in transporting methane over large areas and forming any substantial accumulations [*Judd and Hovland*, 2009]. Advective methane flow driven by buoyance force and pressure gradients tends to reach higher hypsometric levels and may eventually expel at the seafloor. Noteworthy, across continental margins, the ascending flux of dissolved methane experiences sufficient reduction due to anaerobic oxidation in bottom sediments [*Boetius et al.*, 2000]. **Anaerobic oxidation of methane (AOM)** is a process of methane oxidation with different electron acceptors (most commonly sulfate) in anoxic marine or freshwater conditions. Methane oxidation is coupled with sulfate reduction through a consortium of methanotrophic archaea and sulfate-reducing bacteria [*Boetius et al.,* 2000]. Their symbiosis causes specific biogeochemical interface called **sulfate-methane transition zone** where sediment pore water sulfate infiltrating from sweater and methane migrating from deeper sediments experience coupled reduction. 80-90 % of the upward diffusive methane flux (400 Tg CH_4 y^{-1} estimated globally) oxidizes anaerobically [*Reeburgh*, 2007].

Beyond this strong microbiological methane filter, geological structures impermeable for fluids constitute physical barriers retaining dissolved and gaseous methane. Similar to geological seals, subsea permafrost and gas hydrates have the potential to limit vertical methane flux [*Archer*, 2015; *Dickens et al.*, 1997] with one fundamental difference: they are particularly sensitive to environmental conditions such as pressure and temperature and may rapidly form or degrade .

Subsea permafrost – submerged grounds/sediments that remain below freezing point for two or more consecutive years. Subsea permafrost may form on the continental shelves of polar regions during episodes of sea-level lowstands and low-temperature exposure, or in subsea conditions in response to negative mean annual bottom temperatures. Frozen deposits are less permeable [*Yakushev and Chuvilin*, 2000] or impermeable [*Shakhova et al.*, 2010] for fluids acting as a seal and isolate organic matter within its frozen framework. Thawing of permafrost uncaps the fluid flow and liberates organic matter supporting methanogenesis. Low temperatures within subsea permafrost may sustain gas hydrates in low-pressure conditions of shallow shelves and onshore.

Gas hydrates of natural gas – crystalline solids consisting of methane and its heavier homologs (e.g. ethane, propane) trapped in a lattice of hydrogen-bonded molecules of water. Under stable – low temperature, high pressure – conditions, gas hydrates act as an efficient methane sink (1 cm^3 of methane hydrate contains ~150 cm^3 of gas). If hydrate-bearing sediments abandon the gas hydrate stability envelop, hydrates dissociate releasing free gas. Gas hydrates are widely distributed on continental slopes, overdeepened shelfs and in subsea and terrestrial permafrost (intra-permafrost gas hydrates). Grounded ice-sheets feature another strong control on gas hydrate distribution. Loading of ice provides high pressure which along with low basal temperatures generates a **subglacial gas hydrate stability zone** [*Portnov et al.*, 2016; *Wadham et al.*, 2012]. Upon ice-sheet retreat, subglacial gas hydrates may be outside the gas hydrate stability zone (GHSZ) and dissociate releasing methane from the seabed [*Long et al.*, 1998].

The area of the seafloor with enhanced concentrations of methane surrounding a vent of methane bubbles is called a **methane seep**. At seep sites, methane and hydrogen sulfide – a product of AOM – is an energy source supporting specific seafloor ecosystems [*Ruff et al.*, 2015]. Another byproduct of AOM – bicarbonate may facilitate precipitation of methane-derived authigenic carbonates. Paragenesis of authigenic carbonates and chemosymbiotic fauna (Figure 1) is a strong indicator of present or paleo methane rich environments.

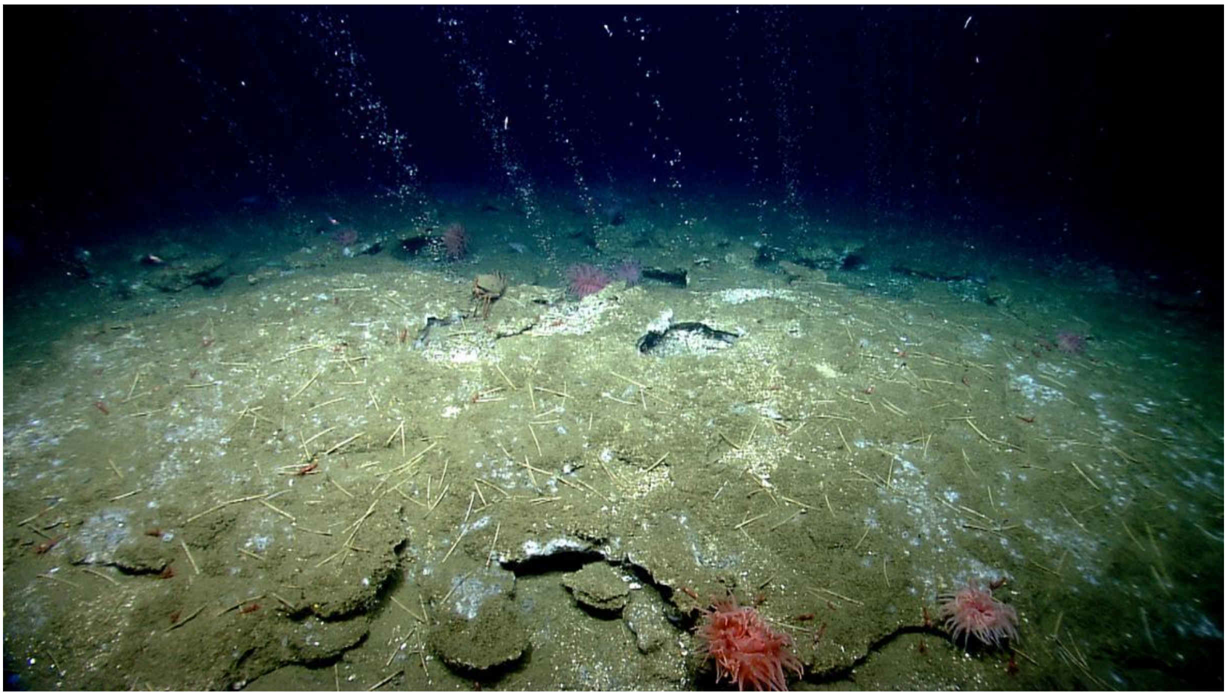

Figure 1 – Release of methane gas and surrounding pavements of authigenic carbonates offshore Virginia, Atlantic Ocean. Image by NOAA Okeanos Explorer program, 2013 Northeast U.S. Expedition.Public domain.

Fluid flow and gas hydrate dynamics cause origination of specific seafloor structures, such as pockmarks, mud volcanoes, gas hydrate pingos, craters, etc. The latter is suggested to be a manifestation of blow out methane discharge tracing collapse of Arctic gas hydrate and permafrost systems [*Kizyakov et al.*, 2017; *Long et al.*, 1998; *Moskvitch*, 2014].

Gas hydrate pingos – seafloor mounds composed of deposits containing substantial quantities of gas hydrates and capping a strong methane inflow (Figure 2). Seep related authigenic carbonates and permafrost may contribute to solid content of gas hydrate pingos (GHPs). GHPs are suggested to originate due to one or combination of following: frost heaving, gas hydrate heaving, volume expansion when hydrates decompose and extrusion by overpressured gas accumulations [*Koch et al.*, 2015; *Paull et al.*, 2007; *Serié et al.*, 2012].

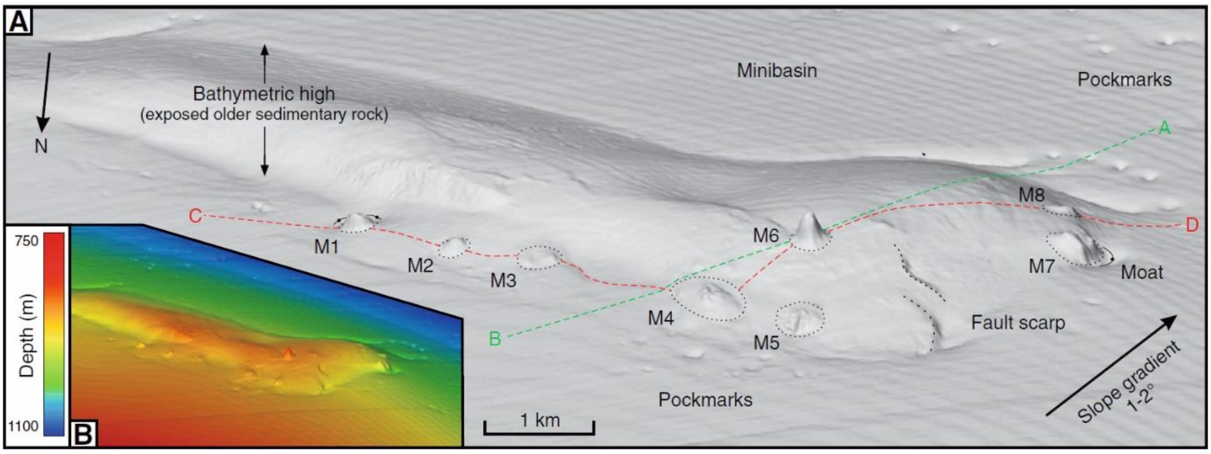

Figure 2 – Gas hydrate pingos (M1 – M8) on shaded relief map (A) and bathymetric map (B) in the Kwanza Basin, offshore Angola [*Serié et al.*, 2012].

Seafloor craters – spherical depressions cut in the seafloor with steep walls (up to 45°) and diameter typically exceeding 500 m. Compared to pockmarks, craters are larger, deeper and may develop in lithified rocks [*Long et al.*, 1998]. The natural craters are hypothesized to originate due to blow outs of fluids analogous to the features formed due to human-caused blow-out accidents during drilling operations (Figure 3) [*Leifer and Judd*, 2015].

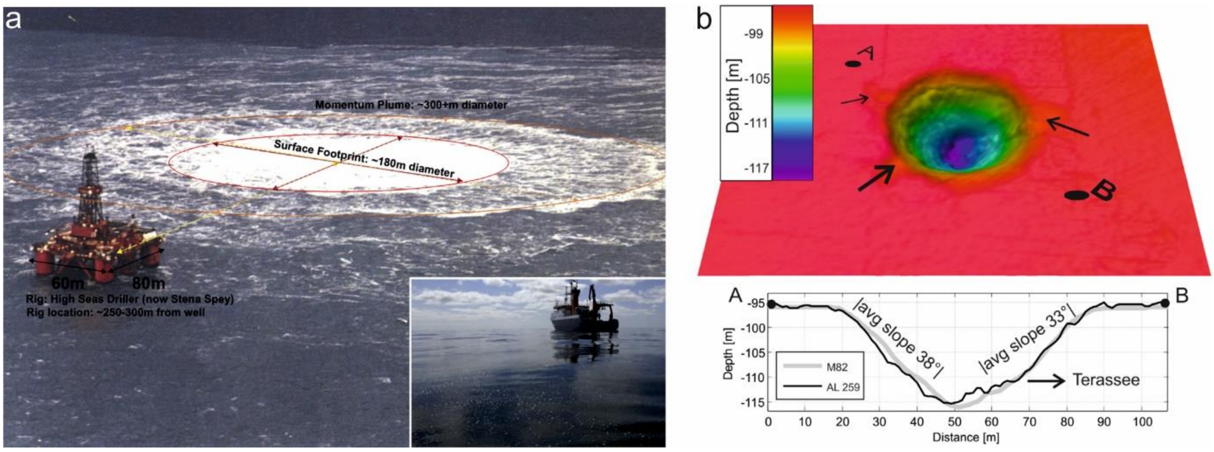

Figure 3 - Blowout at 22/4b well in the North Sea, November 1990 (modified after *Leifer and Judd* [2015] and *Schneider von Deimling et al.* [2015]). a - surface expression of a gas plume. Insert shows gas bubbles observed on the sea surface at 22/4b site during a research cruise in 2005 [*Leifer and Judd*, 2015]; b – gridded multibeam bathymetry data and a topographic profile showing 20 m deep crater formed at the site [*Schneider von Deimling et al.*, 2015].

1.3 Evolution of the cryosphere on the Barents Sea shelf and the Kara Sea shelf from the Last Glacial Maximum to the 21st Century

The Last Glacial Maximum (LGM) is the most recent period in Earth history when global ice-sheet volume reached its maximum values and associated global sea-level its minimum with ~120 m fall. Starting at 33,000 years BP a combined effect of decreases in northern summer insolation, atmospheric CO_2, and sea surface temperature in tropical regions of the Pacific Ocean provoked growth of the ice-sheets to their maximum configurations [*Mix et al.*, 2001]. The maximum extent of ice-sheets across the globe occurred between 26,500 and 19,000 years BP sustained by comparatively stable climate for ~7,500 years [*Clark et al.*, 2009]. ~19,000 years BP orbitally induced increase in insulation triggered a suite of feedbacks (greenhouse gas, sea-level, ice albedo, and wind feedbacks) triggering global nearly synchronous deglaciation [*Alley and Clark*, 1999].

During the LGM the Barents Sea and western parts of the Kara Sea were covered by a marine-based Barents Sea Ice-sheet, which was a part of the Eurasian ice-sheet complex [*Jakobsson et al.*, 2014; *Patton et al.*, 2016]. At its maximum configuration the ice-sheet reached the shelf break on the western and northern margins of the Barents Sea, but it was terminated at and did not reach across the South Kara Sea. Towards the south it joined the terrestrial-based Fennoscandian Ice-sheet (Figure 4).

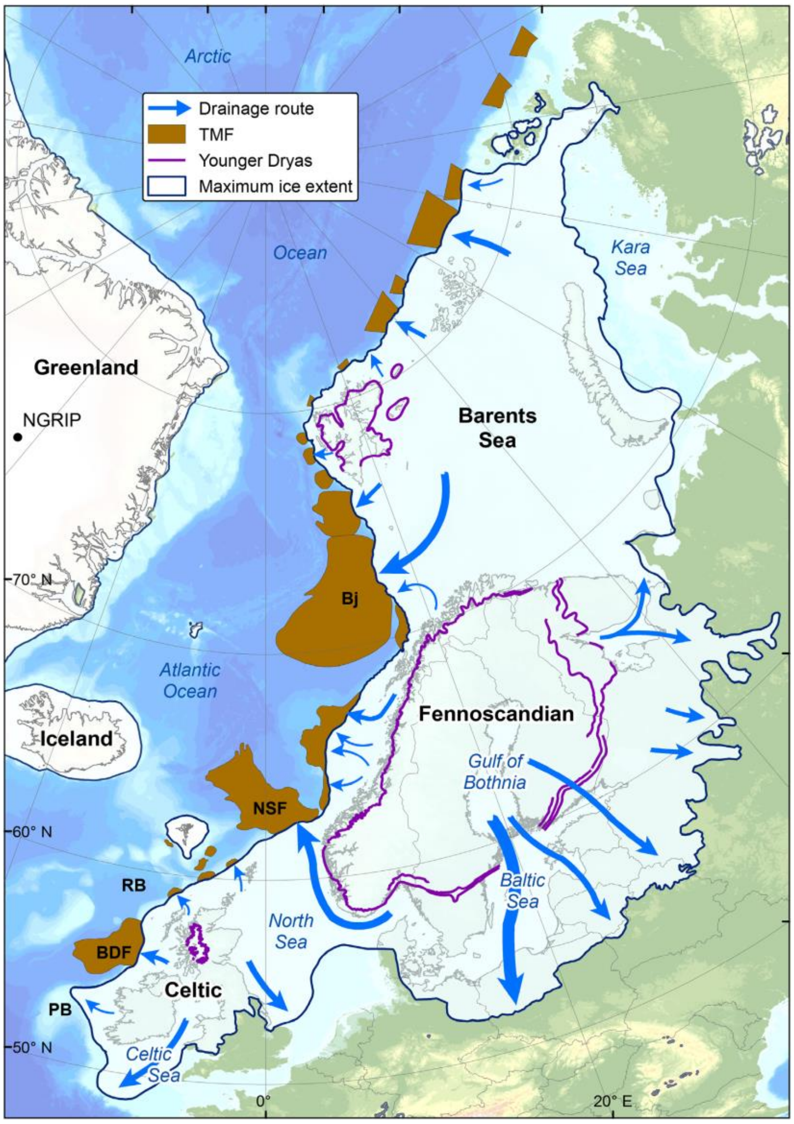

Figure 4 – Maximum ice-sheet extent of the Barents Sea and Fennoscandian Ice-sheets and their major drainage pathways [*Patton et al.*, 2017].

The Barents Sea Ice-sheet at its LGM configuration reached >2 km thickness and substantially loaded the underlying lithosphere [*Patton et al.*, 2016]. Subsequent decay of the ice-sheet caused isostatic rebound [*Siegert et al.*, 2001] locally outpacing sea-level change [*Wallmann et al.*, 2018]. This may have an important implication for the stability of shallow submarine gas hydrates as well as deep hydrocarbon gas accumulations. Numerical modeling of isostatic adjustments of the Barents Sea shelf coupled with sea level curves reveal substantial shallowing of vast areas of the Barents Sea shelf (Figure 5) [*Patton et al.*, 2016]. A significant decrease of water depth (pressure) may cause a thinning of GHSZ, and destabilization of gas hydrates at its base. Noteworthy, the central part of the Barents Sea experienced a decrease in water depth from > 400 m to < 300 m that caused a complete disappearance of gas hydrate reservoirs accompanied by extensive seabed methane release.

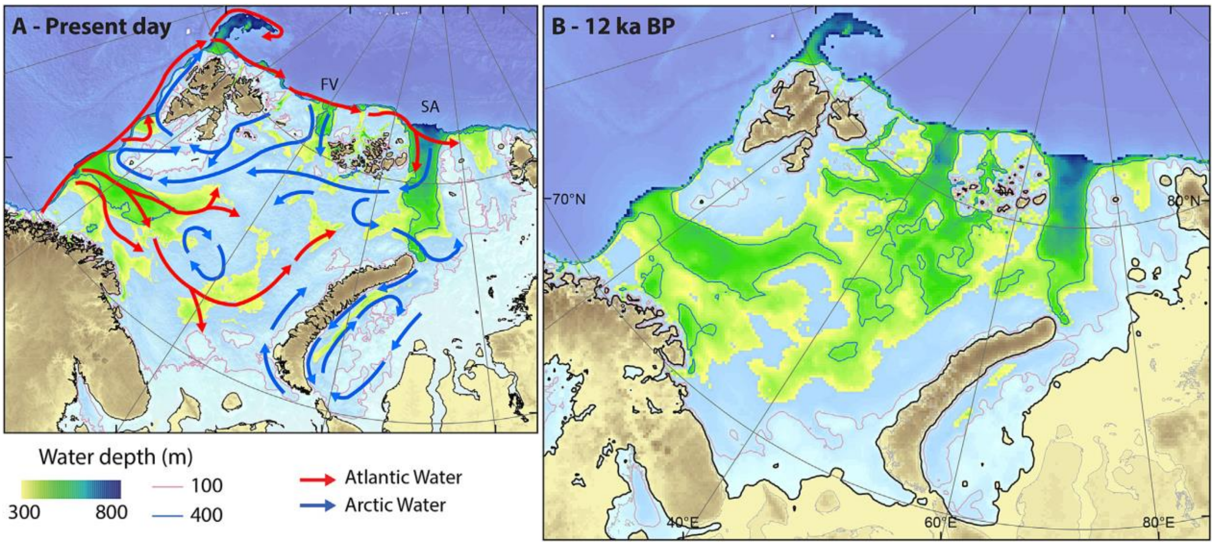

Figure 5 – seabed topography change due to isostatic rebound of the Barents Sea shelf [*Patton et al.*, 2017].

During the LGM, the South Kara Sea was located on a margin of the Barents Sea Ice-sheet with ice thickness < 500 m. Therefore, it only experienced minor isostatic adjustments. The local sea-level here is dominated by global sea-level trends (Figure 6). Due to the LGM sea-level lowstand the Kara Sea coastline was located at the present day ~120 m isobath. Its shelf seas, which now experience <120 m of water depth were exposed to air with a mean annual air temperatures of < -15 °C.

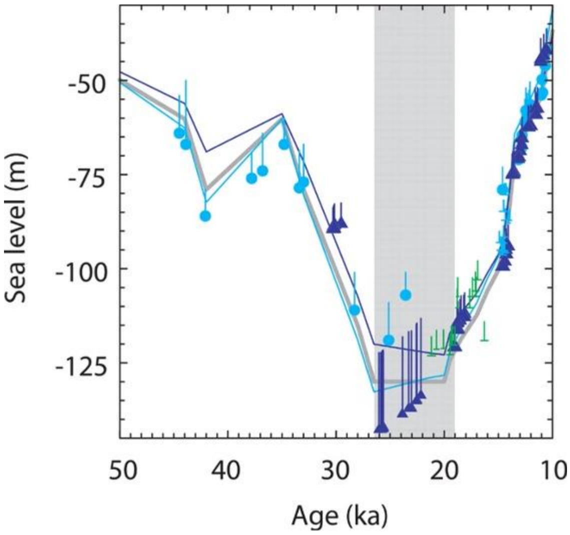

Figure 6 – Global sea-level predictions (lines) and relative sea-level data (dots) for New Guinea (light blue) and Barbados (dark blue). Grey line indicates eustatic sea-level time series [*Clark et al.*, 2009].

1.4 Three study regions

This thesis focuses on four geographical regions demonstrating methane release, which were directly or indirectly affected by the last glaciation. Study areas 1 and 2 (Article 1) are located outside the LGM limits of the Barents Sea Ice-sheet within shallow water (40-80 m water depth) of the Yamal Shelf at the South Kara Sea (Figure 7). During the glaciation, the shallow shelves of the Arctic Ocean, including Yamal Shelf emerged, were subaerial and experienced freezing under mean annual temperatures as low as -15 °C. In contrast, our study sites 3 and 4 (Articles 2-5) were covered by > 1500 m thick grounded Barents Sea Ice-sheet (Figure 4), which insulated the lithosphere and provided substantial loading. High pressure conditions under the ice-sheet and low temperature permafrost conditions outside it are favorable for increasing gas hydrate stability and methane sequestration. Yet, depending on different phases of the cryosphere development related to thickness and temperature such methane inventories may have experienced non-synchronous dissociation driven by the large-scale natural climatic amelioration that started ~20,000 years BP.

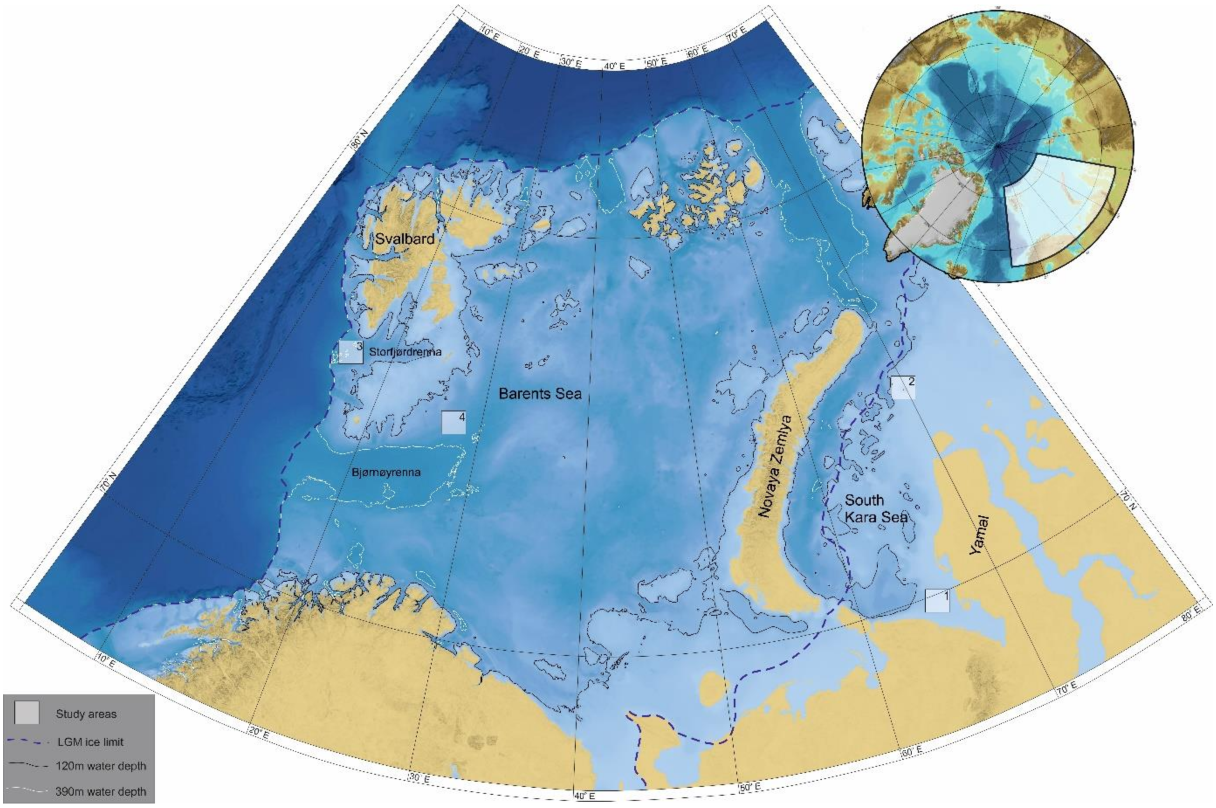

Figure 7 – Location of the study areas in relation to limits of the LGM Barents Sea Ice-sheet, 120m isobath marking the maximum seaward limit of relic subsea permafrost, and 390m isobaths indicating tentative shallow termination of methane hydrate stability zone [*Jakobsson et al.*, 2012].

1.4.1 Yamal Shelf (South Kara Sea)

The shallow (<120 m water depth) shelf offshore Yamal Peninsula is 100 – 120 km wide and does not demonstrate any significant seafloor relief. Considering the low gradients even minor sea-level fluctuations will cause large-scale advances or retreats of the shoreline. Existing eustatic sea level curves reveal that distal parts of shelf that are deeper than 55 m were exposed and thus experienced freezing for minimum ~22,000 years, while shallower areas experienced freezing for as long as ~65,000 years (Figure 8). Ice-sheet modeling and empirical observations suggest insignificant glacio-isostatic movement along the Yamal coastlines indicating minimal deviations from the global sea-level trend (Figure 8).

During periods of shelf exposure, the low mean annual air temperatures provoked growth of up to ~300 m thick permafrost that partly exists until today [*Yakushev and Chuvilin*, 2000]. Coastal inundation started ~19.000 years BP causing a >10 ºC warming of the seafloor initiating thawing of relic permafrost. Current state of relic subsea permafrost in the South Kara Sea is still controversial. Modeling studies by *Portnov et al.* [2014] suggest a range of possible rates of permafrost retreat and propose the most likely scenario of present seaward limit of continuous permafrost at c. 20 m water depth. Notably, the seabed methane release sites concentrate in the region deeper than 20 m water depth (Figure 9). In contrast, mapping of acoustic signatures of permafrost suggest that subsea permafrost extends to 60 m water depth [*Rekant and Vasiliev*, 2011]. Drilling data reveal occasional subsea permafrost at 0 – 130 m water depths. Contradictions between modeling, direct and indirect empirical observations may point towards a heterogenous state of subsea permafrost in different areas of the Yamal Shelf causing a patchy distribution.

Beneath the South Kara Sea exists a 7-10 km thick Mesozoic and upper Cenozoic sedimentary basin containing source rocks analogous to West Siberian petroleum province [*Stupakova*, 2011]. Yamal peninsula adjacent to our offshore study sites 1 and 2 hosts 26 gas, gas condensate and oil fields [*Grama*, 2012]. In these offshore areas conventional seismic data show numerous prospective structures with a potential for gas and gas condensate.

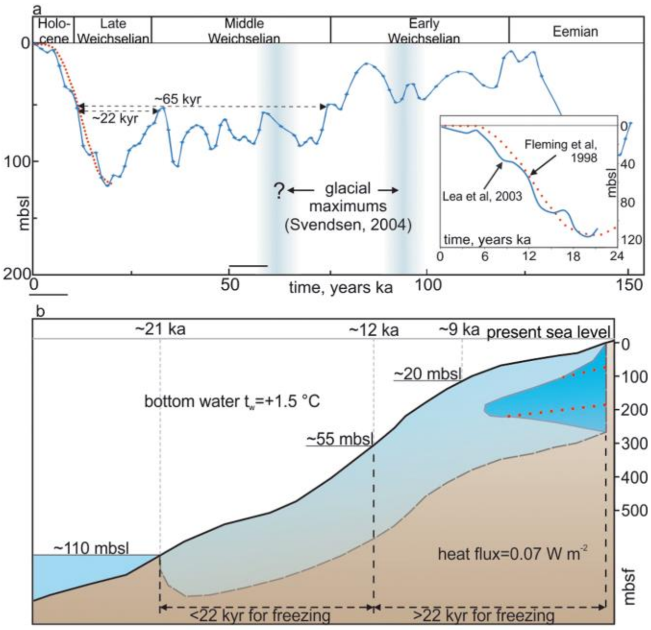

Figure 8 – (a) Eustatic sea level curves defining exposure time of the Yamal Shelf [*Fleming et al.*, 1998; *Lea et al.*, 2003]. (b) Modeled extent of permafrost during the LGM sea level lowstand (light blue) and today (dark blue) [*Portnov et al.*, 2014].

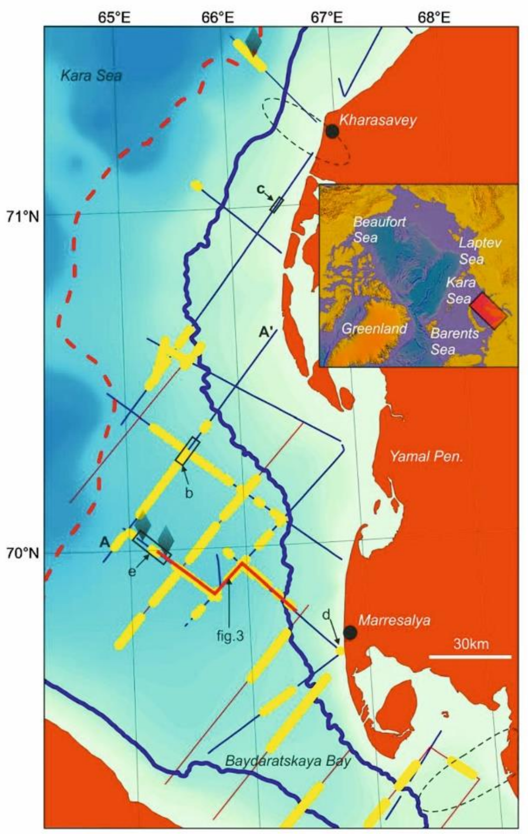

Figure 9 – Hydro-acoustic anomalies on Yamal shelf (yellow lines) concentrating in water depth deeper than 20 m (shown in blue). Black lines show locations of survey lines [*Portnov et al.*, 2013].

1.4.2 Storfjorden Trough (Barents Sea)

Our study site in Storfjorden Trough (Storfjordrenna) shows a specific geological character with a cluster of gas hydrate pingos leaking free gas into the water column (Articles 2, 4, 5). It is located ~50 km southward from Svalbard and ~35 km westward from the shelf break of the Barents Sea. Storfjorden trough is the second largest in the western Barents Sea and was developed by dynamic ice stream draining substantial portions of the Barents Sea Ice-sheet during the last glaciation. Today's seabed of the trough demonstrates a series of grounding zone wedges each reflecting an episode of ice stream standstill during deglaciation. The trough terminates with a large trough mouth fan – a pronounced sediment depocenter on the continental slope. Ice-sheet modeling suggests that our study site was covered by grounded ice up to 2 km in thickness from ~33,000 to ~19,000 years BP [*Patton et al.*, 2017]. After the deglaciation, relaxation of underlying lithosphere resulted in glacioisotatic adjustments that are still ongoing until today [*Auriac et al.*, 2016].

The trough itself shows a thin (< 4 m) veneer of Holocene and postglacial marine muds [*Rasmussen et al.*, 2007] overlying ~100 m thick glacial till. The tills are lying with a distinct angular unconformity (so-called Upper Regional Unconformity - URU) on lithified bedrocks of variable age and origin [*Bergh and Grogan*, 2003]. Within our ~25 km^2 study region the glacial unit is remarkably thin and overlies rotated basement blocks of Paleogene age [*Lasabuda et al.*, 2018]. Here, we observe characteristic and wide-spread seismic indications of free gas accumulations. An array of listric faults suggests an extensional tectonic regime that very likely relates to the Hornsund Fault Zone Complex marking a transition zone between continental and oceanic crust along the western Svalbard margin [*Anell et al.*, 2016].

A distinct field of gas hydrate pingos exists on an elongated topographic depression hosting (< ~ 50 m) GHSZ. Along the western Svalbard margin >1200 methane seeps have been mapped close to termination of the GHSZ, yet the majority of them is restricted to bathymetric highs in between glacial troughs [*Mau et al.*, 2017]. Despite the inferred shallow gas hydrate accumulations along the western Svalbard margin, previous sampling attempts (drilling and gravity coring) to recover gas hydrates were unsuccessful. Our study site in Storfjorden trough was the first one with recovered gas hydrates on the shelf surrounding Svalbard.

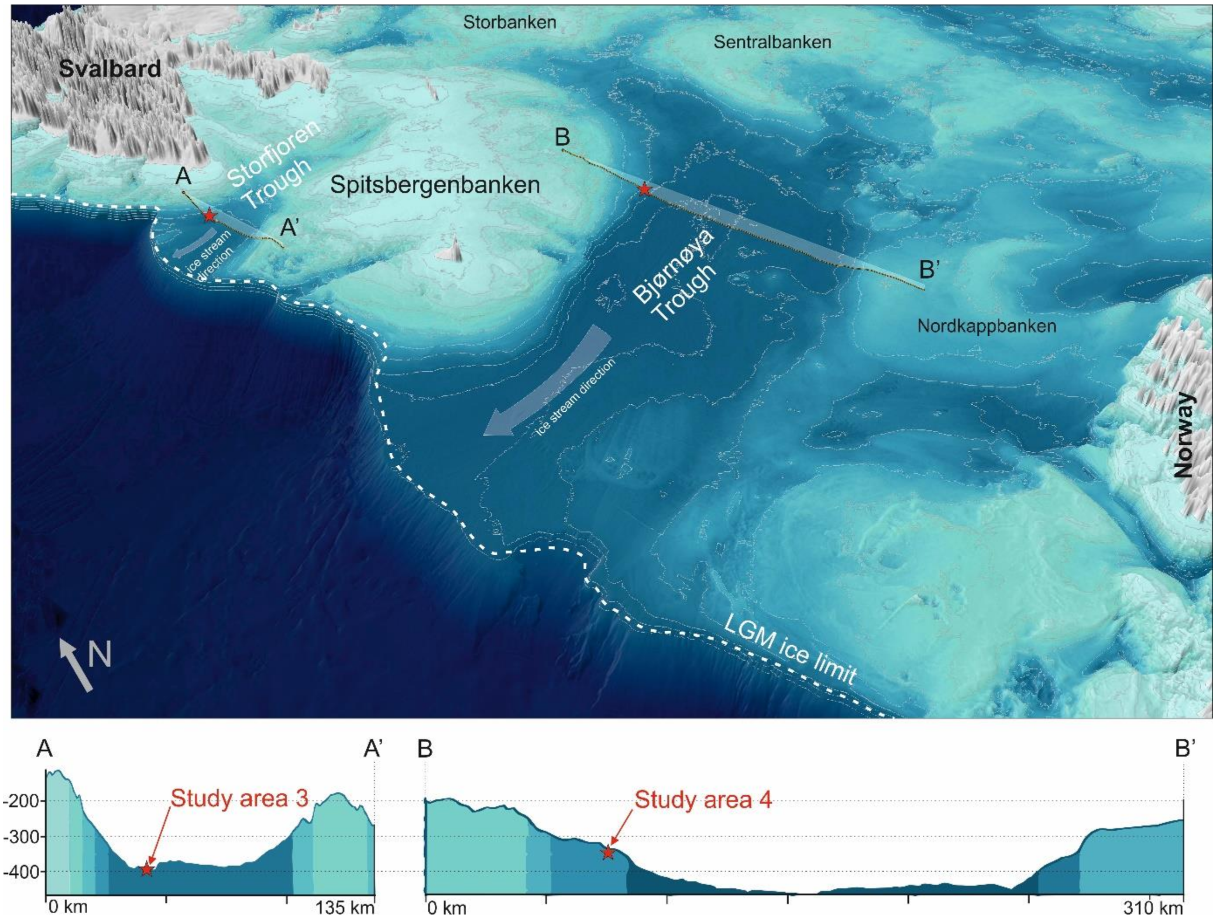

Figure 10 - Seabed topography of the western Barents Sea margin with location of study areas 3 in Storfjorden trough and study area 4 in Bjørnøya trough [*Jakobsson et al.*, 2012].

1.4.3 Bjørnøya Trough (Barents Sea)

Study area 4 (Article 3) stretches along a flank of Bjørnøya Trough (Bjørnøyrenna) – the largest glacially eroded trough crosscutting the Barents Sea shelf from east to west (Figure 10). This study region comprises >100 seabed craters that occur 350 km eastward from the shelf break and c. 200 km distance from Bjørnøya (Bear Island). The sediment blanket is thin [*Long et al.*, 1998] and the thickness of Holocene soft sediments varies from 0 - 30 cm at the study site. Moreover, the glacigenic sediment unit is essentially missing but outcrops of lithified shales/fine-grained sandstones mark the seabed [*Long et al.*, 1998].

The glacial geomorphology of the trough reveals several grounding zone wedges to the west from the study site marking episodes of decreased ice dynamics during the ice stream retreat [*Winsborrow et al.*, 2010]. Our study site does not show elements of mega-scale glacial geomorphology (streamlined landforms, sediment wedges, etc.), yet reveals numerous ice scouring ploughmarks. Ploughmarks formed by iceberg activity proximal to retreating ice stream front may provide important insights into the age of the craters.

The Barents Sea experienced extensive Cenozoic erosion that removed up to 3 km of sedimentary strata [*Laberg et al.*, 2012]. Within our study area the glacial erosion has reached down to a series of clinoform structures of Middle-Triassic age. It is known from offshore drilling and outcrops on Svalbard that such clinoforms contain topsets of sandstone and bottomsets of organic-rich fine-grained material [*Høy and Lundschien*, 2011; *Lundschien et al.*, 2014]. Seismic surveys indicated offsets of reflectors within bedrocks pointing towards faulting below the craters [*Andreassen et al.*, 2017]. Therefore, within our study area 4 we anticipate that several crucial components exists for a hydrocarbon leakage system: potential organic-rich source rocks coarsening upwards, disrupted by faults supporting fluid advection. Yet, before our investigations in 2014-2016 seabed fluid release has not been studied in detail. Moreover, the quality of 2D seismic data did not allow documenting subseabed fluid flow, which has now been much improved due to our high-resolution P-Cable 3D seismic survey. *Long et al.* [1998] were only able to hypothesize that craters might have formed due to rapid dissociation of gas hydrates and methane release following ice-sheet retreat during the last deglaciation. Though a hypothesis was postulated, a confirmation of fluid flow systems in the area with integrated modeling of the LGM ice-sheet and gas hydrate evolution were still missing.

Our recent comprehensive ice-sheet modeling suggests that the study area in Bjørnøya trough hosted an ice stream up to 2 km thick from at least 30,000 to 16,000 years ago [*Patton et al.*, 2017]. Outcomes of this model including transient ice-sheet thickness, basal thermal regime and isostatic adjustments of underlying lithosphere provide a solid base to develop a coupled gas hydrate evolution model to investigate the history of methane capture and release in the Bjørnøya trough crater field from the LGM to the 21th Century. Considering present bottom water temperatures, the crater field is mostly lying outside of theoretical methane hydrate stability zone [*Vadakkepuliyambatta et al.*, 2017].

Study area 3 and 4 experienced different histories of pressure and temperature perturbations related to the latest glaciation-deglaciation. Study area 3 lies in the outer part of Storfjorden trough which was deglaciated ~5,000 years earlier if compared to study area 4 located in central part of the LGM ice-sheet (Figures 7, 10). The Storfjorden trough bears a nearly complete LGM – Holocene sediment record that are missing in Bjørnøya trough where lithified bedrocks outcrop on the seabed. Today, a pressure-temperature envelop of methane hydrate stability characterizes the gas hydrate pingo region, but it does not exist anymore in the crater field. Clearly, the seabed structures with the study regions 3 and 4 are very different: while gas hydrate bearing pingos of soft muds exist in area 3, craters and mounds of lithified bedrocks without confirmed gas hydrates exist in area 4.

1.5 Cryosphere-controlled methane capacitors and climate change

Remarkable temperature changes (up to 8 °C [*Alley*, 2000]) during the glacial-interglacial transitions (as indicated by deuterium content of ice) cannot be quantitatively explained by insolation forcing alone [*Brook*, 2005]. With growing numbers of atmospheric gas records from ice core samples covering the past 650,000 years it became clear that climate and greenhouse gas cycles are related and the latter contribute ~40% to the radiative forcing (Figure 11).

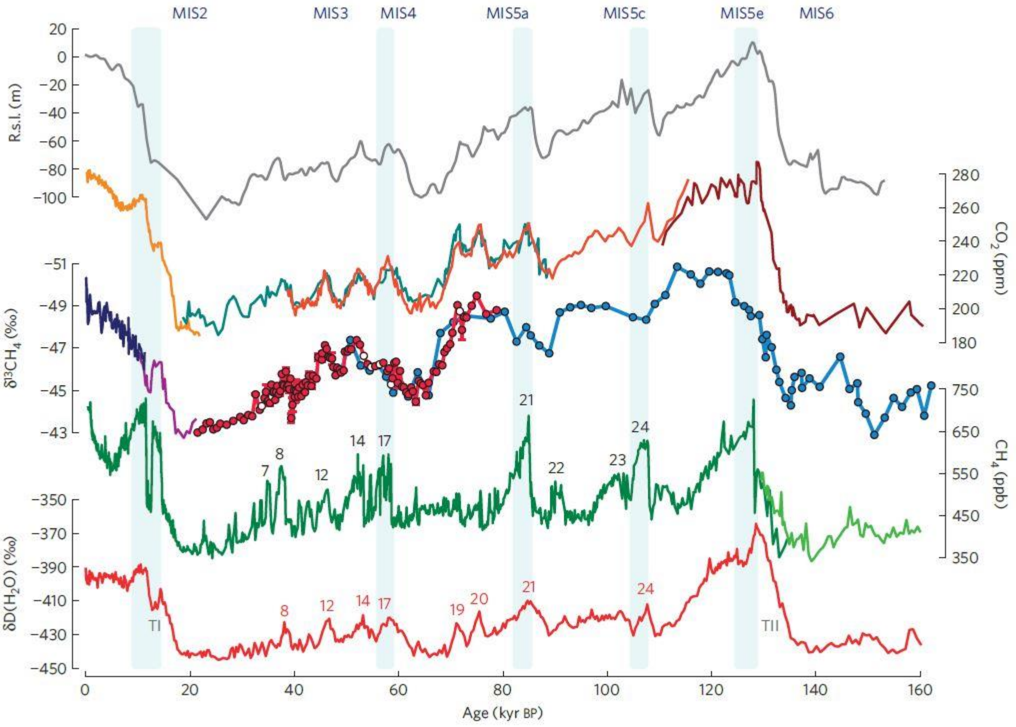

Figure 11 – δD H_2O, methane, $\delta^{13}CH_4$ and carbon dioxide records [*Moller et al.*, 2013]. Ice cores from Vostok, EDML, Talos Dome, Byrd, EPICA Dome C and GISP2 are used for composed curves.

Carbon dioxide and methane have a special relevance to greenhouse gas driven climate warming [*Pachauri et al.*, 2014]. CO_2 is the largest contributor to the radiative effect (its modern atmospheric concentration is ~400 ppm), while CH_4 is the most potent greenhouse gas despite its concentration in the atmosphere is ~220 times less [*Stocker*, 2014]. Over a 20-year period, one mass unit of CH_4 has 84 times higher impact on the radiative warming than CO_2 and 25 times higher over a century [*Stocker*, 2014]. In 2017 human-induced warming reached a benchmark value of 1 °C above pre-industrial time (IPCC special report on Global warming of 1.5 °C). Future climate projections reveal a range of global temperature rise scenarios in response to variable CO_2 release rates (Figure 12). Even the scenario with no human-induced radiative forcing after 2055 is predicting a temperate rise throughout the 21st century.

No reduction of net CO_2 radiative forcing will bring us to 1.5 °C warming above pre-industrial time already by 2040 (IPCC special report on Global warming of 1.5 °C). This may have extensive impacts on the temperature-dependent cryosphere and carbon inventories associated to it. Today's climate already forces ice-sheet retreats [*Hanna et al.*, 2008; *Rignot and Thomas*, 2002], Arctic sea ice decline [*Parkinson and Cavalieri*, 2008; *Sévellec et al.*, 2017] and permafrost thaw [*Sazonova et al.*, 2004].

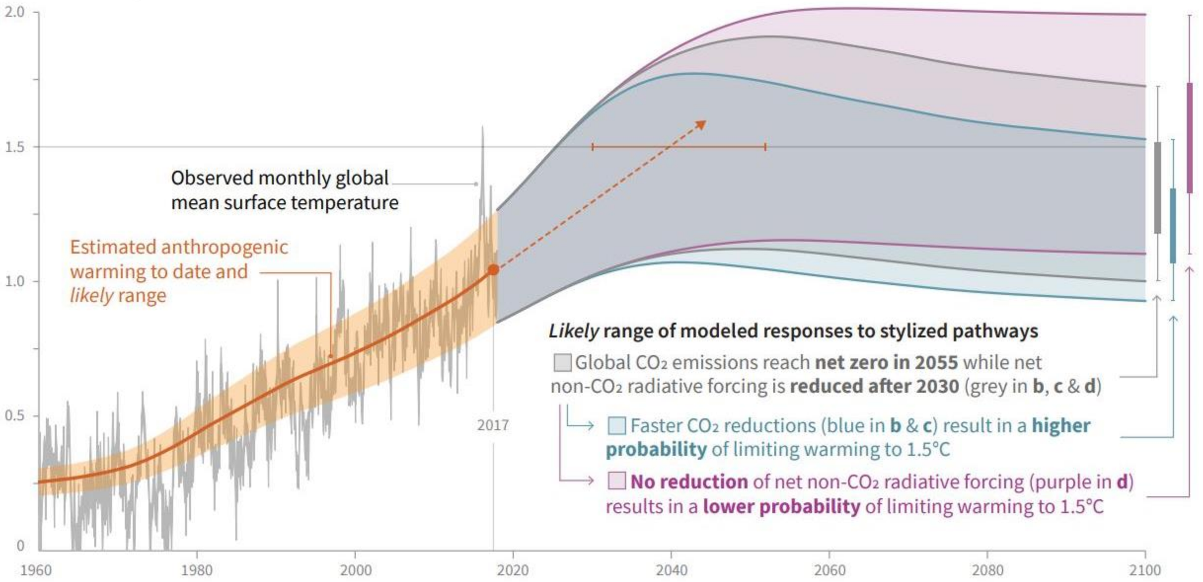

Figure 12 – Observed global temperature changes and modeled future climatic feedback in response to variable anthropogenic CO_2 emission scenarios (IPCC special report on Global warming of 1.5 °C).

Among the subsea CH_4 carbon reservoirs, gas hydrates and permafrost are deemed the most important to the ocean-atmosphere system because of their vast distribution and inconstancy [*Ruppel and Kessler*, 2017]. Permafrost and gas hydrates are major carbon sinks and storage capacitors for carbon, should the environmental conditions support them. Once temperature and/or pressure becomes insufficient, the capacitors turn into strong emitters of CH_4 carbon. The complex nature of subsea permafrost and gas hydrates that are, on one hand are dependent on, but on the other hand, may modulate the global climate through emissions of CH_4 remains a major discussion point today [*James et al.*, 2016; *Ruppel and Kessler*, 2017; *Shakhova et al.*, 2015]. In response to a natural warming climate scenario during interglacials, the cryosphere may have controlled intra-permafrost and subglacial gas hydrate reservoirs collapse [*Portnov et al.*, 2014; *Portnov et al.*, 2016]. Despite the fact that interglacial hydrate destabilization events were indeed deciphered in marine sediments [*Cremiere et al.*, 2016; *Hill et al.*, 2006], the contribution of this extensive submarine gas source to the atmosphere remains controversial.

Comparing present terrestrial permafrost and gas hydrate systems with their marine counterparts, the latter ones appear less efficient contributors to atmospheric methane pool due to microbial filter systems within the bottom sediments [*Boetius et al.*, 2000] and the overlying water column [*Steinle et al.*, 2015]. Recent studies suggest that on the Arctic Shelves (90 – 459 m water depth) only 0.07% of all methane entering the water column reaches the atmosphere [*Graves et al.*, 2015; *Mau et al.*, 2017]. Corresponding to these conservative estimates, measurements of methane concentrations above sea-air interface at western Svalbard margin seepage sites claim absence of ocean-atmosphere methane flux, yet one hotspot is reported just north of Svalbard [*Myhre et al.*, 2016; *Platt et al.*, 2018]. Contemporary total flux of methane across the ocean seafloor is 16 – 3,200 Tg CH_4 y^{-1} [*Ruppel and Kessler*, 2017], while the total emission of methane from ocean surface to atmosphere is ~0.6 to 10 Tg CH_4 y^{-1}. For comparison, total emissions from natural wetlands vary from ~175 to ~217 Tg CH_4 y^{-1} [*Cranston*, 1994; *Rhee et al.*, 2009].

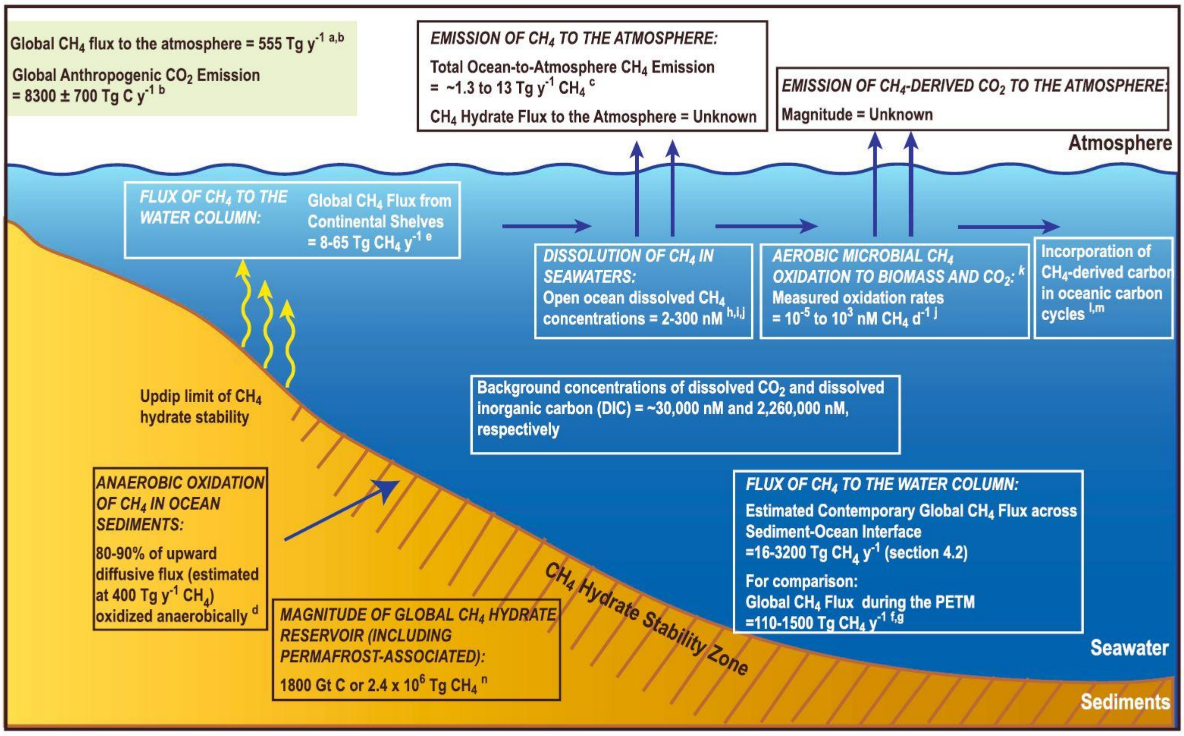

Figure 13 - Sources and sinks of hydrate-bound methane [*Ruppel and Kessler*, 2017]

Today's CH_4 carbon system is largely described by sinks and sources which are only tentatively quantified (Figure 13) [*Ruppel and Kessler*, 2017]. Much less is known about past methane inventories modulated by cold or warm climates. During Late Glacial Maximum, the Barents Sea Ice-sheet covered an enormous area of 2.4 x 10^{6} km^2, including the entire Barents Sea shelf [*Patton et al.*, 2015]. Vast amounts of presently active methane seepage sites were covered by more than 1000 m thick ice-sheet and thus immobilized within the thick subglacial gas hydrate stability zone [*Portnov et al.*, 2016]. A cluster of methane seeps (~500 individual flares within 4 km^2) on the western Svalbard margin shows activity at today's water depth of ~240 m contributing ~438,400,000 g CH_4 y^{-1} [*Sahling et al.*, 2014]. Assuming the grounded ice-sheet covered this area for at least 5,000 years [*Patton et al.*, 2017] and constant methane flux that can be assumed to be equal to today's flux, up to 2.192 Tg CH_4 might have been subglacially isolated within the area. Estimates of subglacial methanogenesis suggest that 22 to 4680 Gt CH_4 carbon were stored in situ under Northern Hemisphere LGM ice-sheets [*Wadham et al.*, 2008]. Proportion of thermogenic methane involved in subglacial methane cycle is yet to be determined.

Upon ice-sheet collapse rapid and extensive seafloor methane discharge may happen. Proportion of dissolved methane increases as the gas bubbles rise through the water column. The water depth has a primary control on the timing of bubble exposure to solvent and, thus, is a first order measure of ocean methane utilization [*Greinert et al.*, 2006]. Dissolved methane is further subjected to aerobic oxidation [*Graves et al.*, 2015]. However, it is unknown how fast the seawater microbial population grows in response to an increase of methane concentrations. Thus, it is not unlikely, that massive seabed methane release at least for a short time period is not balanced with microbial consumption [*Du and Kessler*, 2012; *Mau et al.*, 2013]. Growing methane concentrations in surface waters facilitate sea-atmosphere methane flux. However, they may also increase the biological productivity of the surface water causing withdrawal of CO_2 from atmosphere [*Pohlman et al.*, 2017].

Apart from dissolved gas, releases of large quantities of free gas analogous to offshore drilling blowouts may reach the sea-air interface [*Leifer and Judd*, 2015]. Blowouts are likely to cause upwelling of water with high concentration of dissolved methane that means reduced concentration gradient between the gas bubble and ambient water inhibiting methane dissolution and supporting free gas transport [*Leifer et al.*, 2006]. Blowout events due to abrupt postglacial methane release has been suggested for the Barents Sea shelf [*Long et al.*, 1998] and permafrost bearing regions [*Moskvitch*, 2014]. This gives rise to perceptions that various aspects of methane release, utilization and related atmospheric chemistry changes await more research. For example, the magnitude of methane release from a collapsing cryosphere during the last 2.7 Ma and its climate amplifying potential remain of high interest considering projections for a future climate.

2 Summary of Articles

2.1 Article 1

Pavel Serov, Alexey Portnov, Jürgen Mienert, Petr Semenov, Polina Ilatovskaya (2015). **Methane release from pingo-like features across the South Kara Sea shelf, an area of thawing offshore permafrost**. *Journal of Geophysical Research: Earth Surface*. DOI: 10.1002/2015JF003467

During the last glacial maximum, 120 m sea-level drop emerged vast territories of a non-glaciated South Kara Sea shelf. Exposure to -15 ºC mean annual air temperatures caused the formation of up to ~ 350 m thick permafrost. Subsequent transgression started ~19,000 years ago initiated thawing of the relic permafrost that is still ongoing today. Thawing permafrost may emit methane trapped inside frozen sediments in form of free gas and gas hydrate, as well as organic matter supporting microbial methanogenesis.

In **Article 1** we, for the first time, report and investigate ice-bearing domes (pingo-like features - PLF) on the West Yamal Shelf (40 – 80 m water depth) of the South Kara Sea. PLF 1 does not show any elevated methane concentrations on its surface and frozen sediments outcrop on the seafloor. PLF 2, in contrast, reveals evidence of thawing and elevated methane concentrations. In both locations, our geochemical results demonstrate a biogenic nature of methane gas and no contribution of heavier thermogenic hydrocarbons.

Combining our observations with published results of permafrost modeling we suggest a mechanism of permafrost-bound methane release involving decomposition of intra-permafrost gas hydrates. Further, we propose a range of possible scenarios of PLF formation in areas of subsea permafrost retreat and methane release that is important for many circum-Arctic regions.

Due to geothermal heat fluxes, subsea permafrost thaws from below despite cold (> -1 ºC) bottom water temperatures on its upper boundary. The lower part of subsea permafrost is lying within the pressure / temperature field of methane hydrate phase stability. Retreat of the lower permafrost boundary causes a collapse of the associated GHSZ, hydrate-bound methane release, and pore pressure build up. Methane gas accumulating beneath progressively thinning permafrost may push-up the remaining permafrost cap forming a PLF. Higher methane concentration at PLF 2 may be explained by more pronounced thawing likely reflecting inhomogeneity in geothermal heat flux, initial ice saturation and lithological properties.

State of submarine and onshore permafrost in Yamal peninsula region has become concerning in light of recently occurred blow-out craters and our report of PLFs releasing methane. Yet scarce geophysical and drilling data limit our attempts to estimate current boundaries of permafrost, rate of its retreat and associated regional methane release.

2.2 Article 2

Pavel Serov, Sunil Vadakkepuliyambatta, Jurgen Mienert, Henry Patton, Alexey Portnov, Anna Silyakova, Giuliana Panieri, Michael L. Carroll, JoLynn Carroll, Karin Andreassen, Alun Hubbard (2017). **Postglacial response of Arctic Ocean gas hydrates to climatic amelioration.** *Proceedings of the National Academy of Science of the United States of America (PNAS)*. DOI: 10.1073/pnas.1619288114

In **Article 2** we investigate the effect of environmental changes from the Last Glacial Maximum to the present day on the stability of gas hydrates on an Arctic Ocean continental margin. Our study integrates empirical observations of past and present seabed methane release in the previously glaciated Stofjorden trough in the north-western Barents Sea and a coupled ice-sheet/gas hydrate model to identify phases of subglacial methane sequestration and release.

Geophysical data reveal a group of seabed domes (350-500 m in diameter and 6-10 m high) at 370 – 390 m water depth bearing gas hydrates and releasing thermogenic hydrocarbon gas into the water column. The domes host abundant methane-derived authigenic carbonate formations visible on the seabed and appearing within a sediment section in distinct layers. Due to sufficient fraction of methane-derived carbonate formations and gas hydrates in soft cohesive sediments we refer the structures to gas hydrate pingos (GHPs). Layered appearance of methane-derived carbonate formations points toward variable intensity of seabed methane leakage in the past.

Our gas hydrate stability model is forced with transient subglacial pressure and temperature derived from ice-sheet model. The seafloor pressure and temperature is derived from existing sea-level curves and oxygen isotope records. The coupled model shows the dynamic nature of the GHSZ during the last 37,000 years. The onset of the glaciation provoked the build-up of GHSZ ~35,000 years BP. The 200-220 m thick glacially controlled GHSZ was present in Storfjorden Trough for 13,500 years until the retreat of the ice-sheet. Deglaciation caused depressurization and seabed warming due to removal of ice load and encroach of ocean waters that reduced GHSZ to a c. 40 m thickness. Subsequently, the submarine GHSZ started to collapse due to ocean warming of bottom waters during Heinrich event H1 (15,000 – 13,000 years BP), the Bølling and Allerød interstadials (13,000 – 11,000 years BP) and the Holocene optimum (9,000 – 8,000 years BP). This triggered a release of hydrate-bound methane and migration of gas from deeper sources allowing more thermogenic gas to reach the seabed. The variability of methane efflux is documented in discrete appearances of methane-derived authigenic carbonates in post-glacial sediment sections.

Through synthesis of empirical data and hybrid ice-sheet/GHSZ modeling we show that an extensive gas hydrate system formed in subglacial conditions across Storfjorden Trough during the Last Glacial

Maximum. This system subsequently experienced repeated cycles of collapse and reemergence of gas hydrates due to changes in oceanographic conditions and glacio-isotatic adjustments. Our study shows that abrupt changes in pressure and temperature conditions related to interactions of grounded ice-sheets, postglacial isostatic rebound and influx of variable ocean currents modulate gas storage and release. Such study is deemed particularly important in the light of a potential collapse of the Greenland ice-sheet under future global warming.

2.3 Article 3

Karin Andreassen, Alun Hubbard, Monica Winsborrow, Henry Patton, Sunil Vadakkepuliyambatta, Andreia Plaza-Faverola, Eythor Gudlaugsson, Pavel Serov, Alexey Deryabin, Rune Mattingsdal, Jurgen Mienert, Stefan Bunz (2017). **Massive blow-out crater formed by hydrate-controlled methane expulsion from the Arctic seafloor.** *Science*. DOI: 10.1126/science.aal4500

A grounded ice-sheet controlled the evolution of a gas hydrate stability zone across the Barents Sea shelf. However, the magnitude of methane release due to postglacial gas hydrate decomposition remained elusive. In the **Article 3** we present geophysical data documenting >100 seabed methane-leaking craters up to 1.2 km wide and 35 m deep within 440 km^2 in previously glaciated Bjørnøya Trough. The craters are engraved in Middle-Triassic sedimentary bedrock covered with <2 m thick veneer of glacigenic deposits. 2D seismic data indicate a series of faults connecting Triassic hydrocarbon source and reservoir rocks documented at a strategic petroleum industry borehole to shallow gas accumulations.

Combining our observations of an extensive subsurface fluid flow system with a paired ice-sheet and GHSZ model we propose a conceptual scenario for the formation of craters in the northern Barents Sea. Cyclic episodes of Barents Sea ice-sheet loading and unloading throughout the Pleistocene caused perturbations of a subseabed pressure field in thermogenic gas reservoirs. This enhanced sub-vertical cracking and gas migration along faults into glacially-controlled GHSZ. Rapid retreat of grounded ice-sheet (17,000 – 15,000 years BP) caused a shoaling of lower GHSZ boundary, while a release of hydrate-bound methane contributed to hydrate growth in a still remaining but shallow and thin GHSZ. Volume increase due to hydrate growth and hydrofracturing led to GHP formation. Upon deglaciation, the seafloor overlain with a 320 m thick and warm water column was outside the GHSZ, leading to dissociation of hydrates within GHPs, followed by their collapse, methane expulsion and blow-out crater formation.

Thermogenic gas reservoirs affected by grounded ice-sheets are wide spread. A region of 33 million km^2 with confirmed hydrocarbon reserves offshore northern Europe, Russia, Canada and the United States was directly affected by the last glaciation [*Ehlers and Gibbard*, 2007]. Thus, analogous to our study site, such glacially-controlled gas hydrate reservoirs may be common in many regions of the Arctic.

2.4 Article 4

Wei-Li Hong, Marta E. Torres, JoLynn Carroll, Antoine Cre´mie`re, Giuliana Panieri, Haoyi Yao, Pavel Serov (2017). **Seepage from an arctic shallow marine gas hydrate reservoir is insensitive to momentary ocean warming.** *Nature Communications*. DOI: 10.1038/ncomms15745

Gas hydrate accumulations located close to shallow termination of GHSZ across the Arctic Ocean continental margins are thought to have experienced gas hydrate dissociation induced by warming of ocean bottom water. In the **article 4** we investigate the potential influence of seasonal and decadal water temperature changes on gas hydrate pingos in Storfjorden Trough (380 m water depth).

Our geochemical analyses indicate concaved shapes of downcore profiles of (SO_4^{2-}, ΣHS, TA, Fe^{2+}, Ca^{2+}, Mg^{2+} and NH_4^{+}) in pore water pointing towards non-steady-state behavior of chemical species. Considering 5 potential reasons for such pattern, we model the responses of the pore water profiles to each of them. Our results show that increased methane flux is the most plausible candidate to explain observed non-steady-state geochemical profiles. Pore-water sulfate concentrations are used as proxy for anaerobic methane oxidation (AOM), which is controlled by upward flux of methane. The transport-reaction model of AOM indicates timing of enhanced methane ventilation events over different parts of one gas hydrate bearing mound (pingo). Further, we investigate if seasonal or decadal bottom warming trends may trigger gas hydrate dissociation and methane release. Considering seasonal temperature trends imposed on a longer-term trend of 1 °C warming of bottom water over 30 years we conclude that only 2.3 m of upper sediment section might experience gas hydrate dissociation that cannot explain methane flux matching with observed sulfate profiles.

Pre-anthropogenic age of methane flux events and limited contributions of recent bottom warming suggest that observed geochemical anomalies are not connected to ocean temperature-induced dissociation of gas hydrates. In turn, subseafloor controls of methane venting events such as pressure changes, opening and sealing of fractures are likely to explain increased methane fluxes in the past. These pulsations may be imposed on millennia-scale methane release events inferred from coupled ice-sheet/gas hydrate modeling (**Article 2**).

2.5 Article 5

Pavel Serov, Henry Patton, Malin Waage, Calvin Shackleton, Jürgen Mienert, Karin Andreassen. **Subglacial erosion and transportation of gas hydrate bearing sediments on an Arctic Ocean continental margin.** *Manuscript.*

Pleistocene glaciations of the Barents Sea shelf eroded up to 3 km of sedimentary strata. In areas were methane fluxes are sufficient to support gas hydrate formation, glacial erosion may affect subglacial gas hydrate inventories previously considered undisturbed under the thick ice. In the **Article 5** we investigate the erosion effect of LGM Storfjordrenna Ice Stream on gas hydrate bearing deposits in an area of strong thermogenic gas leakage from a deep source.

Here we use 1 dimensional multiphase fluid flow and gas hydrate model TOUGH+ HYDRATE [*Moridis*, 2014] to simulate evolution of gas hydrate, free and dissolved gas in pore space of deposits underlying the LGM Storfjordrenna ice stream. The model is constrained with empirical data revealing sediment thicknesses, stratigraphy, and active subseabed migration of thermogenic gas. Analogous to **Article 2**, we force our gas hydrate model with ice thickness, bottom temperature and isostatically adjusting topography derived from the UiT ice-sheet model. Moreover, we introduce transient seabed erosion parameter acquired through adjusting previously published average erosion rates with variating basal velocity of the ice stream. We assume that higher velocities of the Storfjordrenna Ice Stream at ice - sediment interface correspond to higher rates of subglacial erosion. In order to show a range of possible scenarios we consider 3 different average erosion rates consistent with literature: 1.0 mm/yr, 1.7 mm/yr – the most likely scenario, and 3.0 mm/yr.

The modeling indicates that, depending on the average erosion rate scenario, 13.4 – 40.2 m of sediments is eroded during ~14,100 years interval of ice-sheet dominating our study area. These sediment erosion values correspond to 0.11 – 0.32 m^3 of methane hydrate eroded from 1 m^2 of seafloor at areas of active methane release during the LGM. These values are comparable to amount of hydrate that are predicted to disappear from 1 m^2 of western Svalbard shelf at 400 m water depth by the end of the 21st Century [*Marín-Moreno et al.*, 2015].

Extrapolating our point estimates, within 5 gas migration conduits (total area 137,500 m^2) mapped at the study area using high-resolution P-cable 3D seismic technology the LGM glacial erosion may remove 15,125 to 44,000 m^3 of methane hydrate. Eroded hydrate-bearing deposits may be frozen into the ice or dissolved in subglacial water and transported to the ice margin. It is very likely that some portions of glacially eroded methane hydrate or dissolved hydrate-bound gas reach the ice margin and discharge into the ocean during glaciations. Taking into account wide availability of methane sources and fluid leakage structures across the Barents Sea shelf experienced > 30 glacial cycles, the implications of subglacial denudation of gas hydrate-bearing sediments for ocean methane uptake may be much broader.

3 Future research

First attempts to investigate the behavior of the cryosphere-dependent methane inventories throughout the last glacial cycle showed a potential significance of expanding similar multidisciplinary studies to earlier glaciations and to the future scenarios of the Greenland ice-sheet dynamics. Since 2.7 ma, the Barents Sea shelf experienced up to 30 cycles of glaciation – deglaciation [*Knies et al.*, 2009], some of which might also have impacted the South Kara Sea shelf. Limited amount of empirical constrains on ice-sheet evolution and paleo fluid flow is a major challenge. However, despite late Weichselian glaciation “reset” seabed imprints and underlying geological features of previous glacial cycles, trough mouth fans and some shelf areas may still preserve valuable stratigraphic records of older glacial cycles. Relying on these empirical constrains, CAGE is developing a model of Pleistocene evolution of the Barents Sea Ice-sheet that would be of great importance for reconstructing gas hydrate dynamics and seabed methane release history. Here, the dynamics of the Greenland ice-sheet and its impacts on gas reservoirs is today’s best analogue in a rapidly changing world during climate change [*Hanna et al.*, 2013; *Robinson et al.*, 2012]. Greenland with the large shelf areas could be one of the key regions for observing environmental changes on the seabed.

Investigating glacial/interglacial deposits of Pleistocene glacial cycles for potential fluid flow features using high-resolution 3D seismic P-Cable surveys may provide new insights into paleo methane release dynamics connecting numerical modeling with actual geological observations. Stratigraphic correlation of glacial units bearing fluid flow features would provide tentative age constrains of fluid migration patterns. Drilling campaigns concentrating on methane-derived authigenic carbonate records may further contribute to verify age of methane release events.

Another direction of potential future research comes with in situ measurements of methane concentrations and studies of methane oxidizing biomass in front of active marine terminating ice streams of Greenland. It may shed more light on similar scenarios of the former environmental conditions along the western Barents Sea ice-sheet. The conceptual scenarios of subglacial methane sequestration and postglacial release that we proposed in Articles 2, 3 and 5 neglect potential bacterial utilization of methane. Very limited amount of literature on subglacial methane microbiology, as well as in situ measurements of methane concentrations in front of marine terminated ice-sheets exists today. Understanding of methane turnover in subglacial environments is important for assessing feedbacks and climate accelerators in a changing Arctic under future warming.

List of figures

Figure 12 – Observed global temperature changes and modeled future climatic feedback in response to variable anthropogenic CO_2 emission scenarios (IPCC special report on Global warming of 1.5 °C)

Figure 13 - Sources and sinks of hydrate-bound methane [*Ruppel and Kessler*, 2017]

Reference

Alley, R. B. (2000), Ice-core evidence of abrupt climate changes, *Proceedings of the National Academy of Sciences*, *97*(4), 1331-1334, doi:10.1073/pnas.97.4.1331.

Alley, R. B., and P. U. Clark (1999), THE DEGLACIATION OF THE NORTHERN HEMISPHERE: A Global Perspective, *Annual Review of Earth and Planetary Sciences*, *27*(1), 149-182, doi:10.1146/annurev.earth.27.1.149.

Andreassen, K., et al. (2017), Massive blow-out craters formed by hydrate-controlled methane expulsion from the Arctic seafloor, *Science*, *356*(6341), 948-953, doi:10.1126/science.aal4500.

Anell, I. M., J. I. Faleide, and A. Braathen (2016), Regional tectono-sedimentary development of the highs and basins of the northwestern Barents Shelf, *Norsk Geologisk Tidsskrift*, *96*(1), 27-41.

Archer, D. (2015), A model of the methane cycle, permafrost, and hydrology of the Siberian continental margin, *Biogeosciences*, *12*(10), 2953-2974.

Auriac, A., P. L. Whitehouse, M. J. Bentley, H. Patton, J. M. Lloyd, and A. Hubbard (2016), Glacial isostatic adjustment associated with the Barents Sea ice-sheet: A modelling inter-comparison, *Quaternary Science Reviews*, *147*, 122-135, doi:http://dx.doi.org/10.1016/j.quascirev.2016.02.011.

Bergh, S. G., and P. Grogan (2003), Tertiary structure of the Sørkapp-Hornsund Region, South Spitsbergen, and implications for the offshore southern extension of the fold-thrust Belt, *Norwegian Journal of Geology*, *83*, 43-60.

Boetius, A., K. Ravenschlag, C. J. Schubert, D. Rickert, F. Widdel, A. Gieseke, R. Amann, B. B. Jorgensen, U. Witte, and O. Pfannkuche (2000), A marine microbial consortium apparently mediating anaerobic oxidation of methane, *Nature*, *407*(6804), 623-626, doi:http://www.nature.com/nature/journal/v407/n6804/suppinfo/407623a0_S1.html.

Brook, E. J. (2005), Tiny Bubbles Tell All, *Science*, *310*(5752), 1285-1287, doi:10.1126/science.1121535.

Bröder, L., T. Tesi, A. Andersson, I. Semiletov, and Ö. Gustafsson (2018), Bounding cross-shelf transport time and degradation in Siberian-Arctic land-ocean carbon transfer, *Nature Communications*, *9*(1), 806, doi:10.1038/s41467-018-03192-1.

Callaghan, T. V., M. Johansson, J. Key, T. Prowse, M. Ananicheva, and A. Klepikov (2011), Feedbacks and Interactions: From the Arctic Cryosphere to the Climate System, *Ambio*, *40*(Suppl 1), 75-86, doi:10.1007/s13280-011-0215-8.

Chappellaz, J., et al. (2013), High-resolution glacial and deglacial record of atmospheric methane by continuous-flow and laser spectrometer analysis along the NEEM ice core, *Climate of the Past*, *9*, 2579-2593, doi:10.5194/cp-9-2579-2013.

Clark, P. U., A. S. Dyke, J. D. Shakun, A. E. Carlson, J. Clark, B. Wohlfarth, J. X. Mitrovica, S. W. Hostetler, and A. M. McCabe (2009), The Last Glacial Maximum, *Science*, *325*(5941), 710-714, doi:10.1126/science.1172873.

Cranston, R. (1994), Marine sediments as a source of atmospheric methane, *Bulletin of the Geological Society of Denmark*, *41*, 101-109.

Cremiere, A., A. Lepland, S. Chand, D. Sahy, D. J. Condon, S. R. Noble, T. Martma, T. Thorsnes, S. Sauer, and H. Brunstad (2016), Timescales of methane seepage on the Norwegian margin following collapse of the Scandinavian Ice-sheet, *Nat Commun*, *7*, doi:10.1038/ncomms11509.

Dickens, G. R., C. K. Paull, and P. Wallace (1997), Direct measurement of in situ methane quantities in a large gas-hydrate reservoir, *Nature*, *385*, 426, doi:10.1038/385426a0.

Du, M., and J. D. Kessler (2012), Assessment of the Spatial and Temporal Variability of Bulk Hydrocarbon Respiration Following the Deepwater Horizon Oil Spill, *Environmental Science & Technology*, *46*(19), 10499-10507, doi:10.1021/es301363k.

Ehlers, J., and P. L. Gibbard (2007), The extent and chronology of Cenozoic global glaciation, *Quaternary International*, *164*, 6-20.

Fleming, K., P. Johnston, D. Zwartz, Y. Yokoyama, K. Lambeck, and J. Chappell (1998), Refining the eustatic sea-level curve since the Last Glacial Maximum using far- and intermediate-field sites, *Earth and Planetary Science Letters*, *163*(1), 327-342, doi:https://doi.org/10.1016/S0012-821X(98)00198-8.

Gautier, D. L., et al. (2009), Assessment of Undiscovered Oil and Gas in the Arctic, *Science*, *324*(5931), 1175-1179, doi:10.1126/science.1169467.

Ginsburg, G. (1998), Gas hydrate accumulation in deep-water marine sediments, *Geological Society, London, Special Publications*, *137*(1), 51-62.

Grama, Y. (2012), The analysis of Russian oil and gas reserves, *International Journal of Energy Economics and Policy*, *2*(2), 82-91.

Graves, C. A., L. Steinle, G. Rehder, H. Niemann, D. P. Connelly, D. Lowry, R. E. Fisher, A. W. Stott, H. Sahling, and R. H. James (2015), Fluxes and fate of dissolved methane released at the seafloor at the landward limit of the gas hydrate stability zone offshore western Svalbard, *Journal of Geophysical Research: Oceans*, *120*(9), 6185-6201, doi:10.1002/2015JC011084.

Greinert, J., Y. Artemov, V. Egorov, M. De Batist, and D. McGinnis (2006), 1300-m-high rising bubbles from mud volcanoes at 2080 m in the Black Sea: Hydroacoustic characteristics and temporal variability, *Earth and Planetary Science Letters*, *244*(1–2), 1-15, doi:http://dx.doi.org/10.1016/j.epsl.2006.02.011.

Hanna, E., P. Huybrechts, K. Steffen, J. Cappelen, R. Huff, C. Shuman, T. Irvine-Fynn, S. Wise, and M. Griffiths (2008), Increased runoff from melt from the Greenland Ice-sheet: a response to global warming, *Journal of Climate*, *21*(2), 331-341.

Hanna, E., et al. (2013), Ice-sheet mass balance and climate change, *Nature*, *498*, 51, doi:10.1038/nature12238.

Harris, C., and J. B. Murton (2005), Cryospheric systems: glaciers and permafrost, Geological Society of London.

Hill, T. M., J. P. Kennett, D. L. Valentine, Z. Yang, C. M. Reddy, R. K. Nelson, R. J. Behl, C. Robert, and L. Beaufort (2006), Climatically driven emissions of hydrocarbons from marine sediments during deglaciation, *Proceedings of the National Academy of Sciences*, *103*(37), 13570-13574, doi:10.1073/pnas.0601304103.

Høy, T., and B. Lundschien (2011), Triassic deltaic sequences in the northern Barents Sea, *Geological Society, London, Memoirs*, *35*(1), 249-260.

Inagaki, F., et al. (2006), Biogeographical distribution and diversity of microbes in methane hydrate-bearing deep marine sediments on the Pacific Ocean Margin, *Proceedings of the National Academy of Sciences of the United States of America*, *103*(8), 2815-2820, doi:10.1073/pnas.0511033103.

Jakobsson, M., et al. (2014), Arctic Ocean glacial history, *Quaternary Science Reviews*, *92*, 40-67, doi:http://dx.doi.org/10.1016/j.quascirev.2013.07.033.

Jakobsson, M., et al. (2012), The International Bathymetric Chart of the Arctic Ocean (IBCAO) Version 3.0, *Geophysical Research Letters*, *39*(12), n/a-n/a, doi:10.1029/2012GL052219.

James, R. H., et al. (2016), Effects of climate change on methane emissions from seafloor sediments in the Arctic Ocean: A review, *Limnology and Oceanography*, n/a-n/a, doi:10.1002/lno.10307.

Judd, A., and M. Hovland (2009), Seabed fluid flow: the impact on geology, biology and the marine environment, edited, Cambridge University Press.

Kizyakov, A., M. Zimin, A. Sonyushkin, Y. Dvornikov, A. Khomutov, and M. Leibman (2017), Comparison of Gas Emission Crater Geomorphodynamics on Yamal and Gydan Peninsulas (Russia), Based on Repeat Very-High-Resolution Stereopairs, *Remote Sensing*, *9*(10), 1023.

Knies, J., J. Matthiessen, C. Vogt, J. S. Laberg, B. O. Hjelstuen, M. Smelror, E. Larsen, K. Andreassen, T. Eidvin, and T. O. Vorren (2009), The Plio-Pleistocene glaciation of the Barents Sea–Svalbard region: a new model based on revised chronostratigraphy, *Quaternary Science Reviews*, *28*(9–10), 812-829, doi:http://dx.doi.org/10.1016/j.quascirev.2008.12.002.

Koch, S., C. Berndt, J. Bialas, M. Haeckel, G. Crutchley, C. Papenberg, D. Klaeschen, and J. Greinert (2015), Gas-controlled seafloor doming, *Geology*, doi:10.1130/g36596.1.

Laberg, Andreassen, and Vorren (2012), Late Cenozoic erosion of the high-latitude southwestern Barents Sea shelf revisited, *Geological Society of America Bulletin*, *124*(1-2), 77-88.

Lasabuda, A., J. S. Laberg, S.-M. Knutsen, and P. Safronova (2018), Cenozoic tectonostratigraphy and pre-glacial erosion: A mass-balance study of the northwestern Barents Sea margin, Norwegian Arctic, *Journal of Geodynamics*, doi:https://doi.org/10.1016/j.jog.2018.03.004.

Lea, D., P. Martin, D. Pak, and H. Spero (2003), 350 kyr sea level reconstruction and foraminifer isotope data, IGBP PAGES/World Data Center A for Paleoclimatology Data Contribution Series# 2003-010, *NOAA/NGDC.(Paleoclimatology Program, Boulder*.

Leifer, I., and A. Judd (2015), The UK22/4b blowout 20 years on: Investigations of continuing methane emissions from subseabed to the atmosphere in a North Sea context, *Marine and Petroleum Geology*, *68*, 706-717, doi:http://dx.doi.org/10.1016/j.marpetgeo.2015.11.012.

Leifer, I., B. P. Luyendyk, J. Boles, and J. F. Clark (2006), Natural marine seepage blowout: Contribution to atmospheric methane, *Global Biogeochemical Cycles*, *20*(3), n/a-n/a, doi:10.1029/2005GB002668.

Levin, L. A., et al. (2016), Hydrothermal Vents and Methane Seeps: Rethinking the Sphere of Influence, *Frontiers in Marine Science*, *3*(72), doi:10.3389/fmars.2016.00072.

Long, D., S. Lammers, and P. Linke (1998), Possible hydrate mounds within large sea-floor craters in the Barents Sea, *Geological Society, London, Special Publications*, *137*(1), 223-237, doi:10.1144/gsl.sp.1998.137.01.18.

Lundschien, B. A., T. Høy, and A. Mørk (2014), Triassic hydrocarbon potential in the Northern Barents Sea; integrating Svalbard and stratigraphic core data, *Norwegian Petroleum Directorate Bulletin*, *11*, 3-20.

Marín-Moreno, H., T. A. Minshull, G. K. Westbrook, and B. Sinha (2015), Estimates of future warming-induced methane emissions from hydrate offshore west Svalbard for a range of climate models, *Geochemistry, Geophysics, Geosystems*, *16*(5), 1307-1323, doi:10.1002/2015GC005737.

Mau, S., J. Blees, E. Helmke, H. Niemann, and E. Damm (2013), Vertical distribution of methane oxidation and methanotrophic response to elevated methane concentrations in stratified waters of the Arctic fjord Storfjorden (Svalbard, Norway), *Biogeosciences*, *10*(10), 6267-6278, doi:10.5194/bg-10-6267-2013.

Mau, S., et al. (2017), Widespread methane seepage along the continental margin off Svalbard - from Bjørnøya to Kongsfjorden, *Scientific Reports*, *7*, 42997, doi:10.1038/srep42997

Mix, A. C., E. Bard, and R. Schneider (2001), Environmental processes of the ice age: land, oceans, glaciers (EPILOG), *Quaternary Science Reviews*, *20*(4), 627-657, doi:https://doi.org/10.1016/S0277-3791(00)00145-1.

Moller, L., T. Sowers, M. Bock, R. Spahni, M. Behrens, J. Schmitt, H. Miller, and H. Fischer (2013), Independent variations of CH4 emissions and isotopic composition over the past 160,000 years, *Nature Geosci*, *6*(10), 885-890, doi:10.1038/ngeo1922

Moridis, G. J. (2014), TOUGH+ HYDRATE v1. 2 User's Manual: A Code for the Simulation of System Behavior in Hydrate-Bearing Geologic Media.

Moskvitch, K. (2014), Mysterious Siberian crater attributed to methane, in *nature news*, edited, nature publishing group, doi:doi:10.1038/nature.2014.15649.

Myhre, C. L., et al. (2016), Extensive release of methane from Arctic seabed west of Svalbard during summer 2014 does not influence the atmosphere, *Geophysical Research Letters*, *43*(9), 4624-4631, doi:10.1002/2016GL068999.

Nelson, F. E., O. A. Anisimov, and N. I. Shiklomanov (2001), Subsidence risk from thawing permafrost, *Nature*, *410*, 889, doi:10.1038/35073746.

Pachauri, R. K., M. R. Allen, V. R. Barros, J. Broome, W. Cramer, R. Christ, J. A. Church, L. Clarke, Q. Dahe, and P. Dasgupta (2014), *Climate change 2014: synthesis report. Contribution of Working Groups I, II and III to the fifth assessment report of the Intergovernmental Panel on Climate Change*, IPCC.

Parkinson, C. L., and D. J. Cavalieri (2008), Arctic sea ice variability and trends, 1979–2006, *Journal of Geophysical Research: Oceans*, *113*(C7).

Patton, K. Andreassen, L. R. Bjarnadóttir, J. A. Dowdeswell, M. C. M. Winsborrow, R. Noormets, L. Polyak, A. Auriac, and A. Hubbard (2015), Geophysical constraints on the dynamics and retreat of the Barents Sea ice-sheet as a paleobenchmark for models of marine ice-sheet deglaciation, *Reviews of Geophysics*, *53*(4), 1051-1098, doi:10.1002/2015RG000495.

Patton, Hubbard, Andreassen, Auriac, P. L. Whitehouse, A. P. Stroeven, C. Shackleton, M. Winsborrow, J. Heyman, and A. M. Hall (2017), Deglaciation of the Eurasian ice-sheet complex, *Quaternary Science Reviews*, *169*, 148-172, doi:http://dx.doi.org/10.1016/j.quascirev.2017.05.019.

Patton, Hubbard, Andreassen, Winsborrow, and A. P. Stroeven (2016), The build-up, configuration, and dynamical sensitivity of the Eurasian ice-sheet complex to Late Weichselian climatic and oceanic forcing, *Quaternary Science Reviews*, *153*, 97-121, doi:http://dx.doi.org/10.1016/j.quascirev.2016.10.009.

Paull, C. K., W. Ussler, S. R. Dallimore, S. M. Blasco, T. D. Lorenson, H. Melling, B. E. Medioli, F. M. Nixon, and F. A. McLaughlin (2007), Origin of pingo-like features on the Beaufort Sea shelf and their possible relationship to decomposing methane gas hydrates, *Geophysical Research Letters*, *34*(1), n/a-n/a, doi:10.1029/2006GL027977.

Platt, S. M., S. Eckhardt, B. Ferré, R. E. Fisher, O. Hermansen, P. Jansson, D. Lowry, E. G. Nisbet, I. Pisso, and N. Schmidbauer (2018), Methane at Svalbard and over the European Arctic Ocean.

Pohlman, J. W., J. Greinert, C. Ruppel, A. Silyakova, L. Vielstädte, M. Casso, J. Mienert, and S. Bünz (2017), Enhanced CO₂ uptake at a shallow Arctic Ocean seep field overwhelms the positive warming potential of emitted methane, *Proceedings of the National Academy of Sciences*, doi:10.1073/pnas.1618926114.

Portnov, A., J. Mienert, and P. Serov (2014), Modeling the evolution of climate-sensitive Arctic subsea permafrost in regions of extensive gas expulsion at the West Yamal shelf, *Journal of Geophysical Research: Biogeosciences*, *119*(11), 2082-2094, doi:10.1002/2014JG002685.

Portnov, A., J. Mienert, M. Winsborrow, K. Andreassen, S. Vadakkepuliyambatta, P. Semenov, and V. Gataullin (2018), Shallow carbon storage in ancient buried thermokarst in the South Kara Sea, *Scientific Reports*, *8*(1), 14342, doi:10.1038/s41598-018-32826-z.

Portnov, A., A. J. Smith, J. Mienert, G. Cherkashov, P. Rekant, P. Semenov, P. Serov, and B. Vanshtein (2013), Offshore permafrost decay and massive seabed methane escape in water depths >20 m at the South Kara Sea shelf, *Geophysical Research Letters*, *40*(15), 3962-3967, doi:doi:10.1002/grl.50735.

Portnov, A., S. Vadakkepuliyambatta, J. Mienert, and A. Hubbard (2016), Ice-sheet-driven methane storage and release in the Arctic, *Nat Commun*, *7*, doi:10.1038/ncomms10314.

Rasmussen, T. L., E. Thomsen, M. A. Ślubowska, S. Jessen, A. Solheim, and N. Koç (2007), Paleoceanographic evolution of the SW Svalbard margin (76°N) since 20,000 14C yr BP, *Quaternary Research*, *67*(1), 100-114, doi:http://dx.doi.org/10.1016/j.yqres.2006.07.002.

Reeburgh, W. S. (2007), Oceanic Methane Biogeochemistry, *Chemical Reviews*, *107*(2), 486-513, doi:10.1021/cr050362v.

Rekant, P., and A. Vasiliev (2011), Distribution of subsea permafrost at the Kara Sea shelf, *Cryosphere of the Earth*, *XV*, *4*, 69-72.

Rhee, T. S., A. J. Kettle, and M. O. Andreae (2009), Methane and nitrous oxide emissions from the ocean: A reassessment using basin-wide observations in the Atlantic, *Journal of Geophysical Research: Atmospheres*, *114*(D12), n/a-n/a, doi:10.1029/2008JD011662.

Rignot, E., and R. H. Thomas (2002), Mass Balance of Polar Ice-sheets, *Science*, *297*(5586), 1502-1506, doi:10.1126/science.1073888.

Robinson, A., R. Calov, and A. Ganopolski (2012), Multistability and critical thresholds of the Greenland ice-sheet, *Nature Climate Change*, *2*, 429, doi:10.1038/nclimate1449

Ruff, S. E., J. F. Biddle, A. P. Teske, K. Knittel, A. Boetius, and A. Ramette (2015), Global dispersion and local diversification of the methane seep microbiome, *Proceedings of the National Academy of Sciences*, *112*(13), 4015-4020, doi:10.1073/pnas.1421865112.

Ruppel, C. D., and J. D. Kessler (2017), The interaction of climate change and methane hydrates, *Reviews of Geophysics*, n/a-n/a, doi:10.1002/2016RG000534.

Sahling, H., et al. (2014), Gas emissions at the continental margin west of Svalbard: mapping, sampling, and quantification, *Biogeosciences*, *11*(21), 6029-6046, doi:10.5194/bg-11-6029-2014.

Sazonova, T. S., V. E. Romanovsky, J. E. Walsh, and D. O. Sergueev (2004), Permafrost dynamics in the 20th and 21st centuries along the East Siberian transect, *Journal of Geophysical Research: Atmospheres*, *109*(D1), doi:doi:10.1029/2003JD003680.

Schneider von Deimling, J., P. Linke, M. Schmidt, and G. Rehder (2015), Ongoing methane discharge at well site 22/4b (North Sea) and discovery of a spiral vortex bubble plume motion, *Marine and Petroleum Geology*, *68, Part B*, 718-730, doi:https://doi.org/10.1016/j.marpetgeo.2015.07.026.

Serié, C., M. Huuse, and N. H. Schødt (2012), Gas hydrate pingoes: Deep seafloor evidence of focused fluid flow on continental margins, *Geology*, *40*(3), 207-210, doi:10.1130/G32690.1.

Sévellec, F., A. V. Fedorov, and W. Liu (2017), Arctic sea-ice decline weakens the Atlantic Meridional Overturning Circulation, *Nature Climate Change*, *7*, 604, doi:10.1038/nclimate3353

Shakhova, N., I. Semiletov, I. Leifer, A. Salyuk, P. Rekant, and D. Kosmach (2010), Geochemical and geophysical evidence of methane release over the East Siberian Arctic Shelf, *Journal of Geophysical Research: Oceans*, *115*(C8), n/a-n/a, doi:10.1029/2009JC005602.

Shakhova, N., et al. (2015), The East Siberian Arctic Shelf: towards further assessment of permafrost-related methane fluxes and role of sea ice, *Philosophical Transactions of the Royal Society of London A: Mathematical, Physical and Engineering Sciences*, *373*(2052), doi:10.1098/rsta.2014.0451.

Siegert, M. J., J. A. Dowdeswell, M. Hald, and J.-I. Svendsen (2001), Modelling the Eurasian Ice-sheet through a full (Weichselian) glacial cycle, *Global and Planetary Change*, *31*(1), 367-385, doi:http://dx.doi.org/10.1016/S0921-8181(01)00130-8

Slaymaker, O., and R. Kelly (2009), *The cryosphere and global environmental change*, John Wiley & Sons.

Sloan, E. D., C. Koh (2008), *Clathrate Hydrates of Natural*

Gases, 3rd ed., CRC Press, Boca Raton, Fla.

Sowers, T. (2006), Late Quaternary Atmospheric CH4 Isotope Record Suggests Marine Clathrates Are Stable, *Science*, *311*(5762), 838-840, doi:10.1126/science.1121235.

Steinle, L., et al. (2015), Water column methanotrophy controlled by a rapid oceanographic switch, *Nature Geosci*, *8*(5), 378-382, doi:10.1038/ngeo2420

Stocker, T. (2014), *Climate change 2013: the physical science basis: Working Group I contribution to the Fifth assessment report of the Intergovernmental Panel on Climate Change*, Cambridge University Press.

Stupakova, A. (2011), Structure and petroleum potential of the Barents-Kara Shelf and adjacent territories, *Oil and gas geology*, *6*(6), 99-115.

Sultan, N., et al. (2004), Triggering mechanisms of slope instability processes and sediment failures on continental margins: a geotechnical approach, *Marine Geology*, *213*(1), 291-321, doi:https://doi.org/10.1016/j.margeo.2004.10.011.

Vadakkepuliyambatta, S., S. Chand, and S. Bünz (2017), The history and future trends of ocean warming-induced gas hydrate dissociation in the SW Barents Sea, *Geophysical Research Letters*, *44*(2), 835-844, doi:doi:10.1002/2016GL071841.

Wadham, J. L., et al. (2012), Potential methane reservoirs beneath Antarctica, *Nature*, *488*(7413), 633-637, doi:http://www.nature.com/nature/journal/v488/n7413/abs/nature11374.html#supplementary-information.

Wadham, J. L., M. Tranter, S. Tulaczyk, and M. Sharp (2008), Subglacial methanogenesis: A potential climatic amplifier?, *Global Biogeochemical Cycles*, *22*(2), n/a-n/a, doi:10.1029/2007GB002951.

Wallmann, K., et al. (2018), Gas hydrate dissociation off Svalbard induced by isostatic rebound rather than global warming, *Nature Communications*, *9*(1), 83, doi:10.1038/s41467-017-02550-9.

Winsborrow, M. C. M., K. Andreassen, G. D. Corner, and J. S. Laberg (2010), Deglaciation of a marine-based ice-sheet: Late Weichselian palaeo-ice dynamics and retreat in the southern Barents Sea reconstructed from onshore and offshore glacial geomorphology, *Quaternary Science Reviews*, *29*(3), 424-442, doi:https://doi.org/10.1016/j.quascirev.2009.10.001.

Yakushev, V. S., and E. M. Chuvilin (2000), Natural gas and gas hydrate accumulations within permafrost in Russia, *Cold Regions Science and Technology*, *31*(3), 189-197, doi:https://doi.org/10.1016/S0165-232X(00)00012-4.

Åström, E. K. L., M. L. Carroll, W. G. Ambrose, A. Sen, A. Silyakova, and J. Carroll (2018), Methane cold seeps as biological oases in the high-Arctic deep sea, *Limnology and Oceanography*, *63*(S1), S209-S231, doi:doi:10.1002/lno.10732.

Article 1

Pavel Serov, Alexey Portnov, Jürgen Mienert, Petr Semenov, Polina Ilatovskaya (2015).

Methane release from pingo-like features across the South Kara Sea shelf, an area of thawing offshore permafrost. *Journal of Geophysical Research: Earth Surface*. DOI: 10.1002/2015JF003467

AGU PUBLICATIONS

JGR

Journal of Geophysical Research: Earth Surface

RESEARCH ARTICLE
10.1002/2015JF003467

Key Points:
- PLFs of uncertain origin were discovered on the South Kara Sea shelf
- Anomalous concentrations of biogenic methane correspond to one of the PLFs
- Subpermafrost methane accumulations can lead to the formation of PLFs

Correspondence to:
P. Serov,
pavel.russerov@uit.no

Citation:
Serov, P., A. Portnov, J. Mienert, P. Semenov, and P. Ilatovskaya (2015), Methane release from pingo-like features across the South Kara Sea shelf, an area of thawing offshore permafrost, *J. Geophys. Res. Earth Surf.*, *120*, doi:10.1002/2015JF003467.

Received 30 JAN 2015
Accepted 11 JUL 2015
Accepted article online 16 JUL 2015

Methane release from pingo-like features across the South Kara Sea shelf, an area of thawing offshore permafrost

Pavel Serov[1,2], Alexey Portnov[1,2], Jurgen Mienert[1], Peter Semenov[2], and Polina Ilatovskaya[2]

[1]Centre for Arctic Gas Hydrate, Environment and Climate, Department of Geology, UiT The Arctic University of Norway, Tromsø, Norway, [2]I.S. Gramberg VNIIOkeangeologia, Saint Petersburg, Russia

Abstract The Holocene marine transgression starting at ~19 ka flooded the Arctic shelves driving extensive thawing of terrestrial permafrost. It thereby promoted methanogenesis within sediments, the dissociation of gas hydrates, and the release of formerly trapped gas, with the accumulation in pressure of released methane eventually triggering blowouts through weakened zones in the overlying and thinned permafrost. Here we present a range of geophysical and chemical scenarios for the formation of pingo-like formations (PLFs) leading to potential blowouts. Specifically, we report on methane anomalies from the South Kara Sea shelf focusing on two PLFs imaged from high-resolution seismic records. A variety of geochemical methods are applied to study concentrations and types of gas, its character, and genesis. PLF 1 demonstrates ubiquitously low-methane concentrations (14.2–55.3 ppm) that are likely due to partly unfrozen sediments with an ice-saturated internal core reaching close to the seafloor. In contrast, PLF 2 reveals anomalously high-methane concentrations of >120,000 ppm where frozen sediments are completely absent. The methane in all recovered samples is of microbial and not of thermogenic origin from deep hydrocarbon sources. However, the relatively low organic matter content (0.52–1.69%) of seafloor sediments restricts extensive in situ methane production. As a consequence, we hypothesize that the high-methane concentrations at PLF 2 are due to microbial methane production and migration from a deeper source.

1. Introduction

During the ice ages of late Pleistocene [*Jakobsson et al.*, 2014] a thick layer of permafrost and gas hydrate deposits formed in subaerial conditions on the Arctic shelves [*Khimenkov and Brushkov*, 2003]. Following the Last Glacial Maximum (LGM) (~19 ka) [*Aubry et al.*, 2009] Arctic shelves were flooded during an extensive ocean transgression reaching ~120 m [*Bauch et al.*, 2001]. Relatively warm ocean waters encroached on areas which had formerly been coastal planes [*Fairbanks*, 1989; *Fleming et al.*, 1998], thereby initiating thermal inundation of permafrost from the top [*Osterkamp et al.*, 1989; *Paull et al.*, 2007]. Simultaneously, permafrost thawed from the bottom due to the influence of geothermal heat flux coupled with warmer upper boundary conditions [*Nicolsky et al.*, 2012; *Rokos et al.*, 2009].

Permafrost can be considered an impermeable seal for gas [e.g., *Shakhova et al.*, 2010] or at least a layer substantially reducing gas migration from the subsurface [*Yakushev*, 2009]. Thus, the distribution and decay of Arctic permafrost over both long- and short-time periods provides an important control on natural emissions of gas, including the potent greenhouse gas—methane—to the atmosphere [*Shakhova et al.*, 2010]. Thawing subsea permafrost also triggers a significant release of methane of various origins that migrates through open taliks into the shallow seas and atmosphere, thereby affecting the global climate [*Delisle*, 2000; *Frederick and Buffett*, 2014; *Majorowicz et al.*, 2011; *Nicolsky et al.*, 2012; *Romanovskii et al.*, 2005].

The extent of relict subsea permafrost along with an inventory of the associated gas hydrates stored within and below the permafrost on the Arctic shelves is still controversial [*Collett et al.*, 2011; *Rachold et al.*, 2007; *Yakushev*, 2009]. Numerous studies have improved our knowledge base and extended the subsea permafrost mapping on the Beaufort Sea shelf [*Brothers et al.*, 2012; *Hu et al.*, 2013; *Taylor et al.*, 2013], the Laptev and East Siberian Sea shelves [*Nicolsky et al.*, 2012; *Romanovskii et al.*, 1998, 2004], and the Kara Sea shelf [*Portnov et al.*, 2013; *Rekant et al.*, 2005; *Rekant and Vasiliev*, 2011]. Modeling performed by *Romanovskii et al.* [2004] suggests that a continuous permafrost layer extended to the 60 m isobaths in the

Laptev and East Siberian Seas. However, continuous subsea permafrost appears to be less abundant on the other Arctic coastal shelf areas. *Brothers et al.* [2012] concluded that minimal extent of ice-bearing permafrost on the U.S. Beaufort continental shelf is limited to the 20 m isobaths.

Portnov et al. [2013] mapped a region of extensive gas release over an area of at least 7500 km^2 located in the South Kara Sea in water depths $>$20 m. The presence of individual gas flares and gas fronts within the water column is closely related to thawed permafrost boundaries. Permafrost was present in only 15% of boreholes drilled offshore Yamal Peninsula in water depths $>$20 m [*GEOS*, 1997]. These drilling results and observations of gas expulsion within the water column imply that the South Kara Sea is a key area of ongoing and extensive permafrost decay.

There are two competing hypotheses for the conditions under which pingo-like formations (PLFs) form: (1) an early study suggests that they formed under terrestrial conditions in low relative sea level stands during glacial episodes throughout the late Pleistocene and were subsequently submerged in interglacials [*Shearer et al.*, 1971] or, alternatively, (2) that they developed in marine environments after the shelf flooding in Holocene times [*Bondarev et al.*, 2002; *Paull et al.*, 2007]. Earlier models of marine PLF formation speculated that gas, emitted during dissociation of gas hydrates within and below thawing permafrost, built up at high pressures driving seafloor doming [*Paull et al.*, 2007]. However, the debate is still ongoing as to whether PLFs are related to gas release since many of the documented PLFs do not reveal any measurable gas discharge [*Bondarev et al.*, 2002; *Paull et al.*, 2007].

Steady state gas leakage and even blowout events have been documented from some of the PLFs at the Beaufort Sea and Russian Arctic shelves [*Hovland et al.*, 1993; *Judd and Hovland*, 2007]. Noteworthy, a drilling vessel (operated by “AMIGE” company) experienced an emergency situation due to sudden and extensive gas release from a well after the drill bit penetrated a gas pocket inside a large PLF in the Pechora Sea [*Bondarev et al.*, 2002; *Rokos*, 2008]. Hence, it follows that some PLFs act as major gas storage and seepage hot spots. The recently described Siberian craters found onshore in permafrost regions of the Yamal Peninsula have also been speculated to be the result of accumulation of high gas pressure and abrupt methane release [*Bogoyavlenskiy*, 2014a, 2014b; *Moskvitch*, 2014].

This study concentrates on offshore PLFs in the shallow waters of the South Kara Sea. Here we report on the acoustic, geological, and geochemical evidence revealing the genesis and evolution of the observed PLFs. We apply a number of geochemical methods, including gas chromatography of gaseous and high molecular weight (HMW) hydrocarbons as well as methane isotope measurements of carbon and hydrogen for deciphering the origin of gas in bottom sediments above two characteristic PLFs in the South Kara Sea shelf. We also integrate our results of both geochemical and high-resolution seismic (HRS) studies with a modeled evolution of permafrost [*Rokos et al.*, 2009] allowing us to suggest possible scenarios for the formation of PLFs on the South Kara Sea shelf.

2. Geological Setting

2.1. Tectonic Framework, Seafloor Morphology, and Lithology of Bottom Sediments

The South Kara Sea lies in a large tectonic depression, the South Kara Syncline, located to the west of the Yamal Peninsula. The syncline developed at a continuation of the East Siberian Plate neighboring the North Kara Plate located to the north of the Novaya Zemlya Archipelago [*Stupakova*, 2011]. The South Kara Syncline has a Paleozoic basement and an up to 14 km thick Permian-Cenozoic sedimentary cover composed of terrigenous deposits. Pliocene-Quaternary strata unconformably overlay older deposits reaching maximal thickness of 300 m on the Yamal Peninsula and ~125 m on the West Yamal shelf [*Sherbakov et al.*, 2010].

The Novozemelsky trough and coastal shelf offshore Yamal Peninsula are the two major physiographic elements that define the morphology of the South Kara Sea (Figure 1a). Shelf depths of less than 120 m extend up to 200 km offshore in the central part and up to 105 km and 170 km in the southern and northern parts of the Kara Sea, respectively. The coastal shelf of the South Kara Sea is glacially eroded [*Melnikov and Spesivtsev*, 1995; *Pavlidis et al.*, 1998] with overdeepened troughs and incised river valleys partly filled with marine terrigenous deposits [*Sherbakov et al.*, 2010].

The upper sedimentary units across the shelf are dominated by Pleistocene and Holocene marine and alluvial-marine deposits. Pre-Weichselian deposits consist mostly of clays overlain by interbeds of sands,

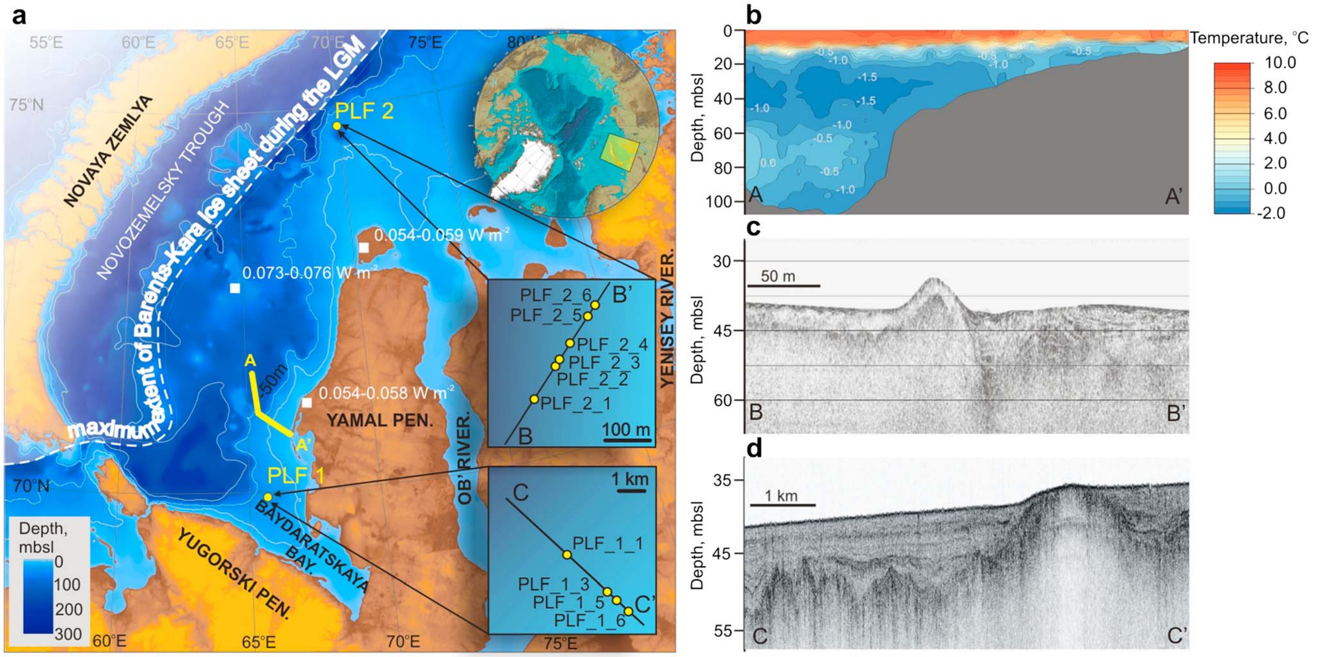

Figure 1. (a) Location of sampling sites on the South Kara Sea shelf. The dashed white line shows the maximum extent of Barents-Kara ice sheet coming from the west during the Late Glacial Maximum (modified from *Polyak et al.* [2002]). The solid yellow line shows the location of water temperature profile obtained by I.S. Gramberg VNIIOkeangeologia in summer 2013. The white squares show the locations of boreholes, where the heat flux values were obtained. The insets in Figure 1a show the location of high-resolution seismic lines crossing the PLFs and sampling stations (yellow dots). (b) Water temperature profile. (c) High-resolution seismic line across the PLF 2. (d) High-resolution seismic line across the PLF 1.

silts, and clays of Middle Weichselian to Holocene age (marine oxygen isotope stage (MIS)4-MIS1) [*Melnikov and Spesivtsev*, 1995]. The uppermost Holocene sediments consist of mud with low sand content and scarce ice-rafted debris [*Levitan et al*., 2004; *Stein et al*., 2004]. Holocene sedimentation is facilitated by the vigorous sediment deposition from rivers and extensive coastal erosion. The most rapid sedimentation and highest sedimentation rates occur at the outer northwestern part of the Baydratskaya Bay and at the estuaries of the Ob' and Enisey Rivers (average linear Holocene sedimentation rates are ~135 cm/kyr and 27–159 cm/kyr, respectively) [*Polyak et al*., 2000; *Stein et al*., 2004].

2.2. Permafrost Settings and Gas Hydrate Stability

Reconstructions of the Barents-Kara ice sheet extent reveal that a large part of the South Kara Sea shelf was ice-free and exposed to subaerial conditions during the Late Weichselian [*Polyak et al*., 2008; *Svendsen et al*., 2004] (Figure 1a). The sustained cold temperatures to −20°C that prevailed over this extended period [*Romanovskii et al*., 2003] led to extensive and deep permafrost generation. Drilling results indicate the presence of a more than 300 m thick permafrost layer onshore Yamal Peninsula [*Melnikov and Spesivtsev*, 1995]. Subsea permafrost was discovered in individual boreholes of the South Kara Sea in water depth of up to 115 m. Modeling of permafrost generation at the South Kara Sea shelf suggests that a 275–480 m thick permafrost layer occurred during the LGM [*Portnov et al*., 2014; *Rokos et al*., 2009]. Such sustained, frozen temperatures provide ideal conditions for the formation of gas hydrates within and beneath the permafrost where methane is present (Figure 2) [*Collett et al*., 2011; *Ruppel*, 2007].

Holocene flooding of the South Kara Sea shelf provoked melting of subsea permafrost (Figure 2) [*Rokos and Tarasov*, 2007]. Models of subsea permafrost evolution suggest a permafrost thickness reduction by 51–100% over a 10.5 kyr period of submergence (Figure 2). Complete melting of submerged permafrost under relatively cold water conditions (−0.5°C) requires 10.4–20.4 kyr, dependent on the geothermal heat flux and thermal conductivities of the soils and sediments [*Portnov et al*., 2014; *Rokos et al*., 2009].

In the South Kara Sea, summer water temperature below the thermocline is usually ≤−0.5°C [*GEOS*, 1997; *Portnov et al*., 2013]. Conductivity-temperature-depth measurements (performed by I.S.Gramberg VNIIOkeangeologia)

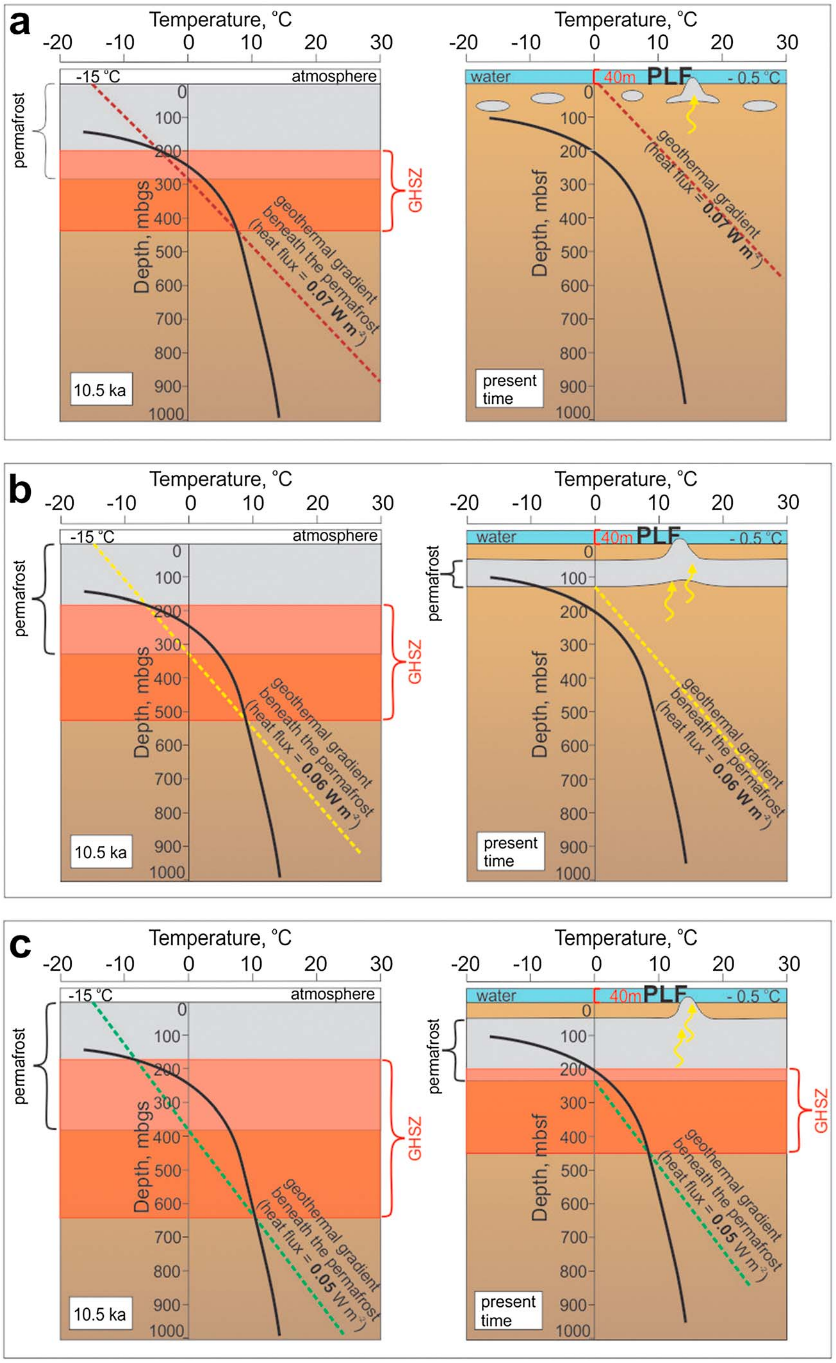

Figure 2. Scenarios of permafrost and GHSZ evolution of the South Kara Sea shelf in 40 m water depth for 10.5 ka and present time. The term ka relates to thousand years before present [*Aubry et al*., 2009]. The black curves show the phase boundary for pure methane hydrate (~99.93 methane by GC-FID) calculated in CSMHYD program [*Sloan*, 1998]. The dashed lines indicate the geotherms for different heat flux values modified from. Ground temperature for subaerial conditions is taken −15°C. Bottom water temperature is taken −0.5°C. Thicknesses of subaerial permafrost (10.5 ka) and present time submarine permafrost are modified from *Portnov et al.* [2014]. *Y* axes on the figures show depths in meters belowground surface (m bgs) and below the seafloor (m bsf). Permafrost-related GHSZ is shown for subaerial conditions (10.5 ka) and subsea conditions (present time) depending on different heat flux: (a) 0.07 W m^{-2}, (b) 0.06 W m^{-2}, and (c) 0.07 W m^{-2}.

offshore Yamal Peninsula in August 2013 revealed bottom water temperatures varying from +0.5°C in shallow water (~15 m) to −1°C in deeper water (>30 m). The Arctic and Antarctic Research Institute (AARI) database collates bottom water temperature data since the 1920s (Figure 1b), supporting these new water mass measurements. According to the AARI data and temperature-depth measurements, bottom water temperature at 40 m water depth varies from 0 to −1.0°C. Thus, shelf flooding in postglacial times has led to a significant temperature increase from −15°C to −0.5°C [*Pavlidis et al.*, 1998; *Rozenbaum and Shpolyanskaya*, 2000; *Smith and Burgess*, 2000].

Such distinct bottom water warming impacts on the subsea permafrost through thermal diffusion and eventually propagates through to the top of the gas hydrate stability zone (GHSZ) [*Sloan*, 1998]. *Portnov et al.* [2014] notes that an equilibrium temperature distribution within subsea permafrost establishes itself at ~1000 years after flooding (geothermal heat flux and bottom water temperature are taken as 0.07 W m^{-2} and −0.5°C, respectively). Differences in geothermal heat flux values significantly affect the depth path of freezing during the global sea regression and what remains from subsea permafrost thickness and GHSZ at the present time (Figure 2) [*Portnov et al.*, 2014; *Taylor et al.*, 2013; *Nicolsky et al.*, 2012]. A few existing heat flux records from the South Kara Sea shelf show values ranging from 0.054 to 0.076 W m^{-2} [*Khutorskoy and Podgornyh*, 2010].

Such variation implies contrasting scenarios of permafrost and GHSZ evolution. Under the elevated geothermal heat flux (0.07 W m^{-2}), continuous permafrost at 40 m below sea level (bsl) will have completely thawed and the corresponding GHSZ should have completely diminished (Figure 2a). Under the moderate geothermal heat flux (0.06 W m^{-2}) ~100 m thick permafrost can still exist at 40 m bsl water depths. However, its lower boundary is too shallow to provide temperatures low enough for gas hydrates to be stable (Figure 2b). Finally, under 0.05 W m^{-2} heat flux scenario permafrost may still be >150 m thick, providing intrapermafrost and subpermafrost GHSZ in the study area (Figure 2c).

The major part of subsea permafrost detected by drilling is limited by ~20 m isobath [*GEOS*, 1997; *Portnov et al.*, 2013]. However, even in the shallow water depths permafrost does not occur in every drilled borehole location, indicating that permafrost degraded heterogeneously over an extended shallow shelf area [*GEOS*, 1997; *Melnikov and Spesivtsev*, 1995]. Heterogeneous conditions of degrading permafrost are favorable for a local release of methane, which has been previously sealed by permafrost and/or gas hydrates [*Shakhova et al.*, 2013].

3. Methods

3.1. Sampling Sites and Techniques

Field studies carried out by I.S. Gramberg VNIIOkeangeologia in 2012 and 2013 on R/V “*Neotrazimy*” and R/V “*Ivan Petrov*” included HRS profiling and site-specific geological sampling in the South Kara Sea (Figure 1a).

Approximately 700 km of HRS lines were acquired using the EdgeTech 3100 SB-216S subbottom chirp operated at a frequency range of 2–16 kHz. The chirp provides at best subbottom penetration of ~80 m and vertical resolution of 20 cm in clays under calm weather conditions. The instrument setting used included a 2–15 kHz sweep with 20 ms pulse duration and 0.25 s pulse range. Depending on seabed properties and sea roughness during the cruise, the data provide ~0.5–1 m vertical resolution and 10–30 m penetration.

Based on very distinct bottom relief features we selected two well-pronounced PLFs for our detailed studies. PLF 1 is located at the West Yamal shelf in the northern part of Baydaratskaya Bay, while PLF 2 is located northward from PLF 1 (Figure 1a) above a deep structure considered for oil and gas potential [*Stupakova*, 2011].

For gravity coring we used a 250 kg weight stand with a 3 m long core barrel. Target sites for sediment coring were selected on top of PLFs and in adjacent areas. Reference core sites are located on a relatively featureless seafloor. The core positioning has been controlled by using the high-precision acoustic positioning and underwater navigation system HiPAP 350P-5. Recovered sediment cores were visually described and examined for evidence of gas or the presence of ice. Subsamples for geochemical analysis were taken from the intervals 27–33 cm, 97–103 cm, and 147–153 cm.

3.2. Laboratory Processing of Samples

For all subsampling performed on board we used conventional headspace gas extraction techniques. We placed a 100 mL plug of sediment into a 270 mL vial, containing 120 mL of distilled water. Hermetically sealed vials with previously injected argon were shaken for 5 h at 400 rpm. These gas samples were stored in 15 mL crimped vials and afterward delivered to the onshore laboratory. Samples for the extraction of high molecular weight hydrocarbons were stored on board in ziplock bags in the freezer at a temperature of −23°C.

Postcruise laboratory studies included gas chromatography–flame ionization detector (GC-FID) analyses of hydrocarbon gases and HMW hydrocarbons. Stable isotopic measurements were performed by ISOLAB (Netherlands). For compositional analyses of hydrocarbon gases we used a gas chromatograph Shimadzu GC 2014 with flame-ionized detector equipped with wide bore capillary column Restek Rt-Aluminia bond $50\,\mathrm{m} \times 0.53\,\mathrm{mm} \times 10\,\mu\mathrm{m}$. We tested the precision of the instrument by following the multiple injection method described by *Grob and Barry* [2004]. Ten injections of a standard sample, containing 10 ppm of various C_1–C_5 gases, showed an uncertainty of ±0.1 ppm. The precision of the method (repeatability) was tested by multiple runs of the identical analytical routine applied to the same sample. Estimated repeatability of the method is ±3%. This discrepancy is inevitably involved in all GC-FID results provided below.

Sample processing for analysis of HMW hydrocarbons started with a high-vacuum freeze drying and subsequent powdering of a weighted quantity. For subtracting C_{10}–C_{35} hydrocarbons we facilitated the Gerhardt SOX416 extraction system. As an internal standard we used 20 mL of squalane solution with concentration of 7.5 mg/L. After the extraction procedure we used a rotary evaporator for concentrating the samples. Gas chromatographic analyses were carried out using Shimadzu GC 2014c equipped with AOC-20i autosampler.

The $\delta^{13}C_{CH4}$ analyses were done on an Agilent 6890N GC interfaced to a Finnigan Delta S isotope ratio mass spectrometer (IRMS). For the δD measurements an Agilent 7890A GC interfaced to a MAT 253 IRMS was used. The results of carbon and hydrogen isotope measurements are expressed in terms of δ values in per mil relative to Pee Dee belemnite and SMOW standards, respectively.

4. Results

4.1. Seismic Data

HRS line spacing (~30–40 km) precludes statistically reliable estimates of the total number of PLFs that exist in the study area. However, HRS data reveal four distinct circular features, rising ~5–9 m above the surrounding seafloor at ~40 m water depth, which we classify as PLFs. Furthermore, seismic imagery reveals PLFs as acoustically transparent domes, bounded by dipping seismic reflector sequences on their flanks (Figures 1c and 1d). We subdivide these mounds into two contrasting sites: PLF1 and PLF2 (Figures 1c and 1d). PLF 1 incorporates three distinct PLFs with diameters ranging between 100 and 1000 m. PLF 2 is a smaller, yet marked, circular, singular feature with a diameter of only ~70 m. Layered sediments fill up the moats surrounding PLFs (Figures 1c and 1d).

4.2. Bottom Sediments

We recovered four sediment cores at the study area PLF 1 (Table 1). At the sites PLF_1_1 and PLF_1_6, we obtained relatively long sediment cores (210 cm and 232 cm, respectively). The sediments consisted of olive-gray bioturbated mud, which is very common for Holocene deposits throughout the Kara Sea [*Polyak et al.*, 2002]. No visible evidence existed for gas bubbling in the cores during onboard examinations. At sites PLF_1_3 and PLF_1_5, located on the flanks of the PLF, gravity core penetration was limited (Figure 3). After three repeated coring attempts at each location, two short sediment sections of 37 cm and 33 cm were retrieved. The sediments consisted of gray-colored clays with minor silt and sand contributions without indications of frozen sediment. Sediments were unable to be recovered from the top of the mound (planned coring site PLF_1_4), indicating an extremely hard seafloor and/or possibly frozen sediments. Away from the PLFs, in the outer northwestern part of the Baydaratskaya Bay, Holocene marine sediments show very high linear sedimentation rates (>100 cm/kyr) [*Polyak et al.*, 2002; *Stein et al.*, 2004].

At the PLF 2 sites, soft sediments consisted of homogeneous bioturbated olive-gray to dark gray mud (Figure 3). Only core PLF_2_4 differed, showing a 27 cm thick layer of black sediments with a very distinct hydrogen sulphide smell in its lower part. Such sediments are indicative for sulphate reduction in the sulphate-methane transition zone, beneath in which increased methane concentrations exist [*Coffin et al.*, 2008].

Table 1. Location, Water Depths, and Recovery of Gravity Cores

		Latitude		Longitude			
Study Site	Core	Minimum	Deg	Minimum	Deg	Water Depth (m)	Penetration (cm)
PLF_1	PLF_1_1	69	58.40366°N	65	18.15229°E	40	210
	PLF_1_3	69	57.87086°N	65	20.08569°E	38	37
	PLF_1_4	69	57.73125°N	65	20.55832°E	35	-
	PLF_1_5	69	57.43890°N	65	21.80662°E	39	33
	PLF_1_6	69	57.63263°N	65	21.06688°E	41	232
PLF_2	PLF_2_1	74	54.88789°N	69	43.11647°E	35	43
	PLF_2_2	74	54.92308°N	69	43.22785°E	30	99
	PLF_2_3	74	54.92806°N	69	43.24986°E	31	106
	PLF_2_4	74	54.94881°N	69	43.29353°E	36	115
	PLF_2_5	74	54.97575°N	69	43.38956°E	37	112
	PLF_2_6	74	54.99016°N	69	43.41372°E	36	187

4.3. Hydrocarbon Gases

Analyses of interstitial gases from within and around the PLFs reveal significant differences in the composition and concentration of gaseous hydrocarbons (C_1–C_5).

Methane concentrations are higher in all samples taken from PLF 2 if compared to samples taken from the same intervals in sediment cores from PLF 1 (Figure 4). PLF 1 methane concentrations at 30 cm subbottom

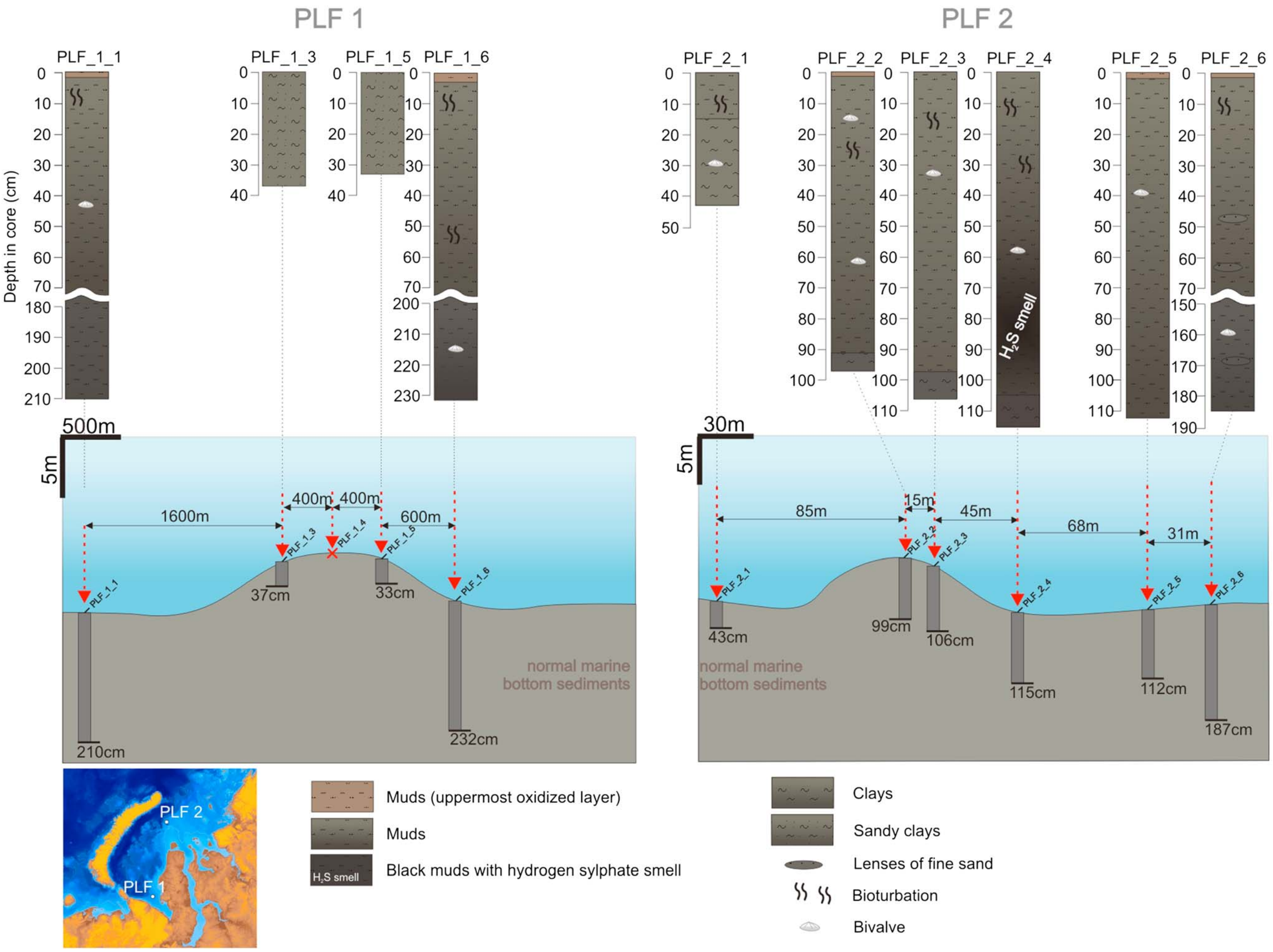

Figure 3. Locations, lengths, and lithology of investigated sediment cores.

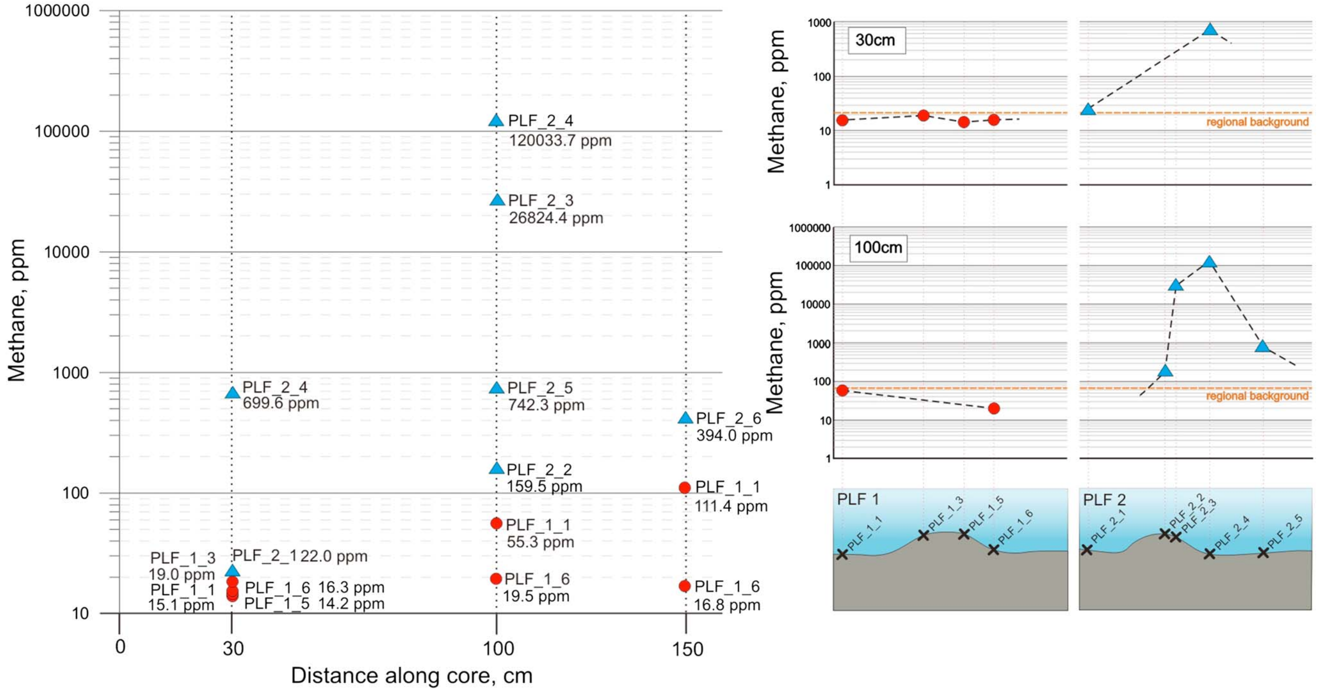

Figure 4. Methane concentrations in samples showing interstitial gas from sediment cores collected from PLF 1 and PLF 2. The red dots indicate the samples from PLF 1. The blue triangles show the samples from PLF 2.

depth (sbd) are relatively low and vary from 14.2 ppm to 19.0 ppm. In contrast, PLF 2 samples from 30 cm sbd show higher-methane concentrations reaching 22.0 ppm and 699.6 ppm, respectively (Figure 4). Similarly, methane concentrations at 100 cm sbd in the samples from PLF 1 do not exceed 55.3 ppm, while samples from PLF 2 show much higher concentrations, i.e., from 159.5 ppm to 120,033.7 ppm, respectively. Of particular note are methane concentrations in cores taken from PLF 2, which are more than 3 times higher at 150 cm sbd than in sediment cores from PLF 1 (Figure 4).

Results of grid-pattern surface geochemical investigations, performed by I.S. Gramberg VNIIOkeangeologia, documented regional background methane concentrations in the bottom sediments of the South Kara Sea shelf of less than 22 ppm at 30 cm and 60 ppm at 100 cm sbd, respectively. Thus, most of the samples taken from PLF 1 show concentrations lower than estimated background values. However, methane concentrations at PLF 2 show markedly higher values well above regional background levels (Figure 4). Site PLF_2_4 shows the highest-methane concentration of $>$120,000 ppm at 100 cm sbd, but we did not observe any gas flares in the water column using our chirp data (2–16 kHz). However, this is not conclusive because flares may actually be recorded if one uses a higher-frequency ($>$18 kHz) echo sounder [*Nikolovska et al*., 2008; *Weber et al*., 2014].

Anomalously high-methane concentrations (core PLF_2_4) are found at the PLF transition zone, between the flanks and the surrounding featureless seafloor. For example, methane concentrations around PLF 2 decrease from $>$120,000 to 26,824.4 ppm. Conversely, on the very top of the PLFs, methane concentrations are considerably lower at 159.5 ppm (Figure 4).

The fraction of total hydrocarbon gas versus wet gas [*Abrams and Dahdah*, 2011] reveals a consistent pattern with three groups of samples (Figure 5). The first group represents samples with moderate-methane concentrations (from 22.8 ppm to 743.9 ppm) and low wet gas fraction (from 0.007 to 0.04), indicative for background values. The second group shows anomalous samples with extremely high methane concentrations ($>$10,000 ppm) but low wet gas fraction (Figure 5). Finally, the third group represents fractionated samples characterized by low methane ($<$100 ppm) and increased wet gas fraction compared to background values (Figure 5). Such a pattern may be a result of differential volatile loss of methane compared to its heavier homologs, leading to a wet gas [*Abrams*, 2005].

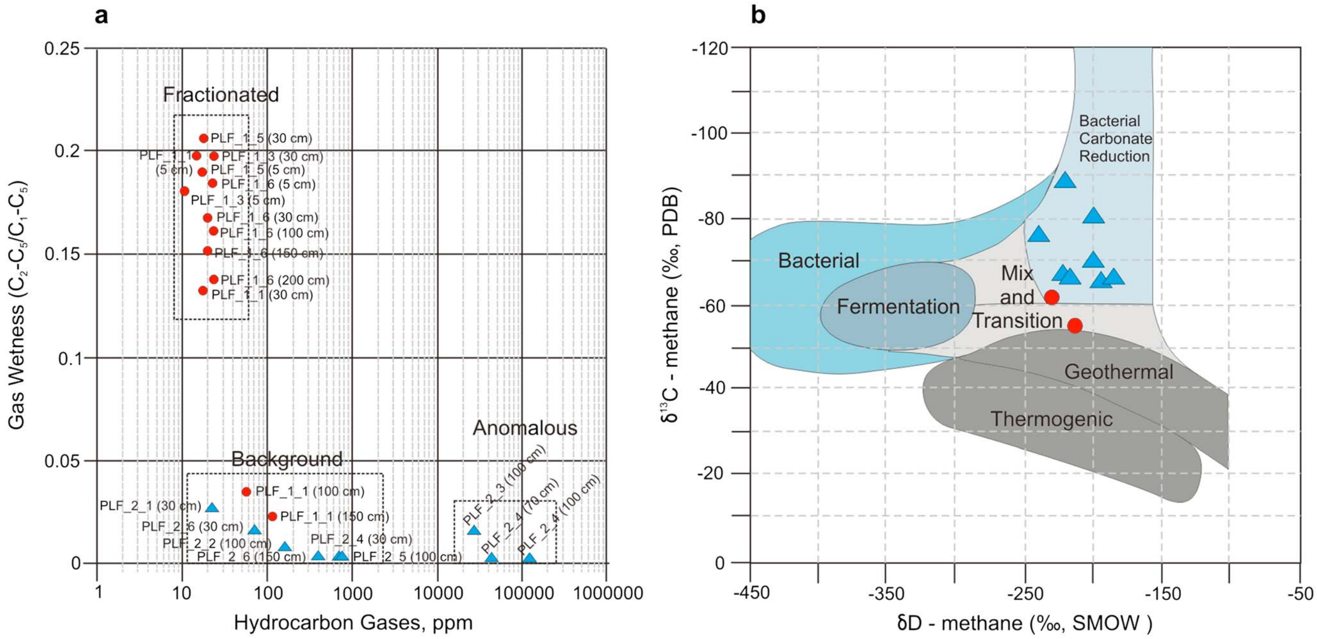

Figure 5. (a) Total extracted interstitial hydrocarbon gases (C_1–C_5) versus wet gas fraction (C_2–C_5/C_1–C_5) from sediment cores collected within PLF 1 and PLF 2. (b) CD diagram for gas genetic classifications [*Whiticar*, 1999]. The red dots show the samples from PLF 1. The blue triangles show the samples from PLF 2.

4.4. Stable Isotopes

We present the isotope data in standard δ notation (expressed in per mil) plotted on a carbon-deuterium diagram (Figure 5b) [*Whiticar*, 1999].

All studied samples demonstrate $\delta^{13}C_{CH4}$ values ranging from −55.1‰ to −88.0‰ and δD_{CH4} values ranging from −175‰ to −246‰, which is consistent with a biogenic source of methane. However, one group of samples shows a relatively heavy isotope composition of carbon from −55.1‰ to 62.1‰ (Figure 5). We suggest that these methane samples may reflect either secondary isotopic effects (substrate depletion and methane oxidation) [*Whiticar*, 1999] or a presence of trace amounts of thermogenic methane from deeper hydrocarbon sources.

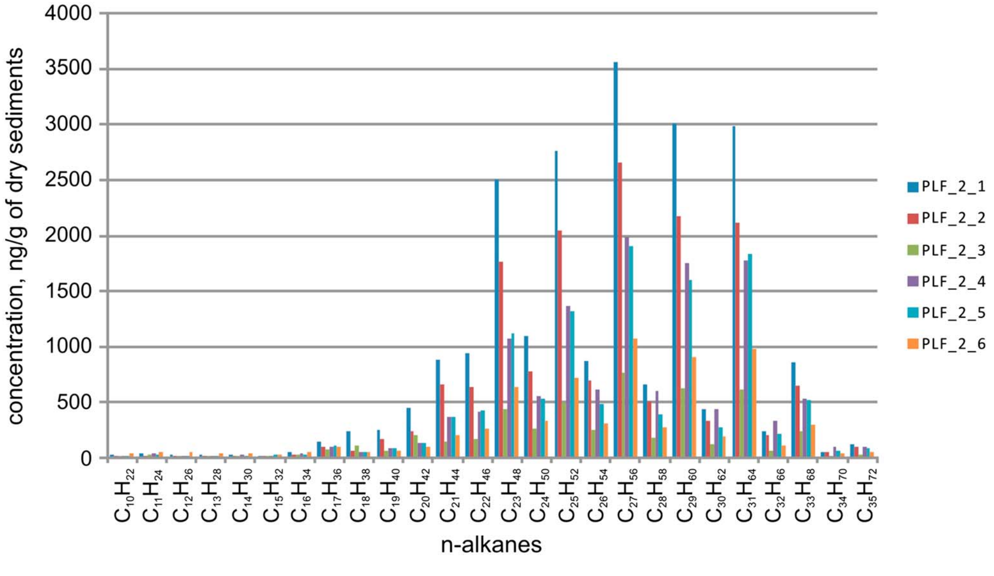

Figure 6. Distribution of *n*-alkanes extracted from the sediment core from PLF 2.

Table 2. High Molecular Weight Hydrocarbon Indexes Calculated for the Samples From PLF 2[a]

		n-Alkanes							
		ΣC_{10}–C_{40}	ΣC_{10}–C_{15}	ΣC_{16}–C_{24}	ΣC_{25}–C_{35}				
Core	TOC, %	ng/g Dry Sediments				Overall CPI	CPI_{10-15}	CPI_{16-24}	CPI_{25-35}
PLF_2_1	1.01	22,339	174.92	6,594.19	15,569.89	3.32	0.94	1.26	4.91
PLF_2_2	1.18	16,089.43	92.76	4,453.5	11,543.17	3.44	0.73	1.35	4.6
PLF_2_4	0.56	5,019.38	104.51	1,498.23	3,416.63	2.41	1.3	0.88	3.71
PLF_2_5	1.63	12,563.57	124.19	2,825.36	9,614.02	2.75	1.14	1.19	3.22
PLF_2_6	0.87	6,991.69	236.39	1,797.28	4,958.02	2.79	0.94	1.17	3.8

[a] CPI = carbon preference index; overall CPI = (ΣOdds C_{11-33} + ΣOdds C_{13-35})/2(ΣEvens C_{11-35}); $CPI_{10-15} = 0{,}5^*((C_{11} + C_{13} + C_{15})/(C_{10} + C_{12} + C_{14}) + (C_{11} + C_{13} + C_{15})/(C_{12} + C_{14} + C_{16}))$; $CPI_{16-24} = 0{,}5^*((C_{17} + C_{19} + C_{21} + C_{23})/(C_{18} + C_{20} + C_{22} + C_{24}) + (C_{17} + C_{19} + C_{21} + C_{23})/(C_{20} + C_{22} + C_{24} + C_{26}))$; and $CPI_{25-35} = 0{,}5^*((C_{25} + C_{27} + C_{29} + C_{31} + C_{33} + C_{35})/(C_{24} + C_{26} + C_{28} + C_{30} + C_{32} + C_{34}) + (C_{25} + C_{27} + C_{29} + C_{31} + C_{33} + C_{35})/(C_{26} + C_{28} + C_{30} + C_{32} + C_{34} + C_{36})$.

4.5. High Molecular Weight Hydrocarbons (*n*-Alkanes)

PLF 2 is located above a geological structure promising for oil and/or gas exploration [*Stupakova*, 2011]. The migration of gases from deeper sources to the subseabed may therefore play a role within this area. We studied HMW hydrocarbons in order to identify migrated thermogenic compounds and ascertain the nature of recent organic matter [*Abrams*, 2005; *Abrams and Dahdah*, 2011]. Shallow bottom sediments in gas leakage sites, fueled by deep and mature hydrocarbons, often show associated anomalies of high molecular weight hydrocarbons, including *n*-alkanes [*Hood et al.*, 2002; *Lorenson et al.*, 2014; *Abrams*, 2005]. Thus, we consider it essential to provide *n*-alkane data to constrain whether methane leakage is related to mature hydrocarbons.

Analyses of *n*-alkanes show that higher molecular compounds prevail in all studied cores (Figure 6). The concentration of long-chain *n*-alkanes (C_{25}–C_{35}) varies from 4958.0 to 15,569.9 ng/g of dry sediment, whereas concentrations of *n*-alkanes with shorter chains vary from 92.8 to 174.9 ng/g (C_{10}–C_{16}) and from 1498.2 to 6594.2 ng/g (C_{16}–C_{24}) of dry sediments (Figure 6 and Table 2). Bulk *n*-alkane fraction changes from 5019.4 to 22,339.0 ng/g of dry sediments (Table 2).

The carbon preference index (overall CPI), which defines the ratio between odd and even *n*-alkanes, varies from 2.35 to 3.39, indicating a predominance of odd molecules (Table 2). CPI_{16-24} and CPI_{25-35} also show a prevalence of odd *n*-alkanes (except for CPI_{16-24} in core PLF_2_4) (Table 2). Even C_{10}–C_{15} *n*-alkanes dominate in the samples from PLF_2_1, PLF_2_2, and PLF_2_6, which is reflected in low CPI_{10-15} (Table 2). However, the C_{10}–C_{15} group demonstrates insufficiently small concentrations if compared to C_{16}–C_{24} and C_{25}–C_{35} (Figure 6 and Table 2). Thus, the contribution of even C_{10}–C_{15} *n*-alkanes to the bulk composition is negligible.

5. Discussion

5.1. Beaufort Sea Shelf Pingo-Like Features

Early studies proposed a model for the origin of PLFs based on the morphological similarity and spatial proximity of terrestrial pingos and PLFs [*Shearer et al.*, 1971; *Mackay*, 1998]. These models suggested that PLFs on the Beaufort Sea shelf initially grew under subaerial conditions during the LGM sea level lowstand before ~19 ka, after which they became submerged during the Holocene transgression [*Fairbanks*, 1989; *Shearer et al.*, 1971]. However, several points contradict this hypothesis. Considering that the PLFs on the Beaufort Sea shelf are located in water depths ranging from 30 to 80 m, they should have been exposed to increased seawater temperatures for as long as ~14 to ~9 kyr [*Fairbanks*, 1989]. Moreover, open-water wave actions would have mechanically eroded the PLFs over time. Both thermal and mechanical influences of the Holocene flooding should have therefore alterated the original PLF's shape, potentially causing collapsed structures or wave undercuts at their seaward parts. However, neither early studies [*Shearer et al.*, 1971] nor recent studies that involved multibeam mapping, high-resolution seismic imaging, and remotely operated vehicle survey [*Paull et al.*, 2007] reported observations that would support such processes.

Table 3. Comparison of PLFs and Onshore Pingos From Different Regions

Criteria		Beaufort Sea PLFs	Pechora Sea PLFs	South Kara Sea PLFs	Tuktoyaktuk Pingos
Diameter	minimal	25 m	50 m	70 m	10 m
	average	400 m	-	-	20–50 m
	maximal	-	600 m	1000 m	600 m
Height	minimal	4 m	2 m	5 m	3 m
	average	10–30 m	-	-	-
	maximal	40 m	25 m	10 m	70 m
Water depths		25–70 m	50–100 m	35–45 m	onshore features
Distribution		clusters, pairs, and single features	clusters, pairs, and single features	clusters and single features	clusters, pairs, and single features
Seismic signatures		zones demonstrating lack of internal structure	acoustically transparent zones	acoustically transparent zones	-
Specific features (gas seeps, moats, collapsed structures, etc.)		negative relief moats; gas seeps at the crests of the structures	negative relief moats, overpressured gas accumulations	negative relief moats	collapsed structures, dilation cracks, and wave-eroded structures
Gas compositions		predominantly methane	-	predominantly methane	-
Isotope compositions		d^{13}C = −76.6% and dD = −179% (biogenic)	-	d^{13}C = −55.1% to −88% and dD = from −179% to −246% (biogenic)	-

Alternative hypotheses suggest that the development of PLFs occurred in submarine conditions, at places where small lakes or a freshwater supply existed for some time [*Shearer et al.*, 1971]. Sediments containing freshwater in the pore space of sediments are more prone to freezing in submarine environments. Thus, the hydrostatic pressure of expelled pore water and frost heaving might trigger upheaval [*Shearer et al.*, 1971; *Mackay*, 1998]. These scenarios require steady bottom water temperatures below the freshwater freezing point and a well-sealed freshwater lens protected from mixing with seawater. Alternatively, submarine groundwater flow from onshore may add freshwater to an aquifer that can prevent salinization of nearshore marine sediments after an ocean transgression [*Post et al.*, 2013]. Calculations of *Shearer et al.* [1971] showed that even in cases of persistently cold bottom water temperatures (below 0°C) the average time required for the 0°C isotherm to reach the lower boundary of a water-saturated lens is approximately 5 kyr. Thus, a very specific and impermeable lithology is required to keep the freshwater lens from mixing with seawater for such a long time, especially during the early stages of the Holocene transgression when wave action contributed to infiltration of seawater into soils in coastal marine environments. However, submarine discharge of groundwater can potentially cause an intrusion of freshwater into the shallow subsurface resulting in a change of the sediment pore water freezing point and, thus, PLF growths [*Frederick and Buffett*, 2015].

More recent studies have discovered methane gas seeps at the crests of many PLFs on the Beaufort Sea shelf [*Paull et al.*, 2007] (Table 3). Earlier hypotheses describing the marine inundation of terrestrial pingos therefore do not help to explain these extensive methane discharges. A scenario proposed by *Paull et al.* [2007] suggests that PLFs might be formed by decomposing permafrost-associated gas hydrates undergoing a thermal equilibration with seawater. At the top of the submerging GHSZ both methane bubbles and pure ice may exist. A transition from gas hydrate via dissociation to gas bubbling where ice may still exist provokes an expansion of the sediment matrix driving the extrusion of ice- and gas-saturated sediments toward the seafloor [*Paull et al.*, 2007]. Methane bubbles reaching the seafloor will discharge to the bottom water, with the relief of stress within the formerly gas-saturated layer and mass transfer triggering subsidence of surrounding zones and the development of moats [*Paull et al.*, 2007], similar to what has been observed in this South Kara Sea study area.

5.2. Formation of Pingo-Like Features in Areas of Thawing Subsea Permafrost

Acoustically transparent zones exist in both regions containing PLFs, as seen on HRS lines (Figures 1c and 1d). However, even HRS profiles do not allow for distinguishing between ice-saturated and gas-saturated sediments. PLF 1 has concentrations of hydrocarbon gases ubiquitously below the regional background value (19.5–55.3 ppm at 100 cm sbd), while PLF 2 represents extremely high concentrations (159.5–120,033.7 ppm at 100 cm sbd) that are much higher than the background value (60 ppm). Gas saturation might therefore induce acoustic transparency in PLF 2.

The unsuccessful gravity coring at the top of PLF 1 suggests that it is capped by a hard layer, contrary to PLF 2 where core penetration into the sediment using the same sampling technique was easily achieved (Figure 3). There is no evidence for boulders or carbonate crusts in the area around PLF 1 that could potentially hinder core penetration, although the hard bottom may be explained by the presence of frozen sediments.

PLF 1 is the largest (~1000 m in diameter and 7 m high) seabed feature within the adjacent study area and in relation to PLF 2. Moats surrounding PLFs have been previous reported from the shallow (30–80 m bsl) Beaufort Sea shelf adjacent to Tuktoyaktuk Peninsula and from the Pechora Sea shelf [*Bondarev et al.*, 2002; *Rokos*, 2008] but also from areas with terrestrial pingos [*Paull et al.*, 2007; *Mackay*, 1998] (Table 3). Taking into account the possibility of frozen sediments within the mound, and structural similarities between PLF 1 and those studied in the Beaufort and Pechora Seas, we suggest a similar origin for the South Kara Sea PLFs.

PLF 2 also exhibits a well-pronounced seabed expression (Figure 1c), but compared to PLF 1 is smaller in diameter, and singular conic-shaped. Bottom sediments of both PLF 2 and PLF 1 do not show any mudflow structures or breccia within the imaged seafloor and recovered materials. We therefore exclude the possibility of a mud volcano.

Anomalous methane concentrations were documented at PLF 2. PLF 1 lacks even background levels of methane concentrations, consistent with the presence of indurated sediments and the likely presence of ice. Frozen sediments prevent significant in situ methane production and may block any ascending flux of gas coming from deeper subsurfaces.

A low wet gas fraction in the samples from both PLFs points toward a microbial origin of gas. We interpret the increased wet gas ratio in a group of samples from PLF 1 (Figure 5a) to be a result of differentiation caused by higher volatile loss of methane compared to its heavier homologs. In general, absolute concentrations of homologs C_2–C_5 do not exceed background values and therefore do not support a focused discharge of mature gaseous hydrocarbons from a deep subsurface.

Isotope compositions of carbon and hydrogen measured in methane samples reflect a distinct microbial signature showing a good agreement with the results of GC-FID analyses (Figure 5). Two samples from PLF 2 show relatively heavy isotope compositions of carbon (Figure 5b). At the same time, they do not demonstrate any leaps in concentrations of methane and/or its heavier homologs, thus pointing toward methane that has been influenced by oxidation and/or depletion of its substrate.

The ubiquitously low content of organic matter in the bottom sediments of PLF 2 (total organic carbon (TOC) varied from 0.52% to 1.69% with an average 1.04%), as well as on the featureless seafloor (from 0.1 to 1.55% with an average 0.92%), restricts vigorous release of microbial in situ methane, pointing toward a migration of microbial gas from greater depth. However, no sites have so far been observed that show such a migration on the surrounding flat seafloor.

Results of the HMW hydrocarbons study at PLF 2 show a predominance of long chain ($>C_{23}$) odd *n*-alkanes. Thermocatalytic decomposition of organic matter during the catagenesis that is responsible for generation of oil and natural gas produces odd and even homologs in equal proportion, whereas live systems, especially plants, produce mostly odd-chained compounds [*Didyk et al.*, 1978]. Thus, a predominance of odd compounds, expressed in $\mathrm{CPI} > 2$ (Figure 6 and Table 2), strongly indicates a prevalence of terrigenous organic matter in our samples, which is typical of the Kara Sea shelf [*Boucsein et al.*, 1999]. In comparison, a thermogenic signature is usually reflected by a $\mathrm{CPI} < 1$ [*Abrams*, 2005]. Our data set suggests the absence of a thermogenic signature within C_{16}–C_{24} and C_{25}–C_{35} ranges (Table 2). The C_{10}–C_{15} range demonstrates a lower CPI, varying from 0.73 to 1.30 (Table 2). However, short-chain *n*-alkanes are present only in insignificant quantities (Figure 6 and Table 2). Results of the HMW study at PLF 2 therefore demonstrate no evidence for expulsion of mature hydrocarbons from a deep subsurface to the shallow sediments, suggesting that the observed seepage shows no relations to mature deep-sourced hydrocarbons. However, drilling data are needed to give an insight into deeper subsurface process.

Models of subsea permafrost evolution (Figure 2) suggest possible scenarios for the origin of PLF 1 and PLF 2. First, observations show that PLF1 and PLF 2 have a similar appearance on acoustic images and that the PLFs occur in similar water depths (~40 m).

The modeled boundary of the lower permafrost shows a significant upward shift in response to the geothermal heat flux (Figure 2). A permafrost evolution scenario based on an elevated heat flux of ~0.07 W m^{-2} [*Khutorskoy and Podgornyh*, 2010] corresponds with other empirical observations [*Portnov et al.*, 2014]. These heat flux would have caused a thawing and dissociation of the permafrost and GHSZ at water depths of ~40 m, an area where PLFs exist today (Figure 2a).

PLF 1 does not indicate a migration of hydrocarbon gases from deeper sources or pressurized buildups caused by growing gas accumulations. It is surprising that PLF 1 is not covered by marine sediments, because high sedimentation rates (27–159 cm/kyr) have been reported from the Kara Sea for the Holocene [*Polyak et al.*, 2000; *Stein et al.*, 2004]. Furthermore, the velocity of the Yamal Current, flowing to the northeast along the western slope of the Yamal Peninsula, is ~1 cm/s at 40 m water depth [*Zatsepin et al.*, 2010], which may not be high enough to prevent sedimentation of silt and clay. This may suggest that PLF 1 has grown more recently and thus not yet buried.

Onshore pingos, as well as the Beaufort Sea PLFs, demonstrate more solid-ice concentrations compared to surrounding permafrost [*Mackay*, 1998; *Paull et al.*, 2007]. Pure ice requires significantly more energy to melt than frozen sediments due to the larger latent heat value for pure ice relative to the bulk latent heat value of frozen sediments [*Farouki*, 1982; *Sass et al.*, 1971]. Thus, low bottom water temperatures (-0.5°C in the South Kara Sea) and high ice content may allow for a better preservation of PLFs than relic subsea permafrost.

High concentrations of hydrocarbon gases at PLF 2 cannot originate from local microbial methane production alone. Additional gas from deeper source must therefore be considered. The modeling results (Figure 2) support gas transfer from thawed subsea permafrost and dissociating gas hydrates. Focused gas leakage in the area occurs in an otherwise low in situ methane production environment as documented by low regional background values (Figure 4). A PLF formation associated with melting of both permafrost and gas hydrates is therefore very likely for the South Kara Sea shelf. We suggest that PLF 2 developed during one of the three following stages of subsea permafrost and gas hydrate evolution: stage 1—GHSZ and permafrost exist; stage 2—GHSZ disappeared, permafrost and gas-saturated layer exist; and stage 3—GHSZ disappeared, discontinuous permafrost exists (Figure 2). Previous field studies [*Portnov et al.*, 2013] and modeling results using available heat flux data [*Khutorskoy and Podgornyh*, 2010; *Portnov et al.*, 2013] provide evidence for a discontinuous permafrost in water depths $>$20 m. The studied PLFs are located in water depths of ~40 m and therefore have most likely reached stage 3.

At stage 1, the mechanism envisioned by *Paull et al.* [2007], where GHSZ was still preserved in the South Kara Sea shelf, might take place. Ongoing thermal equilibration of permafrost during transgression of the shelf post-LGM would have caused the GHSZ to largely disappear leading to stage 2. At this stage, pressurized gas below the continuous permafrost can eventually extrude ice- and methane-saturated materials from the former intrapermafrost GHSZ to the seabed. The high heat flux (0.07 W m^{-2}) below the permafrost results in a further upward shift of the permafrost base. The more the permafrost thaws, the more methane accumulates beneath it, thus driving the pinch out of thinning permafrost. The high heat flux values and our observations support extensive permafrost degradation on the South Kara Sea shelf. Therefore, we suggest that PLF started to form during the transition from stage 2 to stage 3, when a thin, but still continuous, permafrost transformed into a discontinuous layer with locally significant gas storage below (Figure 2a).

6. Conclusions

Pingo-like features (PLFs) exist across the South Kara Sea in ~40 m water depth. One PLF (PLF 2) connects to biogenic gas from deeper sources. Integrated geochemical and geophysical studies suggest that the PLFs evolved after the Last Glacial Maximum and during the Holocene sea level transgression that flooded extensive areas of the Arctic continental shelves. The formation of one PLF (PLF 2) is directly linked to the thawing of subsea permafrost and decomposition of permafrost-related gas hydrates. High accumulations of biogenic methane create the necessary forces to push the remaining frozen layers upward. We speculate that PLF 1 is either a relict-submerged terrestrial pingo or a PLF lacking the necessary underlying methane accumulations. More detailed grid-pattern HRS and drill site investigations are needed to determine the complex distribution patterns of the South Kara Sea PLFs.

Acknowledgments

All data used in this paper as well as detailed description of geochemical and geophysical methods are available upon request from the authors. This work was partly supported by the Research Council of Norway throughout its Centers of Excellence funding scheme, project 223259. The field research was supported by the Federal Subsoil Resources Management Agency of Russia (object 70-113: "Regional geologic-geophysical explorations at Yamal sector of the South Kara Sea shelf"). We would like to thank Boris Vanshtein, Georgy Cherkashev, and Svyatoslav Usenkov for their advice and recommendations during the data collection, laboratory processing, and preparation of the manuscript. We also thank anonymous reviewers and Editor Bryn Hubbard for constructive comments that greatly improved the manuscript.

References

Abrams, M. A. (2005), Significance of hydrocarbon seepage relative to petroleum generation and entrapment, *Mar. Pet. Geol.*, *22*(4), 457–477, doi:10.1016/j.marpetgeo.2004.08.003.

Abrams, M. A., and N. F. Dahdah (2011), Surface sediment hydrocarbons as indicators of subsurface hydrocarbons: Field calibration of existing and new surface geochemistry methods in the Marco Polo area, Gulf of Mexico, *AAPG Bull.*, *95*(11), 1907–1935, doi:10.1306/03211110130.

Aubry, M.-P., J. A. Van Couvering, N. Christie-Blick, E. Landing, B. R. Pratt, D. E. Owen, and I. Ferrusquia-Villafranca (2009), Terminology of geological time: Establishment of a community standard, *Stratigraphy*, *6*(2), 100–105.

Bauch, H. A., T. Mueller-Lupp, E. Taldenkova, R. F. Spielhagen, H. Kassens, P. M. Grootes, J. Thiede, J. Heinemeier, and V. V. Petryashov (2001), Chronology of the Holocene transgression at the North Siberian margin, *Global Planet. Change*, *31*(1–4), 125–139, doi:10.1016/S0921-8181(01)00116-3.

Bogoyavlenskiy, V. (2014a), Threat of catastrophic gas blowouts from the Arctic permafrost zone. Yamal and Taimyr craters. Part 1, *Oil Drill.*, *9*, 13–18.

Bogoyavlenskiy, V. (2014b), Threat of catastrophic gas blowouts from the Arctic permafrost zone. Yamal and Taimyr craters. Part 2, *Oil Drill.*, *10*, 4–8.

Bondarev, V., S. Rokos, D. Kostin, A. Dlugach, and N. Polyakova (2002), Underpermafrost accumulations of gas in the upper part of the sedimentary cover of the Pechora Sea, *Geol. Geophys.*, *43*(7), 587–598.

Boucsein, B., K. Fahl, M. Siebold, and R. Stein (1999), Quantity and quality of organic carbon in surface sediments of the Ob and Yenisei estuaries and adjacent coastal areas: Marine productivity vs. terrigenous input, *Ber. Polarforschung*, *300*, 116–126.

Brothers, L. L., P. E. Hart, and C. D. Ruppel (2012), Minimum distribution of subsea ice-bearing permafrost on the U.S. Beaufort Sea continental shelf, *Geophys. Res. Lett.*, *39*, L15501, doi:10.1029/2012GL052222.

Coffin, R., L. Hamdan, R. Plummer, J. Smith, J. Gardner, R. Hagen, and W. Wood (2008), Analysis of methane and sulfate flux in methane-charged sediments from the Mississippi Canyon, Gulf of Mexico, *Mar. Pet. Geol.*, *25*(9), 977–987, doi:10.1016/j.marpetgeo.2008.01.014.

Collett, T. S., M. W. Lee, W. F. Agena, J. J. Miller, K. A. Lewis, M. V. Zyrianova, R. Boswell, and T. L. Inks (2011), Permafrost-associated natural gas hydrate occurrences on the Alaska North Slope, *Mar. Pet. Geol.*, *28*(2), 279–294, doi:10.1016/j.marpetgeo.2009.12.001.

Delisle, G. (2000), Temporal variability of subsea permafrost and gas hydrate occurrences as function of climate change in the Laptev Sea, Siberia, *Polarforschung*, *68*, 221–225.

Didyk, B. M., B. R. T. Simoneit, S. C. Brassell, and G. Eglinton (1978), Organic geochemical indicators of palaeoenvironmental conditions of sedimentation, *Nature*, *272*(5650), 216–222.

Fairbanks, R. G. (1989), A 17,000-year glacio-eustatic sea level record: Influence of glacial melting rates on the Younger Dryas event and deep-ocean circulation, *Nature*, *342*, 637–642.

Farouki, O. (1982), Thermal properties of soils, *Tech. Rep.*, Hanover, N. H.

Fleming, K., P. Johnston, D. Zwartz, Y. Yokoyama, K. Lambeck, and J. Chappell (1998), Refining the eustatic sea-level curve since the Last Glacial Maximum using far- and intermediate-field sites, *Earth Planet. Sci. Lett.*, *163*(1–4), 327–342, doi:10.1016/S0012-821X(98)00198-8.

Frederick, J. M., and B. A. Buffett (2014), Taliks in relict submarine permafrost and methane hydrate deposits: Pathways for gas escape under present and future conditions, *J. Geophys. Res. Earth Surf.*, *119*, 106–122, doi:10.1002/2013JF002987.

Frederick, J. M., and B. A. Buffett (2015), Effects of submarine groundwater discharge on the present-day extent of relict submarine permafrost and gas hydrate stability on the Beaufort Sea continental shelf, *J. Geophys. Res. Earth Surf.*, *120*, 417–432, doi:10.1002/2014JF003349.

GEOS (1997), *Baydaratskaya Bay Environmental Conditions. The Basic Result of Studies for the Pipeline "Yamal-Center" Underwater Crossing Design*, 432 pp., GEOS, EPS "Eco-System library", Moscow.

Grob, R., and E. Barry (2004), *Modern Practice of Gas Chromatography*, 4th ed., John Wiley, Hoboken, N. J.

Hood, K. C., L. M. Wenger, O. P. Gross, and S. C. Harrison (2002), Hydrocarbon systems analysis of the northern Gulf of Mexico: Delineation of hydrocarbon migration pathways using seeps and seismic imaging, in *Surface Exploration Case Histories: Applications of Geochemistry, Magnetics, and Remote Sensing*, *AAPG Stud. Geol. 48 and SEG Geophys. Ref. Ser. 11*, edited by D. Schumacher and L. A. LeSchack, pp. 25–40, Am. Assoc. of Petrol. Geol., Tulsa, Okla.

Hovland, M., A. G. Judd, and R. A. Burke Jr. (1993), The global flux of methane from shallow submarine sediments, *Chemosphere*, *26*(1–4), 559–578, doi:10.1016/0045-6535(93)90442-8.

Hu, K., D. Issler, Z. Chen, and T. Brent (2013), Permafrost investigation by well logs, and seismic velocity and repeated shallow temperature surveys, Beaufort-Mackenzie Basin, 33 pp., Natural Resources Canada/Ressources Naturelles Canada, doi:10.4095/293120.

Jakobsson, M., et al. (2014), Arctic Ocean glacial history, *Quat. Sci. Rev.*, *92*, 40–67, doi:10.1016/j.quascirev.2013.07.033.

Judd, A. G., and M. Hovland (2007), *Seabed Fluid Flow: The Impact on Geology, Biology and the Marine Environment*, 492 pp., Cambridge Univ. Press, New York.

Khimenkov, A., and A. Brushkov (2003), *Oceanic Cryolithogenesis*, 336 pp., Nauka, Moscow.

Khutorskoy, M. D., and L. V. Podgornyh (2010), Geothermics of the Arctic basin—The problems and solutions. Geothermal field and the Arctic shelf oil and gas bearing, *Monit. Sci. Technol.*, *1*(1), 6–26.

Levitan, M. A., M. V. Bourtman, L. L. Demina, V. V. Krupskaya, E. M. Sedykh, and M. Y. Chudetsky (2004), History of Holocene sedimentation in the southern Kara Sea, *Lithol. Miner. Resour.*, *39*(6), 566–579, doi:10.1023/b:limi.0000046959.42527.71.

Lorenson, T., F. Wong, P. Dartnell, and R. Sliter (2014), Greenhouse gases generated from anaerobic biodegradation of natural offshore asphalt seepages in Southern California, *Geo Mar. Lett.*, doi:10.1007/s00367-014-0359-1.

Majorowicz, J., J. Šafanda, and K. Osadetz (2011), Gas hydrates stability and the dynamics of taliks in the Mackenzie Delta, Canada, in *Proceedings of the 7th International Conference on Gas Hydrates*, edited, pp. 1–15, Heriot-Watt Univ., Edinburgh, Scotland.

Mackay, J. R. (1998), Pingo growth and collapse, Tuktoyaktuk Peninsula area, western Arctic coast, Canada: A long-term field study, *Géographie Physique et Quaternaire*, *52*(3), 271–323, doi:10.7202/004847ar.

Melnikov, V., and V. Spesivtsev (1995), *Engineering-Geological Conditions of Barents and Kara Sea Shelves*, Nauka, Novosibirsk, Russia.

Moskvitch, K. (2014), Mysterious Siberian crater attributed to methane, *Nature*, doi:10.1038/nature.2014.15649.

Nicolsky, D. J., V. E. Romanovsky, N. N. Romanovskii, A. L. Kholodov, N. E. Shakhova, and I. P. Semiletov (2012), Modeling sub-sea permafrost in the East Siberian Arctic shelf: The Laptev Sea region, *J. Geophys. Res.*, *117*, F03028, doi:10.1029/2012JF002358.

Nikolovska, A., H. Sahling, and G. Bohrmann (2008), Hydroacoustic methodology for detection, localization, and quantification of gas bubbles rising from the seafloor at gas seeps from the eastern Black Sea, *Geochem. Geophys. Geosyst.*, *9*, Q10010, doi:10.1029/2008GC002118.

Osterkamp, T. E., G. C. Baker, W. D. Harrison, and T. Matava (1989), Characteristics of the active layer and shallow subsea permafrost, *J. Geophys. Res.*, *94*(C11), 16,227–16,236, doi:10.1029/JC094iC11p16227.

Paull, C., W. Ussler, S. R. Dallimore, S. M. Blasco, T. D. Lorenson, H. Melling, B. E. Medioli, F. M. Nixon, and F. A. McLaughlin (2007), Origin of pingo-like features on the Beaufort Sea shelf and their possible relationship to decomposing methane gas hydrates, *Geophys. Res. Lett.*, *34*, L01603, doi:10.1029/2006GL027977.

Pavlidis, Y. A., A. S. Ionin, F. A. Sherbakov, N. N. Dunaev, and S. L. Nikiforov (1998), *The Arctic Shelf. Late-Quaternary Geological History as a Framework for the Future Prognosis*, 184 pp., GEOS, Moscow.

Polyak, L., M. Levitan, V. Gataullin, T. Khusid, V. Mikhailov, and V. Mukhina (2000), The impact of glaciation, river-discharge and sea-level change on late Quaternary environments in the southwestern Kara Sea, *Int. J. Earth Sci.*, *89*(3), 550–562, doi:10.1007/s005310000119.

Polyak, L., M. Levitan, T. Khusid, L. Merkulin, and V. Mukhina (2002), Variations in the influence of riverine discharge on the Kara Sea during the last deglaciation and the Holocene, *Global Planet. Change*, *32*(4), 291–309, doi:10.1016/S0921-8181(02)00072-3.

Polyak, L., F. Niessen, V. Gataullin, and V. Gainanov (2008), The eastern extent of the Barents–Kara ice sheet during the Last Glacial Maximum based on seismic-reflection data from the eastern Kara Sea, *Polar Res.*, *27*(2), 162–174.

Portnov, A., A. J. Smith, J. Mienert, G. Cherkashov, P. Rekant, P. Semenov, P. Serov, and B. Vanshtein (2013), Offshore permafrost decay and massive seabed methane escape in water depths >20 m at the South Kara Sea shelf, *Geophys. Res. Lett.*, *40*, 3962–3967, doi:10.1002/grl.50735.

Portnov, A., J. Mienert, and P. Serov (2014), Modeling the evolution of climate-sensitive Arctic subsea permafrost in regions of extensive gas expulsion at the west Yamal shelf, *J. Geophys. Res. Biogeosci.*, *119*, 2082–2094, doi:10.1002/2014JG002685.

Post, V. E. A., J. Groen, H. Kooi, M. Person, S. Ge, and W. M. Edmunds (2013), Offshore fresh groundwater reserves as a global phenomenon, *Nature*, *504*(7478), 71–78, doi:10.1038/nature12858.

Rachold, V., D. Bolshiyanov, M. Grigoriev, H.-W. Hubberten, R. Junker, V. Kunitsky, F. Merker, P. Overduin, and W. Schneider (2007), Near-shore arctic subsea permafrost in transition, *Eos Trans. AGU*, *88*(13), 149–150, doi:10.1029/2007EO130001.

Rekant, P., and A. Vasiliev (2011), Distribution of subsea permafrost at the Kara Sea shelf, *Cryosphere Earth*, *XV*(4), 69–72.

Rekant, P., G. Cherkashev, B. Vanstein, and P. Krinitsky (2005), Submarine permafrost in the nearshore zone of the southwestern Kara Sea, *Geo Mar. Lett.*, *25*(2-3), 183–189, doi:10.1007/s00367-004-0199-5.

Rokos, S. (2008), Engineering-geological characteristics of near-surface areas of the anomaly high embedded pressure at the shelves of Pechora and Kara Seas, *Eng. Geol.*, *4*, 22–28.

Rokos, S., and G. Tarasov (2007), Gas-saturated sediments of South Kara Sea Bays and gulfs, *Bull. Stud. Quat. Period*, *67*, 66–75.

Rokos, S., A. Dlugach, A. Loktev, D. Kostin, and S. Kulikov (2009), Permafrost of the Pechora and the Kara Seas: Genesis, structure and conditions of its distribution, *Eng. Surv.*, *10*, 38–41.

Romanovskii, N. N., A. V. Gavrilov, A. L. Kholodov, G. P. Pustovoit, F. Niessen, H. Kassens, and H. W. Hubberten (1998), Map of predicted offshore permafrost distribution on the Laptev Sea shelf, in *7th International Conference on Permafrost*, *Collect. Nordicana*, edited by M. Allard and A. G. Lewkowicz, pp. 967–972, Center for Northern Studies, Univ. of Laval.

Romanovskii, N. N., H. W. Hubberten, V. E. Romanovsky, and A. L. Kholodov (2003), Permafrost evolution under the influence of long-term climate fluctuations and glacio-eustatic sea-level variation: Region of Laptev and East Siberian Seas, Russia, paper presented at 8th International Conference on Permafrost, Swets & Zeitlinger, Zurich, Switzerland.

Romanovskii, N. N., H. W. Hubberten, A. V. Gavrilov, V. E. Tumskoy, and A. L. Kholodov (2004), Permafrost of the East Siberian Arctic shelf and coastal lowlands, *Quat. Sci. Rev.*, *23*(11–13), 1359–1369, doi:10.1016/j.quascirev.2003.12.014.

Romanovskii, N. N., H. W. Hubberten, A. V. Gavrilov, A. A. Eliseeva, and G. S. Tipenko (2005), Offshore permafrost and gas hydrate stability zone on the shelf of East Siberian Seas, *Geo Mar. Lett.*, *25*(2-3), 167–182, doi:10.1007/s00367-004-0198-6.

Rozenbaum, G., and N. Shpolyanskaya (2000), Late Cenozoic history of Arctic permafrost and tendency of its evolution, *Sci. World*, Moscow.

Ruppel, C. (2007), Tapping methane hydrates for unconventional natural gas, *Elements*, *3*, 193–199.

Sass, J. H., A. H. Lachenbruch, and R. J. Munroe (1971), Thermal conductivity of rocks from measurements on fragments and its application to heat-flow determinations, *J. Geophys. Res.*, *76*(14), 3391–3401, doi:10.1029/JB076i014p03391.

Shakhova, N., I. Semiletov, I. Leifer, A. Salyuk, P. Rekant, and D. Kosmach (2010), Geochemical and geophysical evidence of methane release over the East Siberian Arctic shelf, *J. Geophys. Res.*, *115*, C08007, doi:10.1029/2009JC005602.

Shakhova, N., et al. (2013), Ebullition and storm-induced methane release from the East Siberian Arctic shelf, *Nat. Geosci.*, *7*, 64–70, doi:10.1038/ngeo2007.

Shearer, J. M., R. F. Macnab, B. R. Pelletier, and T. B. Smith (1971), Submarine pingos in the Beaufort Sea, *Science*, *174*(4011), 816–818, doi:10.1126/science.174.4011.816.

Sherbakov, V., V. Motichko, and V. Konstantinov (2010), *Estimation of Background Geological Conditions of Nearshore Area and Coastal Zone at South-West Kara Sea for Monitoring of Bowels*, *Rep. 504.4:556351(268.52)*, 270 pp., VNIIOkeangeologia, Saint-Petersburg, Russia.

Sloan, E. D. (1998), *Clathrate Hydrates of Natural Gases*, CRC Press, Taylor & Francis Group, New York.

Smith, S., and M. Burgess (2000), Ground temperature database for Northern Canada, *Open File Rep. 3954*, 28 pp., Geol. Surv. of Canada.

Stein, R., et al. (2004), Arctic (palaeo) river discharge and environmental change: Evidence from the Holocene Kara Sea sedimentary record, *Quat. Sci. Rev.*, *23*(11–13), 1485–1511, doi:10.1016/j.quascirev.2003.12.004.

Stupakova, A. (2011), Structure and petroleum potential of the Barents-Kara Shelf and adjacent territories, *Oil Gas Geol.*, *6*, 99–115.

Svendsen, J. I., V. Gataullin, J. Mangerud, and L. Polyak (2004), The glacial history of the Barents and Kara Sea Region, *Dev. Quat. Sci.*, *2*, 369–378, doi:10.1016/S1571-0866(04)80086-1.

Taylor, A. E., S. R. Dallimore, P. R. Hill, D. R. Issler, S. Blasco, and F. Wright (2013), Numerical model of the geothermal regime on the Beaufort Shelf, arctic Canada since the Last Interglacial, *J. Geophys. Res. Earth Surf.*, *118*, 2365–2379, doi:10.1002/2013JF002859.

Weber, T. C., L. Mayer, K. Jeram, J. Beaudoin, and Y. Rzhanov (2014), Acoustic estimates of methane gas flux from the seabed in a 6000 km^2 region in the Northern Gulf of Mexico, *Geochem. Geophys. Geosyst.*, *15*, 1911–1925, doi:10.1002/2014GC005271.

Whiticar, M. J. (1999), Carbon and hydrogen isotope systematics of bacterial formation and oxidation of methane, *Chem. Geol.*, *161*(1), 291–314.

Yakushev, V. S. (2009), *Natural Gas and Gas Hydrates in the Permafrost*, 192 pp., GAZPROM VNIIGAZ, Moscow.

Zatsepin, A. G., E. G. Morozov, V. T. Paka, A. N. Demidov, A. A. Kondrashov, A. O. Korzh, V. V. Kremenitsliy, S. G. Poyarkov, and D. M. Soloviev (2010), Circulation in the southwestern part of the Kara Sea in September 2007, *Oceanology*, *50*(5), 643–656.

Article 2

Pavel Serov, Sunil Vadakkepuliyambatta, Jurgen Mienert, Henry Patton, Alexey Portnov, Anna Silyakova, Giuliana Panieri, Michael L. Carroll, JoLynn Carroll, Karin Andreassen, Alun Hubbard (2017). **Postglacial response of Arctic Ocean gas hydrates to climatic amelioration.** Proceedings of the National Academy of Science of the United States of America (PNAS). DOI: 10.1073/pnas.1619288114

Postglacial response of Arctic Ocean gas hydrates to climatic amelioration

Pavel Serov[a,1], Sunil Vadakkepuliyambatta[a], Jürgen Mienert[a], Henry Patton[a], Alexey Portnov[a], Anna Silyakova[a], Giuliana Panieri[a], Michael L. Carroll[a,b], JoLynn Carroll[a,b], Karin Andreassen[a], and Alun Hubbard[a,c]

[a]Centre for Arctic Gas Hydrate, Environment and Climate, Department of Geology, University of Tromsø - The Arctic University of Norway, 9037 Tromsø, Norway; [b]Akvaplan-niva, FRAM – High North Research Centre for Climate and the Environment, 9296 Tromsø, Norway; and [c]Centre of Glaciology, Aberystwyth University, Wales SY23 3DB, United Kingdom

Edited by Mark H. Thiemens, University of California, San Diego, La Jolla, CA, and approved May 1, 2017 (received for review November 22, 2016)

Seafloor methane release due to the thermal dissociation of gas hydrates is pervasive across the continental margins of the Arctic Ocean. Furthermore, there is increasing awareness that shallow hydrate-related methane seeps have appeared due to enhanced warming of Arctic Ocean bottom water during the last century. Although it has been argued that a gas hydrate gun could trigger abrupt climate change, the processes and rates of subsurface/atmospheric natural gas exchange remain uncertain. Here we investigate the dynamics between gas hydrate stability and environmental changes from the height of the last glaciation through to the present day. Using geophysical observations from offshore Svalbard to constrain a coupled ice sheet/gas hydrate model, we identify distinct phases of subglacial methane sequestration and subsequent release on ice sheet retreat that led to the formation of a suite of seafloor domes. Reconstructing the evolution of this dome field, we find that incursions of warm Atlantic bottom water forced rapid gas hydrate dissociation and enhanced methane emissions during the penultimate Heinrich event, the Bølling and Allerød interstadials, and the Holocene optimum. Our results highlight the complex interplay between the cryosphere, geosphere, and atmosphere over the last 30,000 y that led to extensive changes in subseafloor carbon storage that forced distinct episodes of methane release due to natural climate variability well before recent anthropogenic warming.

Arctic Ocean | gas hydrate | methane release | climate change

Marine surveys of the Arctic Ocean continental shelf and slope are continuously disclosing new seafloor methane seeps associated with gas hydrate reservoirs (1–3). Gas hydrates are crystalline solids that consist of methane trapped in a lattice of hydrogen-bonded molecules of water (4). Due to their extensive distribution throughout the Arctic and elsewhere, hydrates are an integral part of a dynamic global carbon cycle (5, 6) where methane and heavier gases (i.e., ethane/propane) are sequestered and released over time. Under stable—high-pressure/low-temperature—conditions, gas hydrates constitute a potentially massive natural subseafloor carbon sink and storage capacitor. However, even under stable conditions, some ongoing methane seepage is likely to occur due to preferential fluid migration from deep, thermogenic hydrocarbon reservoirs or due to methanogenesis within organic-rich marine sediments. Despite this finding, under warming and/or depressurization, hydrate dissociation can drive large-scale natural gas release with potentially profound impacts. Abrupt episodes of methane emissions from the seafloor may attain the atmosphere (6) and thereby become a potent feedback for abrupt climate change (5, 7). Methane released into the water column also affects its geochemical signature and pH due to aerobic oxidation, leading to enhanced levels of carbon dioxide (8). However, moderate methane release is regulated by, and is also the basis for, marine chemosynthetic ecosystems that thrive in the vicinity of venting gas seeps, with new extremophiles continually discovered (9–11). Gas hydrates also sculpt and influence seafloor morphology with methane-derived carbonate crusts and pavements formed above gas venting systems, and, furthermore, hydrate dissociation within sediments has been linked to megascale submarine landslides (12), pockmarks (13), craters (14), and gas dome structures (15).

Gas and water that constitute a hydrate crystalline solid within the pore space of sediment remain stable within a gas hydrate stability zone (GHSZ) that is a function of bottom water temperature, subbottom geothermal gradient, hydrostatic and lithostatic pressure, pore water salinity, and the specific composition of the natural gas concerned. Generally, the GHSZ increases in thickness with greater water depth (4). In contrast to other Arctic regions, where gas hydrates remain stable to 300 m below sea level (mbsl), or even shallower in subsea permafrost regions (16), the modern GHSZ along the southwestern Svalbard margin appears deeper at 370 mbsl to 390 mbsl. Here, the relatively warm, ~2.7 °C northward flowing West Spitsbergen Current exerts strong control on the spatial extent and thickness of the GHSZ. It has been argued that recent warming of this current has triggered active recession of the upper GHSZ, thereby promoting enhanced methane seepage (17, 18). An alternative hypothesis suggests that seasonal variations in bottom water temperature drive fluctuations of gas hydrate decomposition and transient methane release (19). To date, gas hydrates have not been observed at or close to the upper edge of the hydrate stability zone offshore of Svalbard. Due to the largely unknown composition of gas in marine sediments coupled with a paucity of cores and actual hydrate samples, previous estimates for the GHSZ (17, 19) are based on theoretical considerations alone, which may be at odds with the actual hydrate stability conditions at the seabed. Thus, the fate of gas hydrates on the Svalbard margin in response to past, ongoing, and future oceanic warming remains unclear.

Here, we present the discovery of intensive cold seep activity clustered on the apexes of several ~500-m-wide gas hydrate-bearing domes at 370 mbsl to 390 mbsl in Storfjordrenna, northwestern Barents Sea (Fig. 1). Such formations, close to the shallow termination of the GHSZ, have rarely been observed in the Arctic, and their origin has yet to be investigated. We refer to these domes as "gas hydrate pingos" (GHPs) because they are

Significance

Shallow Arctic Ocean gas hydrate reservoirs experienced distinct episodes of subglacial growth and subsequent dissociation that modulated methane release over millennial timescales.

Author contributions: P.S., J.M., A.P., K.A., and A.H. designed research; P.S., S.V., H.P., and G.P. performed research; P.S., S.V., A.P., A.S., G.P., and M.L.C. analyzed data; and P.S., S.V., J.M., H.P., A.S., J.C., and A.H. wrote the paper.

The authors declare no conflict of interest.

This article is a PNAS Direct Submission.

[1]To whom correspondence should be addressed. Email: pavel.russerov@uit.no.

This article contains supporting information online at www.pnas.org/lookup/suppl/doi:10.1073/pnas.1619288114/-/DCSupplemental.

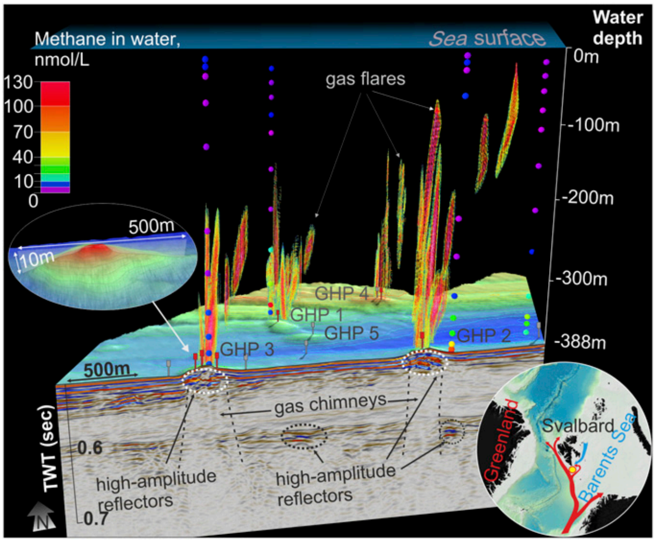

Fig. 1. Gas leakage system at Storfjordrenna. Compilation of observations, including seabed topography from high-resolution multibeam data (10-m grid cell), 2D seismic cross-section (300 Hz), and single-beam echosounder data (38 kHz) tracing streams of gas bubbles (gas flares) in the water column. Different colors within gas flares indicate backscattering strength of the reflected acoustic signals (red is the highest values, light green is the lowest). Vertical trains of large dots in the water column show locations of the water samples and, by colors, concentrations of dissolved methane measured. Red and gray marks at the seafloor indicate coring sites with and without gas hydrates, respectively. (*Inset*) Red arrow shows West Spitsbergen Current (warm Atlantic Water); blue arrow shows East Spitsbergen Current (cold Polar Water).

morphologically similar to ice-bearing onshore pingos (20) and their offshore counterparts (21, 22). Terrestrial and offshore pingos form in permafrost regions where water-saturated soils freeze and expand (20, 23). The primary difference between the permafrost-related mounds and the domes imaged here is that, instead of ice, GHPs are formed from methane-derived authigenic carbonates and gas hydrates, which render them susceptible to changes in their ambient temperature and pressure environment.

The wider Barents Sea region experienced profound subglacial temperature, pressure, and isostatic variations during the last glacial cycle (24–26). A cooling climate ~35,000 y ago initiated the growth of the marine-based Barents–Kara Sea ice sheet, providing extensive high-pressure/low-temperature subglacial conditions across the continental shelf off Svalbard (13). Analysis of sediment cores from the region reveal that the ice sheet advanced across the shelf at ~27,000 calendar (cal.) y B.P. and was at its maximum extent at the shelf break west of Svalbard by ~24,000 cal. y B.P. (27). After a prolonged period of relative stability, deglaciation commenced rapidly from ~20,000 cal. y B.P. (28, 29) onward. Hemipelagic mud present in a sediment core from Storfjordenna, some 12 km south of our GHP site, constrains local deglaciation to around 19,000 cal. y B.P. (30). The receding ice sheet left a series of grounding zone wedges and several generations of plow marks, indicating alternating phases of standstill and active, calving retreat (29). Concurrent with and promoting deglaciation, ambient Arctic water of ~1.5 °C encroached onto the shelf (30). Marine sediment $\delta^{18}O$ records reveal that, during Heinrich event 1 (H1, 15,000–13,000 cal. y B.P.), Bølling and Allerød interstadials (13,000–11,000 cal. y B.P.), and the Holocene Optimum (9,000–8,000 cal. y B.P.), Atlantic bottom water—on average 3 °C warmer—displaced the cooler ambient Arctic water body that was present immediately after deglaciation (30, 31).

Storfjordrenna's complex environmental history, and that of the wider Barents Sea shelf, raises several important questions in relation to gas hydrate storage and decomposition. Did the GHPs develop as a result of deglaciation or due to more recent ocean warming? How did the GHSZ respond to ice sheet retreat and the subsequent marine incursion of Arctic waters? When and for how long did stable gas hydrates exist during glaciation? How thick were they? Addressing these questions requires a quantitative and unified understanding of the interaction between the ice sheet, ocean, and subsurface methane hydrate reservoir over timescales spanning the last glaciation into the near future. To this end, we characterize the newly discovered site at Storfjordrenna, along with the documented recovery of gas hydrate from the Svalbard–Barents Sea shelf, to provide boundary conditions for a time-dependent coupled ice sheet/GHSZ model that describes the evolution and dynamics of the glacial and subglacial gas hydrate systems in this sector.

Gas Hydrate Pingos and Methane Venting

Five discrete GHPs were geophysically imaged within a 2.5 km^2 area on the flank of the glacially eroded cross-shelf Storfjordrenna (Fig. 1 and Fig. S1). All of the GHPs have subcircular or elongated shapes with diameters of 280 m to 450 m and heights of 8 m to 10 m. Their existence within a ground zone of vigorous paleo-ice stream activity evidenced by multiple megascale glacial lineations indicates formation after the last ice sheet retreated from the area.

Hydroacoustic observations reveal that four out of five GHPs persistently emit natural gas (Fig. 1). Gas bubbles, represented by hydroacoustic anomalies within the water column, emerge and concentrate from the topographic summits of the GHPs. The area was surveyed three times in May, July, and October 2015, and the observed gas flares were continuous, with many of them rising to at least ~200 mbsl and the largest ones rising to 20 mbsl. Undetected bubbles—those smaller than the resonance frequency of the echosounder signal (~0.6 and 0.8 mm at 20 and 200 m water depth, respectively)—cannot be discounted from breaking the ocean surface without being traced (32). Despite the lower hydrostatic pressure, rising methane bubbles gradually shrink by diffusion into the ambient water column (33, 34). Geochemical analysis indicates that gas seepage supplies the water column with up to 130 mL/L of dissolved methane (Fig. 1), some ~40 times higher than the ambient concentration. A towed camera vehicle equipped with a methane sensor surveyed 0.5 m to 2.0 m above seabed and traced concentrated plumes of dissolved methane associated with the GHPs. The location of the methane plumes along with the gas release sites coincides with the GHP summits, confirming that persistent, focused methane expulsion is closely linked to the specific morphology of each GHP (Fig. 1).

Cores acquired from the GHPs reveal that gas hydrate-bearing hemipelagic sediments with abundant carbonate concretions (Fig. S2) are present in distinct layers below the seafloor (40 cm to 70 cm and 90 cm to 120 cm below the seafloor in GHP's summits; 120 cm to 130 cm and 205 cm to 220 cm below seafloor in the GHPs' flanks). Outside the GHPs, sediments do not contain carbonate inclusions, indicating reduced or absent influx of methane. In a pattern identical to gas expulsion and flares, gas hydrates appear exclusively within the topographic highs, comprising multiple layers with different textures that include disseminated, massive, and layered hydrates that occur at various depths within the cores. Some sediment layers exhibit a liquefied, soupy material due to the dissociation of hydrates that is typically observed in recovered sediment cores where the temperature and pressure conditions have changed greatly on opening (35, 36). For all GHPs cores, the released gas was predominantly methane with an unambiguous thermogenic (i.e., depleted) isotopic signature ($\delta^{13}C_{average} = -47, n = 8$; $\delta D_{average} = -177; n = 8$) with additional low admixtures of higher methane homologs ($C1/C2-C3_{average} = 111.3$; $n = 87$) (Table S1).

High-resolution seismic data reveal deep-rooted (>150 m below seafloor) subvertical amplitude masking zones underlying each of the GHPs that we interpret as chimneys through which thermogenic-derived gas migrates upward (Fig. 1). High-amplitude reflectors around these gas chimneys indicate local accumulations of free gas, gas hydrate, or authigenic carbonates. Given these seismic data and the regional geological setting, we infer that an existing fault system within the upper Paleocene–Eocene and Pliocene–Pleistocene sedimentary rocks provides high-permeability zones for upward thermogenic gas migration from underlying hydrocarbon-rich Triassic–Jurassic formations (37–39).

Glacial History and Evolution of Gas Hydrate Stability

During the Last Glacial Maximum, a large grounded ice stream occupied Storfjordrenna and drained ice from a major accumulation center over southern Svalbard (40). Empirically constrained ice flow modeling reveals that grounded ice entered Storfjordrenna ~35,500 y ago with the onset of glaciation, overriding today's GHP site (25). Within the next 2,000 y (by ~33,500 y ago), the Storfjordrenna ice stream had advanced to the shelf break (Fig. 2*A*). During the next ~10,000 y, the ice stream was relatively stable, experiencing only minor fluctuations of the ice front, which was mostly pinned to the continental shelf edge. Ice was between 900 m and 1,000 m thick above the GHP site at this time, whereas subglacial temperatures fluctuated between −0.5 °C (the pressure-dependent melting point of ice) and −6 °C dependent on the ice stream configuration (Fig. 2*B*). Ice sheet retreat commenced around 22,500 y ago in line with global climate amelioration. The active ice stream retreated from the GHP site ~21,000 y ago, until it attained a stable position 40 km farther upstream around 18,000 y ago. Under continued atmospheric and ocean warming coupled with ongoing eustatic sea level rise, the ice stream retreated back to inner Storfjorden by 14,500 y ago.

By coupling the glacial evolution with a transient gas hydrate model (*Methods*), we underscore the tight spatial and temporal relationship between GHSZ depth in Storfjordrenna and ice sheet dynamics (Figs. 3 and 4). The GHSZ model essentially solves the conductive heat flux equations based on ambient pressure and thermal conditions provided by ice and/or ocean above and geothermal inputs from below. A more sophisticated multiphase fluid flow model could be adopted, but robust application of such a model requires accurate definition of a wide range of input parameters related to sediment and fluid properties, along with their evolution over time. Given the complex geological and environmental history at our study site, including significant episodes of glacial erosion/isostasy, compaction of sediments, subglacial and marine deposition, and formation and melting of subglacial permafrost, all of these conditions would require accurate parameterization in a multiphase model. Hence, given the available data and the environmental complexity of the study site, we reason that application of a GHSZ model is a more pragmatic and robust approach in this instance.

The GHP site and adjacent shelf were outside of the GHSZ until the onset of ice sheet advance 35,000 y ago (Figs. 2*B* and 3). Cold subglacial temperatures (−2 $^{\circ}C_{mean}$) combined with high

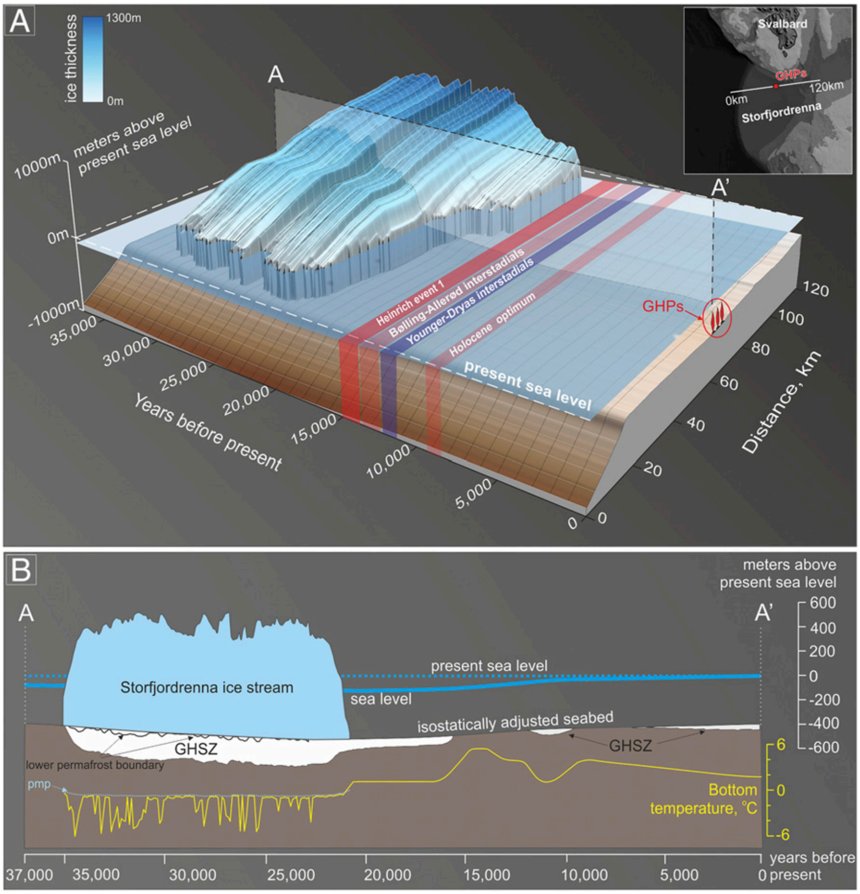

Fig. 2. Evolution of the Storfjordrenna ice stream and postglacial oceanographic changes. (*A*) Time-lapse setting of the ice stream along the line indicated in *Inset*. GHPs are not to vertical and horizontal scale. (*B*) Changes of the ice and GHSZ thickness, bottom temperature, sea level (59), and isostatically adjusted seabed at GHP site throughout the last 37,000 y.

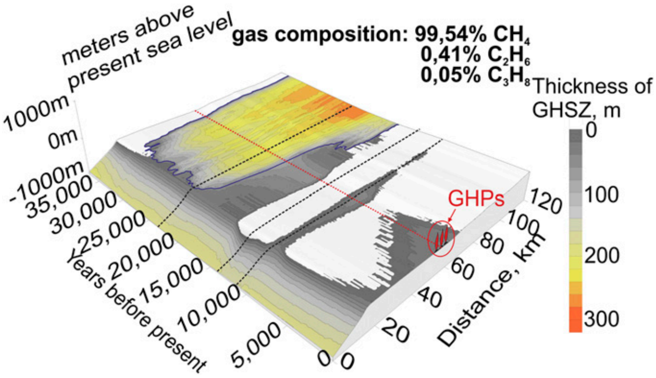

Fig. 3. Evolution of GHSZ in outer Storfjordrenna throughout the last glacial cycle. Blue line indicates contours of the ice sheet. Red dashed line shows location of GHP site. GHPs are not to vertical and horizontal scale.

overburden pressures in excess of 8 MPa (equating to 900-m overburden of ice), established a ~200-m-thick subglacial GHSZ at the GHP site that was sustained for 13,500 y. Around 30,000 y ago, the subglacial GHSZ merged with the subseafloor GHSZ on the continental slope, forming a continuous gas hydrate field across the entire region (Fig. 3). Throughout this glacial episode, the thickness of the subglacial GHSZ varied by around 20%, dependent on ice thickness, basal temperatures, and concomitant overburden pressure (Fig. 2*B*). After final deglaciation, the impact of an inherited glacio-isostatic depression of ~85 m at the GHP site promoted the preservation of a 100-m-thick GHSZ up until around 15,500 y ago (Figs. 2*B* and Fig. 3). Eventually, however, inflowing warm Atlantic Water at 4.0 °C to 5.5 °C associated with the H1 event and the Bølling–Allerød interstadials (30) combined with ongoing isostatic rebound destabilized any remnants of the GHSZ from the area (Fig. 3). Northern Hemisphere cooling during the Younger Dryas stadial at ~12,000 y ago and the incursion of the cold East Spitsbergen Current (30) initiated a second phase of gas hydrate formation with a ~60-m-thick GHSZ established across the shelf that once again connected with the persistent offshore GHSZ beneath the continental slope (Fig. 3).

Analogous to H1, the Holocene optimum was likewise associated with an intrusion of warm, ~4 °C Atlantic Water from outer Storfjordrenna, and led to a further episode of gas hydrate destabilization (Fig. 3). From 8,000 y onward, a steady transition to modern oceanographic conditions, with bottom water temperatures experiencing a steady decline from 4.0 °C to 2.0 °C, somewhat surprisingly promoted moderate gas hydrate growth at the GHP site up to the present. Today, Storfjordrenna hosts two competing water masses: warm and saline Atlantic Water and Arctic Water that is cold and fresh, the interplay of which yields strong seasonal fluctuations in bottom water temperature from 0.5 °C to 2.0 °C, dependent on prevailing synoptic conditions (41). Annual bottom water temperatures observed since the 1950s (42) have, however, remained steady, and thus gas hydrates in the area have remained stable (assuming a similar gas composition to that at the GHP site; Fig. S3).

Varying Methane Leakage Activity

Through synthesis of direct observations with hybrid ice sheet/GHSZ modeling, we demonstrate that an extensive, well-developed subglacial gas hydrate system formed across outer Storfjordrenna during the Last Glacial Maximum. This hydrate system subsequently experienced repeated cycles of reemergence/dissociation during the Late Glacial and Holocene periods driven by changes in oceanographic conditions and gradual glacio-isostatic recovery. Due to its episodic nature, the changes in the GHSZ forced distinct phases of seafloor methane expulsion. During phases when the seafloor was within the hydrate stability envelope, gas hydrate growth incorporated existing natural gas, partially filling sediment pore space and thereby reducing its permeability to ascending fluid flow. Conversely, during phases of gas hydrate decomposition, seafloor gas emissions were amplified due to hydrate-bound gas release and free gas venting from deeper thermogenic reservoirs.

The occurrence of discrete layers of methane-derived authigenic carbonates in shallow sediment cores acquired from the GHPs supports our inference of distinct phases of enhanced methane release since deglaciation. Increased methane flux induces anaerobic oxidation of methane near the seafloor, which produces excess HCO^{3-}, thereby enhancing authigenic carbonate precipitation (43, 44). Hence, high methane seepage activity associated with conditions of hydrate dissociation is favorable for carbonate precipitation.

The Barents Sea ice sheet covered the West Svalbard shelf for over 13,500 y, driving continuous gas entrapment in and beneath a thick and extensive subglacial GHSZ. On regional deglaciation, the corresponding abrupt increase in temperature and decreased pressure conditions triggered a period of thinning and shrinkage of the GHSZ (Figs. 2*B* and 3). Reduced pressure and warmer bottom waters resulted in the complete disappearance of GHSZ within <5,000 y after the ice sheet retreated from shallow regions of the seafloor. Throughout the postglacial period, a ~5-m-thick section of hemipelagic sediments containing present gas hydrates

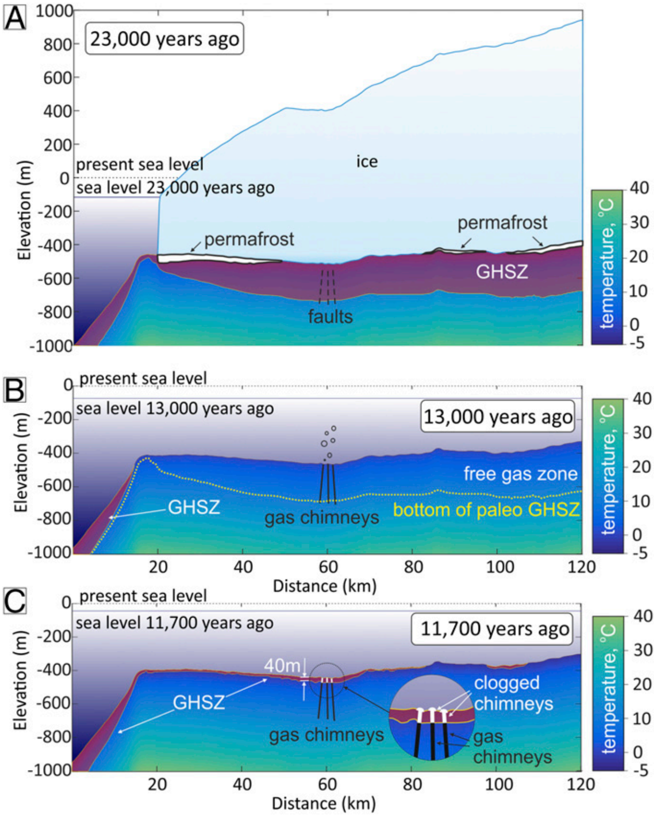

Fig. 4. Growth and collapse of GHSZ in outer Storfjordrenna. Isostatic movements, subsurface temperature distribution, GHSZ, thickness of ice, and permafrost resulted from our modeling. Gas chimneys and faults are not to vertical and horizontal scale. (*A*) Setting during the Last Glacial Maximum: ~200-m-thick GHSZ, patches of subglacial permafrost. (*B*) GHSZ-free shelf during the H1. Seabed gas efflux is unhampered. (*C*) Continuous GHSZ on the shelf by the end of the Younger Dryas Interstadial. Gas chimneys intersect with ~40-m GHSZ.

and authigenic carbonates was deposited across the seafloor (28, 30). Driven by the pronounced warming of bottom water to 5.5 °C (30) from 15,500 y ago onward, any remnant GHSZ collapsed, thereby releasing gas hydrates that had accumulated for more than 18,000 y. Decomposition of gas hydrates caused pore volume expansion and activated large-scale release of formerly hydrate-bound methane that was vented through gas chimneys in the seafloor. Laboratory experiments and numerical simulations of seabed gas dome growth indicate that buoyancy forces and the corresponding enhanced pressure from upwelling methane confined within a gas chimney are sufficient to create seabed domes of a few hundred meters in diameter (45–47). We propose that it was this excess pressure-related doming that initiated the growth of the GHPs around 15,500 y ago.

Corresponding to the Younger Dryas, a ∼1,000-y episode of oceanic cooling stimulated extensive GHSZ regrowth and the cessation of methane seepage across the shelf (Figs. 3 and 4*C*). Gas hydrate heaving, a process analogous to frost heave under permafrost conditions, also would have contributed to sediment upheaval within GHPs at this time. Successive fracturing of sediments caused by excess pore pressure would have led to cracks that eventually fill with hydrates (48), thereby leading to further GHP volume expansion.

A rapid recession of the GHSZ took place, associated with a warming period of bottom water at the Holocene Optimum (Fig. 3). From ∼6,500 y ago onward, oceanographic conditions were broadly comparable to those today, with Arctic-derived bottom waters (<2 °C) prevailing in outer Storfjordenna. These cooler oceanic conditions gradually led to the establishment of a new GHSZ up to 60 m thick that has persisted through to the present day (Fig. 3). Our analysis demonstrates that complex changes in temperature and pressure conditions led to episodic gas hydrate formation in outer Storfjordrenna, which strongly modulated seafloor methane release and the formation of authigenic carbonates and GHPs during the Late Pleistocene and Holocene.

Besides Storfjordeanna, several glacial troughs with depths in excess of 350 mbsl have been eroded into the Barents and Kara Sea shelf (Fig. 4*A*). These troughs and associated deeper shelf areas must have developed extensive GHSZ during the last glaciation that subsequently experienced episodic phases of collapse and reemergence driven by changing subglacial, isostatic, and oceanographic conditions (49–51). Given the abundance of hydrocarbon provinces within these formerly glaciated margins, we propose that the GHPs we document here could be more common and extensive across the Arctic, where submarine gas hydrate systems exist. Recent surveys off West Greenland support this proposition, where hydrate-bearing seafloor features appear to be associated with deep gas migration channels (52). Furthermore, across the East Greenland shelf, δ^{13}C records in benthic and planktonic foraminifera indicate at least three methane release episodes since deglaciation related to dissociating hydrates (53). It is also likely that many GHPs that reside outside of the present-day GHSZ have collapsed, forming large depressions, a phenomenon that has been widely reported in previously glaciated trough systems in the Arctic (13, 14, 54).

Despite considerable seafloor methane seepage from formerly glaciated Arctic shelves, the actual flux of methane that attains the atmosphere remains unconstrained. Recent studies show that a broad gas seepage area extending along the Northwestern Barents sea from 74° to 79° contributed only 0.07% to net atmospheric methane (3). This finding resonates with recent airborne measurements revealing a distinct absence of high atmospheric methane concentration during the summer (55). The role of the water column in critically regulating methane transfer to the atmosphere is not fully understood, and it remains unclear as to whether oceanic methane degradation has limits where large and abrupt fluxes of seafloor release could overcome filter systems, thereby forcing a potent atmospheric feedback, as has previously been proposed.

Earth has experienced a wide range of climate extremes over its geological history (56), such as the Permian–Triassic catastrophe 252 million years ago (57) when both carbon dioxide and methane were released on a massive scale into the atmosphere. It has recently been proposed that such an event was reinforced by global-scale hydrate dissociation and methane release triggered by initial global warming after a prolonged "Snowball Earth" glacial episode (58). Our inferences regarding a glacial gas hydrate capacitor are worth consideration when investigating the causes of past episodes of global-scale gas methane release evident in the geological record.

Despite the growing number of seep-related features that have been recently discovered across the seafloor of the Arctic, shallow gas hydrate systems remain poorly understood and documented, particularly where they have undergone a complex environmental history. This study reveals that abrupt changes in pressure and temperature conditions associated with the interplay of grounded ice, postglacial isostatic rebound, and influx of variable ocean currents all critically modulate the GHSZ, thereby driving distinct episodes of natural gas storage and release. To date, these processes have not been well described or quantified, and any attempts to understand the past and determine the future impact of Arctic methane emissions on global climate need to comprehensively account for them.

Methods

Description of methods of seismic and hydroacoustic data acquisition and processing, sediment sampling, and geochemical analyses are provided in *SI Methods*. *SI Methods* also contains an extensive description of the ice sheet model and the conductive heat flux model of GHSZ.

ACKNOWLEDGMENTS. We thank the crew of the RV *Helmer Hanssen* for their assistance in sediment and water sampling and acquisition of the seismic data. We also thank Kate Waghorn for processing 2D seismic lines. The research is part of the Centre for Arctic Gas Hydrate, Environment and Climate and was supported by the Research Council of Norway through its Centres of Excellence funding scheme Grant 223259.

1. Shakhova N, et al. (2015) The East Siberian Arctic Shelf: Towards further assessment of permafrost-related methane fluxes and role of sea ice. *Philos Trans A Math Phys Eng Sci* 373:20140451.
2. Paull CK, et al. (2015) Active mud volcanoes on the continental slope of the Canadian Beaufort Sea. *Geochem Geophys Geosyst* 16:3160–3181.
3. Mau S, et al. (2017) Widespread methane seepage along the continental margin off Svalbard - from Bjørnøya to Kongsfjorden. *Sci Rep* 7:42997.
4. Sloan ED, Koh CA (2008) *Clathrate Hydrates of Natural Gases* (CRC Press, Boca Raton, FL), 3rd Ed.
5. Dickens GR (2003) Rethinking the global carbon cycle with a large, dynamic and microbially mediated gas hydrate capacitor. *Earth Planet Sci Lett* 213:169–183.
6. Shakhova N, et al. (2014) Ebullition and storm-induced methane release from the East Siberian Arctic Shelf. *Nat Geosci* 7:64–70.
7. Thomas DJ, Zachos JC, Bralower TJ, Thomas E, Bohaty S (2002) Warming the fuel for the fire: Evidence for the thermal dissociation of methane hydrate during the Paleocene-Eocene thermal maximum. *Geology* 30:1067–1070.
8. Reeburgh WS (2007) Oceanic methane biogeochemistry. *Chem Rev* 107:486–513.
9. Bernardino AF, Levin LA, Thurber AR, Smith CR (2012) Comparative composition, diversity and trophic ecology of sediment macrofauna at vents, seeps and organic falls. *PLoS One* 7:e33515.
10. Åström EKL, Carroll ML, Ambrose WG, Jr, Carroll J (2016) Arctic cold seeps in marine methane hydrate environments: Impacts on shelf macrobenthic community structure offshore Svalbard. *Mar Ecol Prog Ser* 552:1–18.
11. Pop Ristova P, Wenzhöfer F, Ramette A, Felden J, Boetius A (2015) Spatial scales of bacterial community diversity at cold seeps (Eastern Mediterranean Sea). *ISME J* 9:1306–1318.
12. Mienert J (2009) *Encyclopedia of Ocean Sciences* (Academic, New York), 2nd Ed, pp 790–798.
13. Portnov A, Vadakkepuliyambatta S, Mienert J, Hubbard A (2016) Ice-sheet-driven methane storage and release in the Arctic. *Nat Commun* 7:10314.
14. Long D, Lammers S, Linke P (1998) Possible hydrate mounds within large sea-floor craters in the Barents Sea. *Geol Soc Lond Spec Publ* 137:223–237.
15. Koch S, et al. (2015) Gas-controlled seafloor doming. *Geology* 43:571–574.
16. Ruppel C (2007) Tapping methane hydrates for unconventional natural gas. *Elements* 3:193–199.

17. Westbrook GK, et al. (2009) Escape of methane gas from the seabed along the West Spitsbergen continental margin. *Geophys Res Lett* 36:L15608.
18. Ferré B, Mienert J, Feseker T (2012) Ocean temperature variability for the past 60 years on the Norwegian-Svalbard margin influences gas hydrate stability on human time scales. *J Geophys Res* 117:C10017.
19. Berndt C, et al. (2014) Temporal constraints on hydrate-controlled methane seepage off Svalbard. *Science* 343:284–287.
20. Mackay JR (1998) Pingo growth and collapse, Tuktoyaktuk Peninsula area, western Arctic coast, Canada: A long-term field study. *Geogr Phys Quat* 52:271–323.
21. Paull CK, et al. (2007) Origin of pingo-like features on the Beaufort Sea shelf and their possible relationship to decomposing methane gas hydrates. *Geophys Res Lett* 34: L01603.
22. Serov P, Portnov A, Mienert J, Semenov P, Ilatovskaya P (2015) Methane release from pingo-like features across the South Kara Sea shelf, an area of thawing offshore permafrost. *J Geophys Res* 120:1515–1529.
23. Shearer JM, Macnab RF, Pelletier BR, Smith TB (1971) Submarine pingos in the Beaufort Sea. *Science* 174:816–818.
24. Auriac A, et al. (2016) Glacial isostatic adjustment associated with the Barents Sea ice sheet: A modelling inter-comparison. *Quat Sci Rev* 147:122–135.
25. Patton H, Andreassen K, Winsborrow MCM, Stroeven A, Hubbard A (2016) The build-up, configuration, and dynamical sensitivity of the Eurasian ice-sheet complex to Late Weichselian climatic and oceanic forcing. *Quat Sci Rev* 153:97–121.
26. Patton H, et al. (2015) Geophysical constraints on the dynamics and retreat of the Barents Sea ice sheet as a paleobenchmark for models of marine ice sheet deglaciation. *Rev Geophys* 53:1051–1098.
27. Jessen SP, Rasmussen TL, Nielsen T, Solheim A (2010) A new Late Weichselian and Holocene marine chronology for the western Svalbard slope 30,000–0 cal years BP. *Quat Sci Rev* 29:1301–1312.
28. Rasmussen TL, Thomsen E (2015) Palaeoceanographic development in Storfjorden, Svalbard, during the deglaciation and Holocene: evidence from benthic foraminiferal records. *Boreas* 44:24–44.
29. Lucchi RG, et al. (2013) Postglacial sedimentary processes on the Storfjorden and Kveithola trough mouth fans: Significance of extreme glacimarine sedimentation. *Global Planet Change* 111:309–326.
30. Rasmussen TL, et al. (2007) Paleoceanographic evolution of the SW Svalbard margin (76°N) since 20,000 14C yr BP. *Quat Res* 67:100–114.
31. Łacka M, Zajaczkowski M, Forwick M, Szczucinski W (2015) Late Weichselian and Holocene palaeoceanography of Storfjordrenna, southern Svalbard. *Clim Past* 11: 587–603.
32. McGinnis DF, Greinert J, Artemov Y, Beaubien SE, Wüest A (2006) Fate of rising methane bubbles in stratified waters: How much methane reaches the atmosphere? *J Geophys Res* 111:C09007.
33. Greinert J, Artemov Y, Egorov V, De Batist M, McGinnis D (2006) 1300-m-high rising bubbles from mud volcanoes at 2080 m in the Black Sea: Hydroacoustic characteristics and temporal variability. *Earth Planet Sci Lett* 244:1–15.
34. Greinert J (2008) Monitoring temporal variability of bubble release at seeps: The hydroacoustic swath system GasQuant. *J Geophys Res* 113:C07048.
35. Piñero E, et al. (2007) Gas hydrate disturbance fabrics of southern Hydrate Ridge sediments (ODP Leg 204): Relationship with texture and physical properties. *Geo Mar Lett* 27:279–288.
36. Waite WF, Kneafsey TJ, Winters WJ, Mason DH (2008) Physical property changes in hydrate-bearing sediment due to depressurization and subsequent repressurization. *J Geophys Res* 113:B07102.
37. Bergh SG, Grogan P (2003) Tertiary structure of the Sørkapp-Hornsund Region, South Spitsbergen, and implications for the offshore southern extension of the fold-thrust Belt. *Nor Geol Tidsskr* 83:43–60.
38. Grogan P, et al. (1999) Structural elements and petroleum geology of the Norwegian sector of the northern Barents Sea. *Petroleum Geology of Northwest Europe: Proceedings of the 5th Conference*, eds Fleet AJ, Boldy SAR (Geol Soc, London), pp 247–259.
39. Chatterjee S, et al. (2014) The impact of lithologic heterogeneity and focused fluid flow upon gas hydrate distribution in marine sediments. *J Geophys Res Solid Earth* 119:6705–6732.
40. Ingólfsson Ó, Landvik JY (2013) The Svalbard–Barents Sea ice-sheet – Historical, current and future perspectives. *Quat Sci Rev* 64:33–60.
41. Walczowski W (2013) Frontal structures in the West Spitsbergen Current margins. *Ocean Sci* 9:957–975.
42. Boyer TP, et al. (2013) *World Ocean Database 2013* (Natl Oceanic Atmos Admin, Silver Spring, MD), Vol 72.
43. Bohrmann G, Greinert J, Suess E, Torres M (1998) Authigenic carbonates from the Cascadia subduction zone and their relation to gas hydrate stability. *Geology* 26: 647–650.
44. Hovland M, Talbot MR, Qvale H, Olaussen S, Aasberg L (1987) Methane-related carbonate cements in pockmarks of the North Sea. *J Sediment Res* 57:881–892.
45. Koch S, et al. (2015) Gas-controlled seafloor doming. *Geology* 43:571–574.
46. Barry MA, Boudreau BP, Johnson BD (2012) Gas domes in soft cohesive sediments. *Geology* 40:379–382.
47. Crémière A, et al. (2016) Timescales of methane seepage on the Norwegian margin following collapse of the Scandinavian Ice Sheet. *Nat Commun* 7:11509.
48. Pecher IA, Henrys SA, Ellis S, Chiswell SM, Kukowski N (2005) Erosion of the seafloor at the top of the gas hydrate stability zone on the Hikurangi Margin, New Zealand. *Geophys Res Lett* 32:L24603.
49. Knies J, Vogt C, Stein R (1998) Late Quaternary growth and decay of the Svalbard/Barents Sea ice sheet and paleoceanographic evolution in the adjacent Arctic Ocean. *Geo Mar Lett* 18:195–202.
50. Hald M, et al. (1999) Late-glacial and Holocene paleoceanography and sedimentary environments in the St. Anna Trough, Eurasian Arctic Ocean margin. *Palaeogeogr Palaeoclimatol Palaeoecol* 146:229–249.
51. Moros M, Jensen KG, Kuijpers A (2006) Mid-to late-Holocene hydrological and climatic variability in Disko Bugt, central West Greenland. *Holocene* 16:357–367.
52. Nielsen T, et al. (2014) Fluid flow and methane occurrences in the Disko Bugt area offshore West Greenland: Indications for gas hydrates? *Geo Mar Lett* 34:511–523.
53. Smith LM, Sachs JP, Jennings AE, Anderson DM, deVernal A (2001) Light δ^{13}C events during deglaciation of the East Greenland Continental Shelf attributed to methane release from gas hydrates. *Geophys Res Lett* 28:2217–2220.
54. Roy S, Hovland M, Noormets R, Olaussen S (2015) Seepage in Isfjorden and its tributary fjords, West Spitsbergen. *Mar Geol* 363:146–159.
55. Myhre CL, et al. (2016) Extensive release of methane from Arctic seabed west of Svalbard during summer 2014 does not influence the atmosphere. *Geophys Res Lett* 43:4624–4631.
56. Snyder CW (2016) Evolution of global temperature over the past two million years. *Nature* 538:226–228.
57. Brand U, et al. (2016) Methane Hydrate: Killer cause of Earth's greatest mass extinction. *Palaeoworld* 25:496–507.
58. Hyde WT, Crowley TJ, Baum SK, Peltier WR (2000) Neoproterozoic 'snowball Earth' simulations with a coupled climate/ice-sheet model. *Nature* 405:425–429.
59. Waelbroeck C, et al. (2002) Sea-level and deep water temperature changes derived from benthic foraminifera isotopic records. *Quat Sci Rev* 21:295–305.
60. Smith AJ, Mienert J, Bünz S, Greinert J (2014) Thermogenic methane injection via bubble transport into the upper Arctic Ocean from the hydrate-charged Vestnesa Ridge, Svalbard. *Geochem Geophys Geosyst* 15:1945–1959.
61. Blatter H (1995) Velocity and stress fields in grounded glaciers: A simple algorithm for including deviatoric stress gradients. *J Glaciol* 41:333–344.
62. Hubbard A (2000) The verification and significance of three approaches to longitudinal stresses in high–resolution models of glacier flow. *Geogr Ann Ser A* 82:471–487.
63. Hubbard A (1999) High-resolution modeling of the advance of the Younger Dryas ice sheet and its climate in Scotland. *Quat Res* 52:27–43.
64. Hindmarsh RCA (2004) A numerical comparison of approximations to the Stokes equations used in ice sheet and glacier modeling. *J Geophys Res* 109:F01012.
65. Brown CS, Meier MF, Post A (1982) Calving speed of Alaska tidewater glaciers, with application to Columbia Glacier. *US Geol Soc Prof Pap:* 1258:C1–C13.
66. Weertman J (1972) *Glaciers and Glacial Erosion*, ed Embleton C (Macmillan, London), pp 244–268.
67. Pollack HN, Hurter SJ, Johnson JR (1993) Heat flow from the Earth's interior: Analysis of the global data set. *Rev Geophys* 31:267–280.
68. Le Meur E, Huybrechts P (1996) A comparison of different ways of dealing with isostasy: Examples from modeling the Antarctic ice sheet during the last glacial cycle. *Ann Glaciol* 23:309–317.
69. Andersen KK, et al.; North Greenland Ice Core Project members (2004) High-resolution record of Northern Hemisphere climate extending into the last interglacial period. *Nature* 431:147–151.
70. Phrampus BJ, Hornbach MJ (2012) Recent changes to the Gulf Stream causing widespread gas hydrate destabilization. *Nature* 490:527–530.
71. Darnell KN, Flemings PB (2015) Transient seafloor venting on continental slopes from warming-induced methane hydrate dissociation. *Geophys Res Lett* 42:10,765–10,772.

Article 4

Wei-Li Hong, Marta E. Torres, JoLynn Carroll, Antoine Cre´mie`re, Giuliana Panieri, Haoyi Yao, Pavel Serov (2017). **Seepage from an arctic shallow marine gas hydrate reservoir is insensitive to momentary ocean warming.** *Nature Communications*. DOI: 10.1038/ncomms15745

nature COMMUNICATIONS

ARTICLE

Received 2 Jun 2016 | Accepted 25 Apr 2017 | Published 7 Jun 2017 DOI: 10.1038/ncomms15745 OPEN

Seepage from an arctic shallow marine gas hydrate reservoir is insensitive to momentary ocean warming

Wei-Li Hong[1,†], Marta E. Torres[2], JoLynn Carroll[1,3], Antoine Crémière[4,†], Giuliana Panieri[1], Haoyi Yao[1] & Pavel Serov[1]

Arctic gas hydrate reservoirs located in shallow water and proximal to the sediment-water interface are thought to be sensitive to bottom water warming that may trigger gas hydrate dissociation and the release of methane. Here, we evaluate bottom water temperature as a potential driver for hydrate dissociation and methane release from a recently discovered, gas-hydrate-bearing system south of Spitsbergen (Storfjordrenna, ~380 m water depth). Modelling of the non-steady-state porewater profiles and observations of distinct layers of methane-derived authigenic carbonate nodules in the sediments indicate centurial to millennial methane emissions in the region. Results of temperature modelling suggest limited impact of short-term warming on gas hydrates deeper than a few metres in the sediments. We conclude that the ongoing and past methane emission episodes at the investigated sites are likely due to the episodic ventilation of deep reservoirs rather than warming-induced gas hydrate dissociation in this shallow water seep site.

---

[1] CAGE—Centre for Arctic Gas Hydrate, Environment and Climate, Department of Geosciences, UiT The Arctic University of Norway, Tromsø N-9037, Norway. [2] CEOAS, Oregon State University, Corvallis 97331, Oregon, USA. [3] Akvaplan-niva AS, Fram Centre, Tromsø N-9296, Norway. [4] Geological Survey of Norway, Trondheim 7491, Norway. † Present addresses: Geological Survey of Norway, 7491 Trondheim, Norway (W.-L.H.); Jet Propulsion Laboratory, California Institute of Technology, Pasadena, California 91109, USA (A.C.). Correspondence and requests for materials should be addressed to W.-L.H. (email: wei-l-hung@uit.no).

Gas hydrate is an ice-like compound that is stable under high pressure and low temperature conditions. Dissociating 1 litre of fully saturated gas hydrate releases 169 of methane under atmospheric pressure[1]. Arctic gas hydrate reservoirs are estimated to hold 100–500 gigatons of carbon[2,3], more than 10% of the carbon in global gas hydrate reservoirs[2]. Current models predict a high potential of Arctic gas hydrate dissociation if bottom water temperatures increase by two degrees during the next century[3]. Indeed, gas hydrate dissociation due to a 1 °C warming of bottom water has been hypothesized to explain hydroacoustic flares observed in water depths shallower than 400 m west of Prins Karls Forland (PKF)[4]. However, the recent recovery of carbonate crusts from PKF points to a longer history of gas venting[5].

Excluding the permafrost area in the Arctic Ocean, gas hydrate recovery has been achieved in water depth at 740 m in the Canadian Beaufort Sea[6] and of 1,200 m water depth at Vestnesa Ridge in Fram Strait[7]. To date, there has been no recovery of gas hydrates in the shelf/slope region of the Arctic, such as PKF[4,5], the shelf area of the Beaufort Sea[8] and the Barents Sea[9,10], regions where increasing bottom water temperatures are thought to have the largest influence on gas hydrate stability. Gas hydrates have only been inferred from the presence of bottom simulating reflectors in seismic data from these areas[8,10]. The hypothesis that Arctic methane seepage is enhanced by warming-triggered gas hydrate dissociation cannot be fully evaluated without direct evidence for the presence of gas hydrates in these warming-sensitive regions.

Here, we present and model the porewater data from a recently discovered shallow water cold seep south of Svalbard. The porewater profiles exhibit concave-up shapes, an indication of an evolving and non-steady-state environment[11–13]. Sulfate profiles are used as a proxy for the activity of anaerobic oxidation of methane (AOM)[14], which in turn responds to methane ascending from deeper sediment towards the sediment-water interface. Using transport-reaction models to simulate the temporal development of the porewater system, we investigate the potential mechanisms leading to the concave-up sulfate profiles, and conclude that these are due to increases in methane flux. The model results also indicate that the timing for the latest methane pulse varies significantly among the investigated sites, suggesting that such events do not respond to regional perturbations such as bottom water warming. Nonetheless, we examine whether bottom water warming can be a plausible mechanism as proposed by previous studies[2–4]. We present evidence to show that short-term warming has limited impact on the gas hydrate stability at the investigated area. Collectively, our results indicate that the ongoing and past methane emission events in this region likely reflect the natural state of a fluid system that is controlled by the state properties of gas reservoirs, the episodic opening of fluid conduits and potential self-sealing by gas hydrate and/or carbonate concretions, as shown in gas hydrate provinces elsewhere[15–18].

Results

Description of sediment and porewater profiles. Here, we describe a group of gas-hydrate-bearing mounds in the slope area south of Svalbard (Storfjordrenna, ~380 m water depth, Fig. 1a and Table 1). The mounds are ~500 m in diameter and extend ~10 m in height above the seafloor. Hydroacoustic imaging of bubble plumes in the water column, commonly referred to hydroacoustic flares (Fig. 1b), and visual observations of bubble streams rising from the seafloor confirm active methane seepage in this area. We reported the sediment and porewater data from seven gravity cores and one multi core recovered during two expeditions in May and October 2015 (Fig. 1c, Table 1 and Supplementary Fig. 1). Core IDs will be abbreviated throughout the text ignoring the cruise number. Gas hydrates were observed in three of the cores (911GC, 912GC and 1520GC) with the shallow-most recovery at 0.85 m below seafloor (mbsf). We therefore term these mound-like structures, ‘Gas Hydrate Mounds (GHMs)’. Microfractures, commonly attributed to gas expansion during core recovery, were observed in the three cores with gas hydrate as well as in cores 940GC and 1521GC (Supplementary Fig. 1). Basic information and the available data from these sediment cores can be found in Table 1. In five of the cores, we observed discrete authigenic carbonate nodules. Their mineralogy and carbon isotopic composition are listed in Supplementary Table 1.

We establish an age model with two ^{14}C dates of planktonic foraminifera from a background core 1522GC (Supplementary Table 2) and Zr/Rb ratio from X-ray fluorescence (XRF) core scanning for stratigraphic correlation (Fig. 2). Zr/Rb ratio is a proxy for sediment grain size[19], which is not affected by methane-derived diagenesis. The presence of oxidized layers in cores 920GC, 940GC and 1522GC (as shown in Fig. 2 and Supplementary Fig. 1) adds additional constraints to this age model using literature attributions to these changes described in other cores from the region[20]. From the two ^{14}C dates, we estimate a sedimentation rate of $2.21(\pm 0.009)\times 10^{4}\,\mathrm{m\,yr^{-1}}$ between the sediment depths of 0.71 and 2.21 mbsf. On the basis of our stratigraphic correlation, we conclude that, between *ca.* 9 and 16 kyrBP, at least four of the sites experienced similar sedimentation rates. The short recovery in other four sites precludes correlations with the rest of the cores. However, based on Zr/Rb profiles, we speculate that sediment in these sites (911GC, 912GC, 1521GC and 904MC) is younger than Pleistocene. We also notice that, some of the sites may experience more intensive erosion than the others as their upper sediments (920GC, 1520GC and 1522GC) are apparently older relative to the top of 940GC. Notwithstanding, the slightly varied but similar depositional characteristics among the sites exclude the influence of major sedimentation events, such as mass transport deposits (MTDs).

An unusual observation from the porewater profiles is the non-steady-state shape of the SO_4^{2-}, ΣHS, total alkalinity (TA), Ca^{2+} and Mg^{2+} profiles at three of the coring sites from one active GHM (Fig. 3), similar to the ‘kink-type’ profiles described in Hensen *et al.*[11]. Above the kinks, the concentrations of these ions show little deviation from bottom seawater values, whereas these solute concentrations increase or decrease rapidly within a narrow depth range below the kinks. Such structure is however absent from the NH_4^+ whose concentration shows a gradual increase with no apparent kink in all the coring sites. Porewater data from 920GC, a currently inactive GHM (Fig. 1a), are included to illustrate the smooth profiles typical of a steady-state system (Fig. 3).

Discussion

There are many published explanations for the presence of non-steady-state porewater profiles in marine sediments worldwide[21]. To find the most plausible explanation for our observations, we simulated five different scenarios with a comprehensive transport-reaction model that considers 15 primary porewater species, seven mineral phases and six redox reactions (Fig. 4; see Methods for modelling details). This model is constrained by the measurements of seven key porewater species (SO_4^{2-},ΣHS, TA, Fe^{2+}, Ca^{2+}, Mg^{2+} and NH_4^+). The scenarios we considered are: irrigation and seawater intrusion due to biological, physical and hydrological processes[12,22] (Scen1);

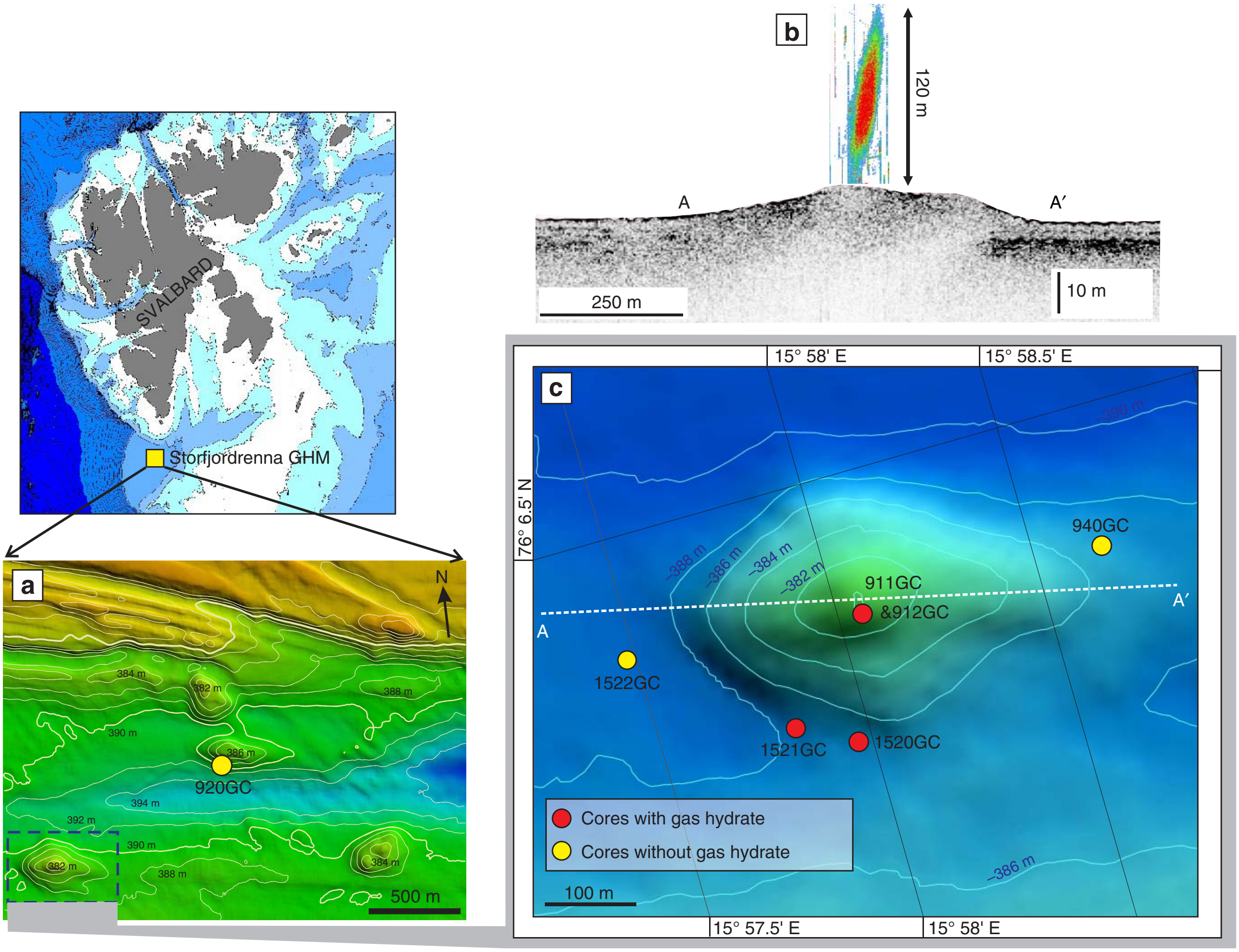

Figure 1 | Bathymetry and core location from Storfjordrenna gas hydrate mounds. (**a**) Bathymetry of the Storfjordrenna gas hydrate mounds (GHMs) area. 920GC in **a** shows the location of a coring site with steady-state porewater profiles (Fig. 3). (**b**) The hydroacoustic flare observed only from the summit of the mound. AA′ indicates the line of hydroacoustic survey as marked in **c** which shows the detailed bathymetry of the studied GHM. We recovered gas hydrates from three of the study sites (red dots). Notice the different distance scales for the AA′ transects in **b**,**c**.

Table 1 | Location, water depth and recovery of the eight studied sediment cores.

CORE ID	Water depth (m)	Recovery (m)	Lat	Lon	X-ray/XRF	Authigenic carbonate	Porewater
CAGE15-2-904MC	377	0.40	76.1072 N	15.9679 E	v	v	v
CAGE15-2-911GC	379	0.85	76.1069 N	15.9677 E	v	v	v
CAGE15-2-912GC	380	1.04	76.1067 N	15.9686 E	v	NA	NA
CAGE15-2-920GC	386	2.50	76.1117 N	16.0108 E	v	NA	v
CAGE15-2-940GC	386	3.10	76.1069 N	15.9779 E	v	v	v
CAGE15-6-1520GC	386	2.90	76.1057 N	15.9661 E	v	v	v
CAGE15-6-1521GC	386	0.95	76.1060 N	15.9638 E	v	v	NS
CAGE15-6-1522GC	388	3.20	76.1071 N	15.9579 E	v	ND	NS

NA, not analysed; ND, not detected; NS, not shown; v, data presented.

changes in sedimentary properties, such as sedimentation rate[11,13] (Scen2) and porosity (Scen3); and changes in methane flux[23] (Scen4). Although strong upwards advection of fluid is unlikely to result in the observed curvatures in our porewater profiles, we still considered a scenario with an advection component to simulate its impact on the porewater profiles (Scen5).

In Scen1, we initiated the model with a shallow SMTZ (grey lines of Scen1 in Fig. 4). Fluid with bottom seawater composition intrudes into surficial sediments by advection, which results in the observed concave-up sulfate profile (blue lines of Scen1 in Fig. 4). Our model can reproduce the observed sulfate profile with a downwards fluid advection rate of 1 m yr^{-1} in 3 months, a similar rate and timescale to what were reported elsewhere[12,24,25]. However, the modelled NH_4^+ profile is significantly lower than what is measured due to the dilution from seawater. Such results help us exclude this explanation.

In Scen2, we assumed the top 30 cm of the sediments was initially a layer of MTD with homogenized porewater and sediment composition, which are identical to the composition of

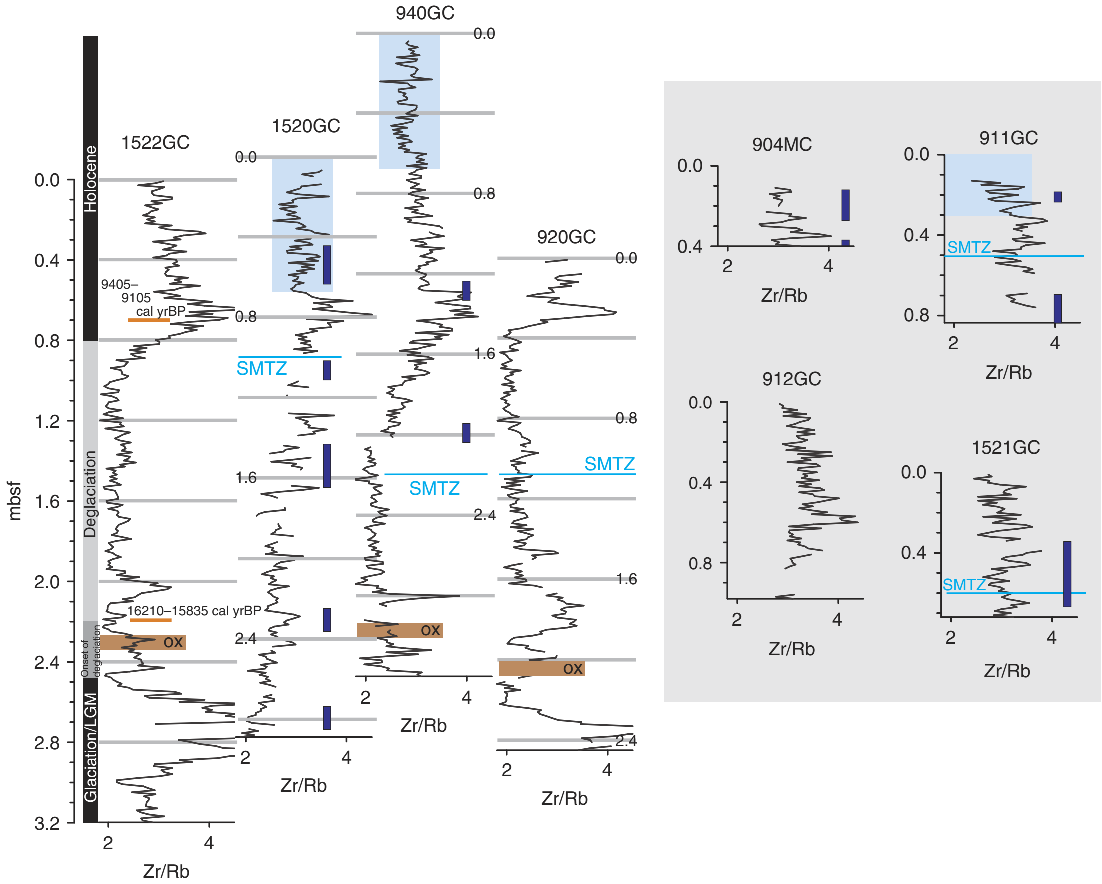

Figure 2 | Age model for the studied sediment cores. We compiled Zr/Rb ratio from XRF core scanning, the observations of oxidized layers, and two ^{14}C dating from planktonic foraminifera to establish the age model for our coring sites. A sedimentation rate of $2.21(\pm 0.009)\times 10^{4}\,\mathrm{m\,yr^{-1}}$ was estimated between 0.71 and 2.21 mbsf at 1522GC. Oxidized layers observed in cores 920GC, 940GC and 1522GC provide an additional constraint for our stratigraphic correlation. The four cores with <1-m recovery (904MC, 911GC, 912GC and 1521GC), are not well constrained, however, based on the Zr/Rb ratios, we speculate their age to be younger than the Pleistocene. Depths of SMTZ at each core were defined by the sulfate concentration profiles. Approximated depths of authigenic carbonate nodules observed from these cores were indicated by the dark blue bars (see Supplementary Table 1 for values and exact depths). The light blue rectangles covering the Zr/Rb profiles mark the depth ranges of seawater-like porewater.

bottom seawater and seafloor sediments (grey lines in Scen2 of Fig. 4). Six months after the initial condition, diffusion gradually smoothes the profile to the currently observed sulfate profile. With this scenario, we can reproduce most of the porewater profiles but not Fe^{2+}, NH_4^+ and ΣHS. As we assumed that the MTD was composed of oxidized sediments with abundant iron hydroxide, the oxidized iron is soon reduced to Fe^{2+} that precipitates as pyrite with hydrogen sulfide, a different scenario from what we have observed. Furthermore, within the 6-month period of simulation, organic matter degradation is not rapid enough to release the observed level of NH_4^+. Not only this model scenario fails to explain the porewater profiles, our age model (Fig. 2) indicates no such abrupt sedimentation event.

In Scen3, we evaluated the case with contrasting low porosity in the sediments. We assumed sediments with very low porosity (50%) were deposited for nine centuries. Such deposition results in a 27.5-cm layer of low porosity barrier with the sedimentation rate we assigned. The grey lines of Scen3 in Fig. 4 show the simulation results without such low porosity layer on top, while the blue lines show the results with a low porosity barrier. We observed that such low porosity barrier results in concave-downwards porewater profiles that are different from what we observed. Such porosity contrast is also not expected based on the Cl ratio obtained from XRF core scanning from our sites, which was used as a proxy for water content[26,27] (Supplementary Fig. 2). These results exclude such explanation for our profiles.

In Scen4, we simulated the case with an increasing methane flux. The simulation results show that an elevated methane flux can deflect the porewater profiles of SO_4^{2-},ΣHS, TA, Fe^{2+}, Ca^{2+} and Mg^{2+} while not affecting the profile of NH_4^+, in agreement with our observations (Fig. 4). We therefore conclude this is the most likely scenario to explain the observed profiles among the four scenarios. Although such model assessment was only performed on the data from 911GC/904MC, we can attribute the same conclusion to 940GC and 1520GC based on the similarity in their porewater profiles (Fig. 3).

In our last scenario (Scen5), we assumed an upwards aqueous advection rate of $1\,\mathrm{m\,yr^{-1}}$ to investigate how the porewater profiles will be impacted. A high methane flux was also assigned to this scenario. To fit the measured NH_4^+ profile, we assigned a lower concentration for the initial condition of NH_4^+. We observed a 'S-shaped' sulfate profile due to both the high methane flux and advection rate. Concaved downwards profiles were observed from Ca^{2+}, and Mg^{2+} (only Ca^{2+} profile is shown), which are different from the measured profiles. By adding such advective component to our model, we are not able to fit most of our porewater profiles. We therefore conclude that aqueous advection is a less significant process compared to diffusion at our study sites and cannot explain our observations in porewater profiles.

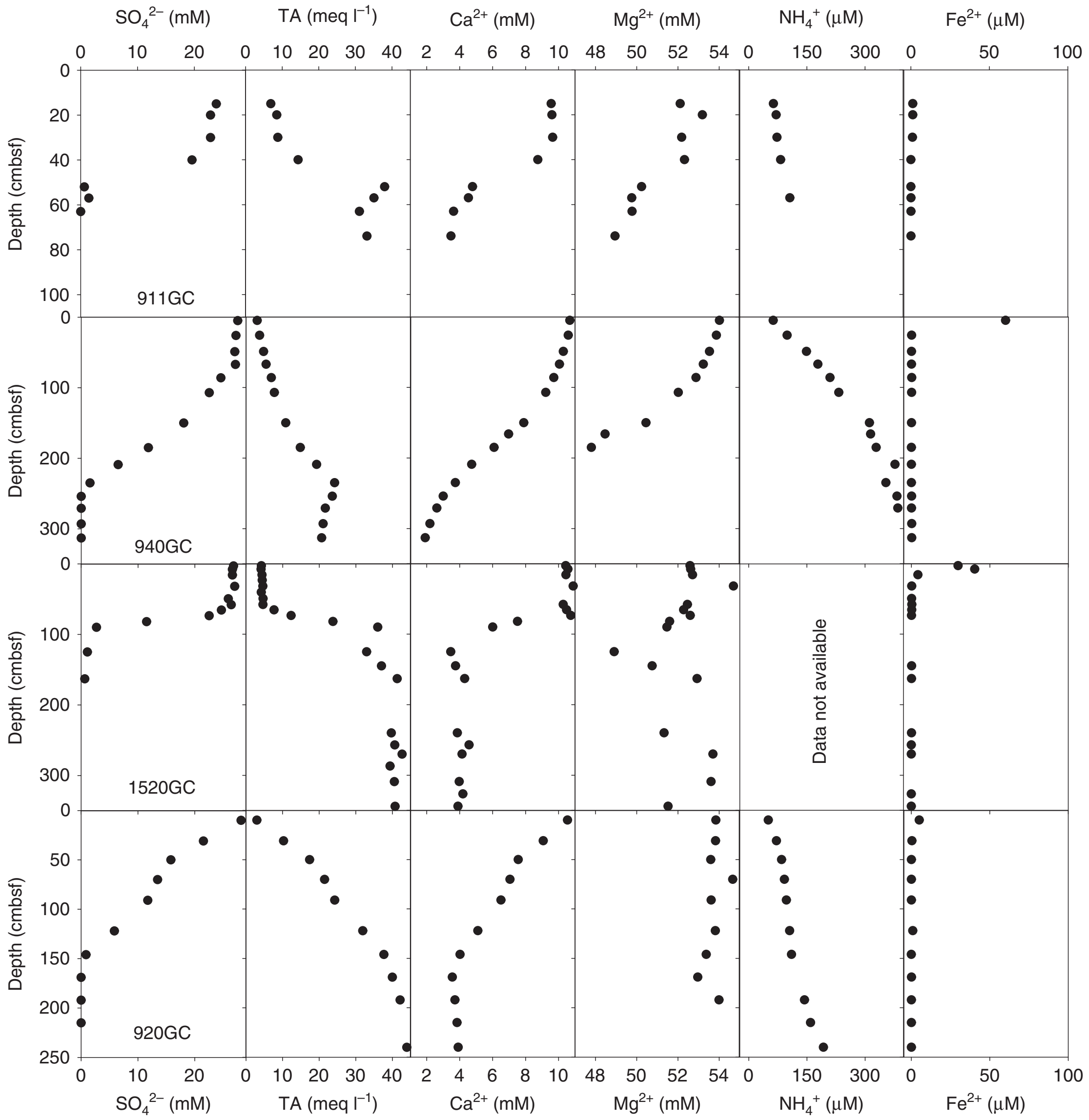

Figure 3 | Porewater data from four selected cores. The profiles of sulfate, ΣHS, TA, calcium and magnesium reveal a system out of steady state at three of the sites. Ammonium concentrations at these three sites show smooth profiles without any apparent kinks. We include porewater data from core 920GC to illustrate a steady-state system in the vicinity of the investigated active gas hydrate mound.

As a step further, we aim to estimate the relative timing of changes in methane flux as this information will be valuable for determining its triggering mechanism. If the flux of methane increases at the same time across the investigated GHM, then the system must be responding to regional forcing, such as bottom seawater warming-triggered gas hydrate dissociation. On the other hand, if the timing of methane pulses varies among the investigated sites that are only a few hundred metres apart, then we can conclude that the triggering mechanism must have high geographical heterogeneity.

To estimate the timing of the methane pulses, we simulated the evolution of sulfate profiles at the three coring sites with non-steady-state profiles as they evolve from an initial steady-state situation. As this simulation has to include the entire sediment column above the gas hydrate stability zone (GHSZ), it is computationally too challenging to implement our comprehensive model. We therefore use a reduced model that focuses exclusively on sulfate. This reduced model assumes that sulfate profiles above the kinks are relics of the profiles when the methane supply was weak, for example, 0–0.65 mbsf at 1520GC (Fig. 3). We derived the initial conditions for each site by executing the same reduced model and adjusting the methane supply from the base of the GHSZ until the results fit the shallow part of the sulfate profile (see Methods section for details). We assume a purely diffusional porewater system with AOM as the only reaction.

By matching our simulations with the observed sulfate profiles, we find that the latest increase in methane supply at the GHM summit was initiated fairly recent (160–340 years at 911GC), and is later than the pulses at its southern (290–630 years at 1520GC) and eastern (1900–4100 years at 940GC) flanks (Fig. 5). From the modelled methane concentration profiles, we can also infer the depths where methane concentration exceeds its saturation in porewater (as calculated by CSMGem[1]). These depths, as shown in Fig. 5, are above the shallowest occurrence of gas hydrates (from cores 911GC to 1520GC) and correspond to the shallowest depth where microfractures were observed in the sediments (Supplementary Fig. 1), a feature that reflects gas expansion during core recovery of sediments with high methane content. Such results suggest that not only does the currently observed

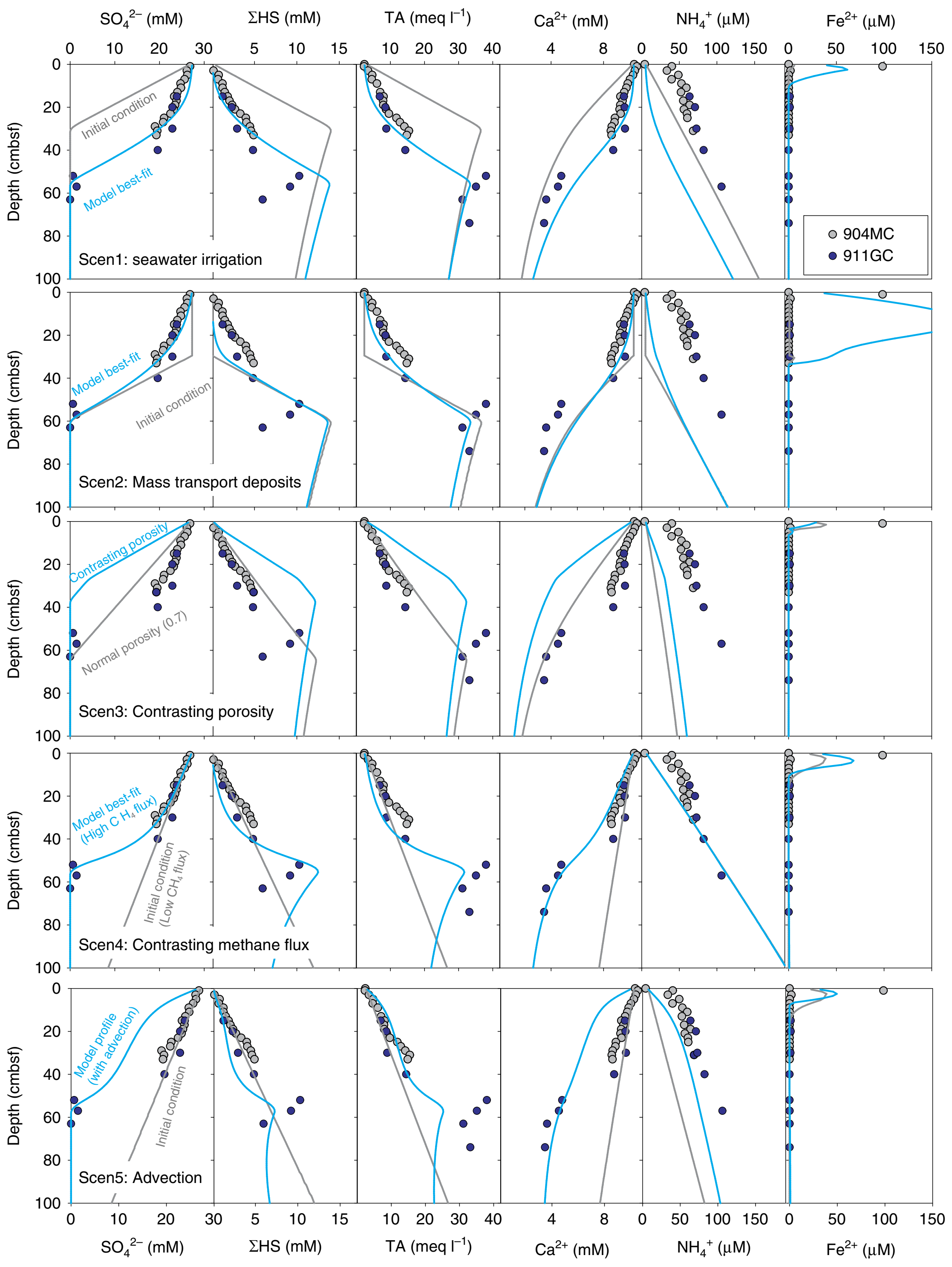

Figure 4 | Simulation results from five scenarios that may explain the non-steady-state profiles. We applied a comprehensive model to investigate the cause of the non-steady-state profiles. The first two scenarios (Scen1 and Scen2) can reproduce the kinks in some porewater data but fail to fit the ammonium and iron profiles. Scen3 is dedicated to simulate the porewater profiles with significant porosity contrast which is not expected. The model results fail to fit the observed profiles. Only with an increase in methane flux (Scen4), we can fit all porewater profiles with the model. Aqueous advection (Scen5) will result in concave-downwards profiles for sulfate, calcium and magnesium, which were not observed. We therefore conclude that advection is not significant at the investigated sites.

Storfjordrenna GHM seepage began before the onset of the Anthropocene but the seepage timing differs by orders of magnitude among sites located only a few hundred metres apart. Such results point to triggering mechanisms that are heterogeneous in space and may operate over geological timescales.

Our time estimates may be compromised by not including an advective component in the model. Advection will accelerate the ascending of methane and shorten the time required to achieve the observed concave-up sulfate profiles. As the measured porewater profiles do not correspond to those simulated with

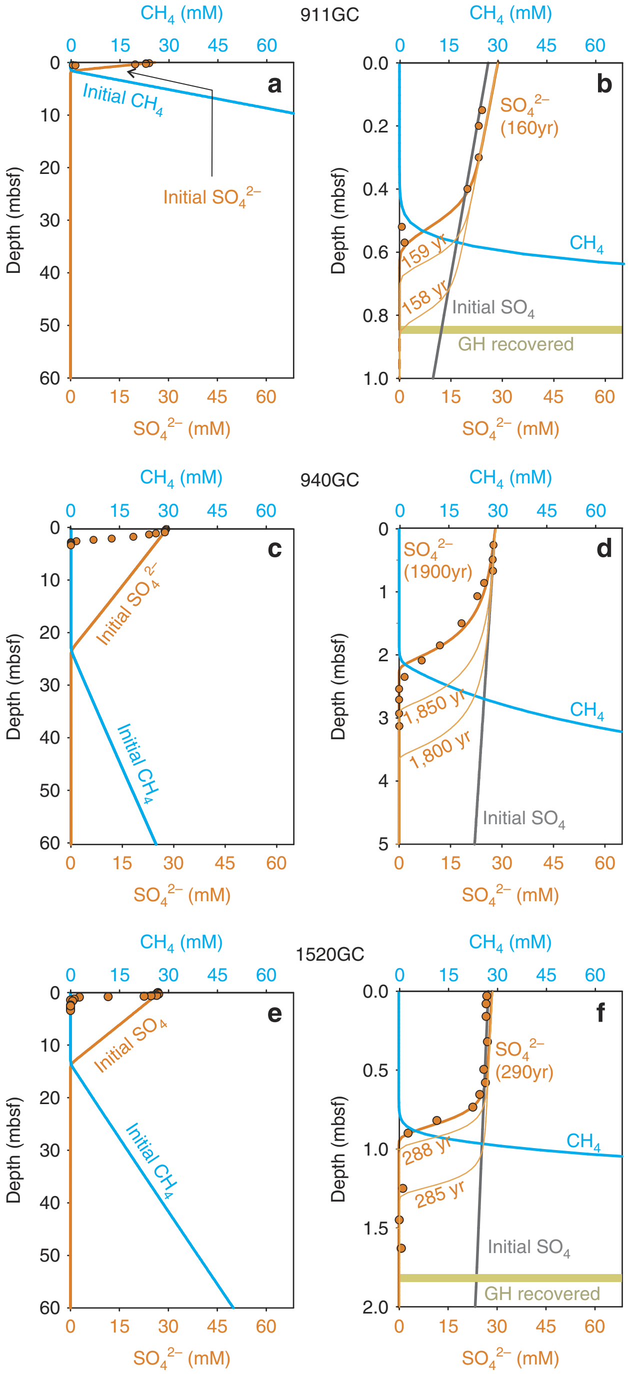

Figure 5 | Simulation of non-steady-state porewater profiles for the timing of methane seepages. We applied the reduced model on 911GC (**a**,**b**), 940GC (**c**,**d**) and 1520GC (**e**,**f**) to estimate the timing of seepage. Orange lines in **a**, (**c**,**e**) are initial sulfate concentrations used in the model which are identical to the black lines in **b**, (**d**,**f**) for the corresponding depth. These initial conditions were constrained by the shallow part of the measured sulfate profiles (orange dots in all panels) where concentration gradients are small. Blue lines in **a**, (**c**,**e**) are initial profiles for methane whereas the blue lines in **b**, (**d**,**f**) are model output for methane, which were also constrained by the first appearance of gas hydrates (yellow bars). Evolution of the modelled sulfate profiles (tortuosity equals to 1.5) at each site were presented in **b**, (**d**,**f**). The rate of evolution largely depends on the rate of sulfate consumption through anaerobic oxidation of methane, which is fastest at 911GC and slowest at 940GC. Model results reflect differences in the timescales of methane seepage among the three coring sites that are in geographical vicinity.

advection (Scen5 in Fig. 4), we conclude that whereas methane gas is clearly migrating upwards, there is no significant component of aqueous advection at our sites. This is consistent with the observation that the solute profiles in sites with gas discharge (911GC) and those without any evidence of active bubbling (for example, 940GC and 1520GC) can both be simulated with a diffusion-based approach. Decoupling between a gas phase transport dominated by advection concurrent with solute distributions that are dominated by diffusion have been documented in other gas hydrate systems[28]. Our time estimates based on the assumption of a solute diffusion is therefore reasonable.

From our time estimates based on porewater simulations, we infer that the triggering mechanism for a methane flux increase cannot be explained by warming-induced gas hydrate dissociation due to the contrasting timescales within a small region. Nonetheless, as ocean warming has been postulated to drive gas hydrate dissociation along the Svalbard slope region[4], we simulated the propagation of bottom water temperature into the sediments. We aim to elucidate both the depth and the time duration of sediment exposure to temperatures exceeding the gas hydrate phase boundary (see Methods section for model details).

For the past century, the Storfjordrenna area experienced seasonal fluctuations in bottom water temperature from −1.8 to 4.6 °C with occasional anomalies up to 5.5 °C (Fig. 6a, data from World Ocean Database[29]; see Supplementary Table 3 for different data choosing criteria) in response to the dynamic interaction between the warmer Atlantic water and colder Arctic water along the polar front[30]. No apparent warming is observed from Fig. 6a although we acknowledge the scarcity of temperature measurements in the past two decades. The bottom water temperature we measured during the two cruises in May and October 2015 lies within the historical values indicating no obvious temperature anomalies during the months when the studied cores were recovered.

Assuming a sinusoidal fluctuation in seasonal bottom water temperatures over the observed temperature range, our seafloor heat propagation model shows that seasonal temperature fluctuations only affect the gas hydrate shallower than 1.65 mbsf (Fig. 6h). In May, sub-bottom temperatures above 1.1 mbsf are above the temperature threshold for gas hydrate stability (Fig. 6f) while, in October, gas hydrate is within stability field for the entire sediment column (Fig. 6k). Gas hydrates were recovered from 0.85 (911GC) to 2.9 mbsf (1520GC) during these 2 months suggesting that gas hydrate dynamics do not respond quickly to the seasonal temperature fluctuations. Furthermore, our exercise shows that gas hydrates present in sediments deeper than 1.65 mbsf will stay within the stability field throughout the year. This observation again rules out warming-induced gas hydrate dissociation as the cause for the methane flux increase at the investigated coring sites, since our simulations show that the methane pulse responsible for the observed non-steady-state sulfate profiles originates below the current SMZT (0.5–2.2 mbsf, Fig. 3).

We also examined the temperature sensitivity of the system with two different warming trends (Fig. 7). In this model exercise, in addition to the sinusoidal fluctuations in seasonal temperature, a steady increase in mean temperature was assigned to account for the warming in bottom water temperature. We assume an annual warming of 0.033 °C for 30 years in our fast warming case[4] (Fig. 7a). By comparing the assigned temperature fluctuations with the compiled temperature data between 1951 and 1981, the assigned temperatures in summer are comparable to the record temperature for the first decade but are ~1–2 °C higher than the record temperature after *ca.* 1965. The model results show that even with such fast warming, most of the

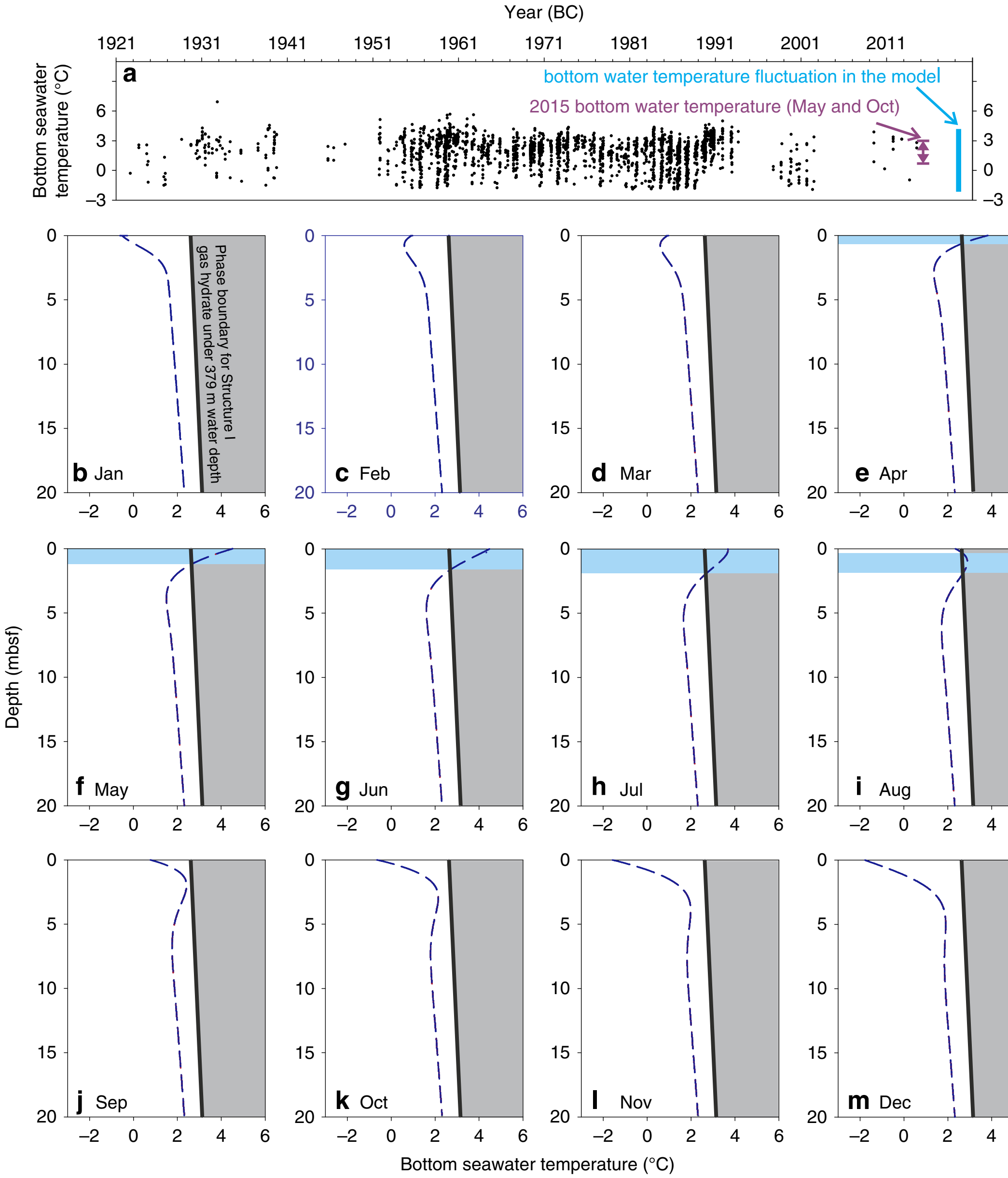

Figure 6 | Simulation of bottom seawater temperature propagation. Results of the seasonal heat propagation model with historic bottom water temperatures. (**a**) The average temperature in this area is 1.25 °C with fluctuations between −1.5 and 5 °C. (**b**–**m**) Monthly sub-bottom temperature profiles from our model. Seasonal bottom water temperature fluctuations only disturb the sub-bottom gas hydrate shallower than ~1.65 mbsf (blue area from **e**–**i**). Our recovery of gas hydrate in May and October, however suggest gas hydrate dynamics do not respond quickly to the seasonal temperature fluctuations.

sediments are still within hydrate stability field except for the top 2.3 m (Fig. 7e) over the 30-year simulation. In the case of slower warming (0.005 °C yr^{-1} for 300 years, Fig. 7f), the sub-bottom temperature for the entire sediment column can exceed hydrate stability field in two centuries (Fig. 7i). As steady increase in annual temperature over centuries is very unlikely, such estimation only reveal the minimum time required. Results from these scenarios could have been possible in the geological past with a lagging time from decades to centuries after the warming initiated based on our temperature modelling.

We observed several discrete layers of authigenic Mg-calcite nodules in five of the cores from Storfjordrenna GHMs (Fig. 2 and Supplementary Table 1). Their depleted δ^{13}C, ranging from −22.6 to −35.4‰, are consistent with anaerobic oxidation of a methane source and are similar to the carbon isotopic signature of authigenic carbonates from Barents Sea[31]. Accurate dating of their formation using U/Th dating technique is not possible due to extensive clay particle incorporation within the carbonate matrix[31]. Nonetheless, we interpret these carbonates as indicators of a prolonged and episodic methane seepage history at the GHMs. As the bicarbonate ion produced from AOM at the horizon of SMTZ diffuses both upwards and downwards, authigenic carbonates typically form around the prevailing SMTZ. Therefore, carbonates nodules immediately above and below the current depth of SMTZ likely originate from recent episodes of methane discharge. Carbonates nodules recovered deeper in the cores suggest prior seepage events such as those found well below the current SMTZ at site 1520GC (Fig. 2). On the basis of our ^{14}C dating and stratigraphy correlation (Fig. 2), the host sediments of these deep carbonate nodules can be older

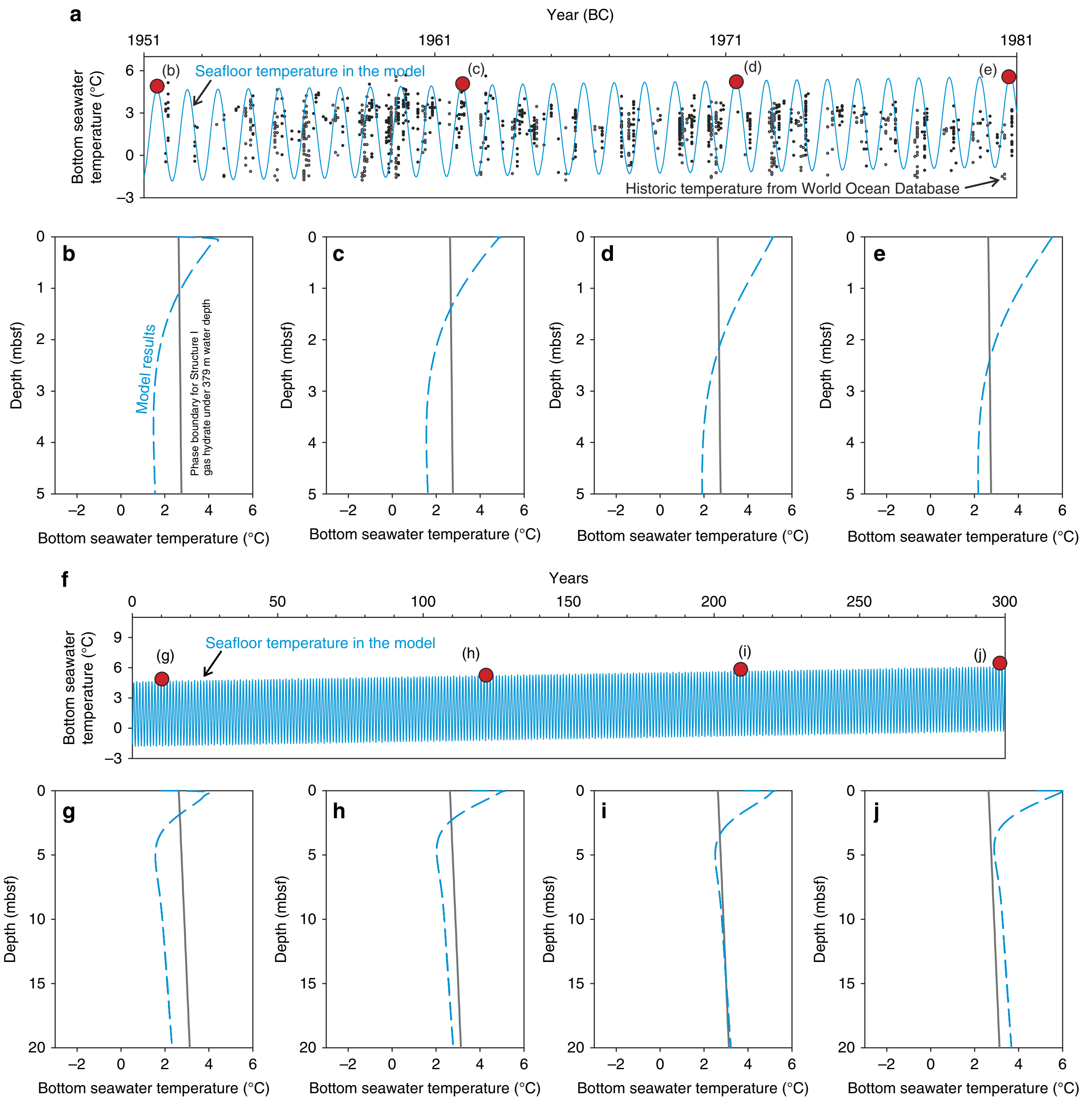

Figure 7 | Model results of heat propagation with different warming trends. We simulate the heat propagation from bottom seawater into the sediments with a fast (**a**–**e**) and a slow (**f**–**j**) bottom seawater warming cases. We assumed a 1-degree warming over the course of 30 years for the fast warming case (**a**–**e**) and a 1.5-degree warming in 300 years for the slow warming case (**f**–**j**). Four snapshots of sub-bottom temperature were shown for each case (**b**–**e**) with the time marked on (**a**) as red dots). Our assumed fast warming trend is apparently higher than the historic temperature record especially for summer seasons after *ca.* 1965. Refer to the main text for the inferences of these model results.

than Holocene. We recognize that the sediment age provides only the maximum age constraint for the formation time of the authigenic carbonate nodules. However, the presence of authigenic carbonates deep in the sediment, together with results from our porewater modelling, lead us to propose that the methane discharge in the Storfjordrenna GHMs has been occurring since at least several millenniums ago.

We postulate that the timing heterogeneity and the potentially long history of seepage can be best explained by the natural ventilation of a methane reservoir primarily modulated by pressure conditions at and beneath the GHSZ, and the opening/sealing of conduits in the sediments. Similar mechanisms for episodic methane venting events have been demonstrated to be plausible by modelling[16] and field observations[17] at other gas-hydrate-bearing margins. Alternatively, it is also likely that gas supply from the reservoir has always been strong but is continuously being redirected due to obstacles in the sediment or near the seafloor. For example, observations from the giant Regab pockmark in the Congo fan, offshore southwestern Africa, documents the development of a natural seal for the methane flow created by the formation of massive authigenic carbonate layers[15]. Future studies are required to differentiate between these potential drivers for episodic methane discharge at Storfjordrenna GHM.

The recent pursuit by the earth science community to locate areas of methane gas seepage on the seafloor is in part due to the societal concern that warming is accelerating methane leakage at high to mid-latitude regions, thereby potentially forming a feedback scenario for further warming and methane release[7]. Modelling studies that link destabilizing gas hydrate reservoirs to future warming scenarios have augmented this concern[2], lending more urgency to the search for methane bubbles entering the ocean at the seafloor. Contrary to this perspective, our findings, together with other recent studies[5,18,31–33], suggest a long history of methane release, dominantly controlled by large scale Earth system changes (for example, geology, oceanography and glaciology) with gas hydrate as a temporary methane reservoir. The role of gas hydrate should be re-assessed under a more integrated framework by taking each component of the Earth system into consideration[34]. Short-term perturbation from decadal-scale warming of the ocean may have only little consequence to the stability of gas hydrate reservoirs, as our model results suggest. The response and feedbacks between different Earth compartments and methane system[35], whether it is from gas hydrate or not, should receive rather large attention.

Methods

Porewater sampling and analyses. Porewater was sampled at ~4 °C from both multicores and gravity cores immediately after core recovery using acid-washed rhizon samplers. The samples were collected in 20 ml acid-washed syringes and subsequently filtered through 0.2 µm cellulose acetate in-line filters. Before subsampling, the porewater was stored at room temperature for ~15 min to allow for temperature equilibration. Subsamples were preserved for shorebased analyses of sulfate by adding 6 ml of a 23.8 mM $Zn(OAc)_2$ solution less than 30 min after the syringe was disconnected from the rhizon. Samples for sulfate/sulfide measurements were stored in −20 °C freezer until analysis.

For sulfate analyses, we used a Dionex ICS—1100 Ion Chromatograph outfitted with an AS-DV autosampler and an IonPac AS23 column (eluent: 4.5 mM Na_2CO_3/0.8 mM $NaHCO_3$, flow: 1 ml min^{-1}). The relative standard deviations from repeated measurements of different laboratory standards are better than 0.5% for concentrations above 0.1 mM and better than 1.8% for concentrations above 0.02 mM.

Dissolved iron was determined spectrophotometrically onboard using a ferrospectral complex in ascorbic acid (1%) at wave length of 565 nm. Calibration curves were prepared from iron sulfate standards (10 points from 0.067 to 1 mg l^{-1} Fe^{2+}) and determined before each sample batch. Standard and ferrospectral solutions were prepared daily with anoxic 18.2 MΩ MilliQ water using acid-washed volumetric flasks. Measurements were done within an hour after the water samples were extracted.

Concentrations of ΣHS were analysed by the 'Cline method'[36] onshore. Porewater samples fixed with $Zn(OAc)_2$ were well mixed before analyses. Sample (50–200 µl) were diluted to a proper concentration for the analyses. Ten to fifteen minutes after mixing the samples with the colour reagent (*N*,*N*-dimethyl-*p*-phenylenediamine sulfate salt and $FeCl_3 + 6H_2O$ dissolved in cool 18.5% reagent grade HCl), they were measured spectrophotometrically with a wave length of 670 nm. Na_2S standard was made fresh every day before analysing the samples. Thirteen standards with concentrations ranging from 0.04 to 0.25 mM were made for calibration.

TA was measured by Gran titration method a couple hours after the porewater samples were collected onboard. The HCl titrant (0.012 M) was made fresh before the cruise. Before each batch of analyses, 0.01 M borax standard and local seawater were titrated for quality control. Titration was performed in an open beaker with constant stirring. The amount of acid and pH was manually recorded during each acid addition. TA was calculated from the Gran function plots.

Concentrations of calcium and magnesium were measured by the ICP-OES (Leeman Labs Prodigy) in the W.M. Keck Collaboratory for Plasma Spectrometry at the Oregon State University in the radial viewing modes. Samples were diluted 100 times with 1% quartz-distilled nitric acid before analyses. Repeated IAPSO and in-house standard were measured for every 11 samples to assess the instrumental accuracy and precision. Mean concentrations and 1-sigma uncertainties were calculated from three replicate analyses. The uncertainties are generally lower than 1 mmol l^{-1} for magnesium and 0.1 mmol l^{-1} for calcium.

Concentrations of ammonium were determined by a colorimetric method with a Technicon AutoAnalyzer II component at the Oregon State University. The analytical detail is documented in the EPA Criteria 'EPA 600/4-79-020 Methods for Chemical Analysis of Water and Wastes' which is available online[37].

X-radiograph and X-ray fluorescence scanning. We scanned all the archived halves of the sediment cores with a GEOTEK X-ray core imaging system (MSCL-XCT 3.0) at UiT the Arctic University of Norway, using an X-ray intensity of 120 kV and a measuring resolution of 10 mm. Once we identified irregular blocks of higher density relative to the adjacent sediments from the x-radiograph, we then tested these irregular blocks with 2% HCl to confirm their calcareous nature. XRF scanning of the cores was done using the Avaatech instrumentation at UiT. Zr and Rb were quantified with 30 kV, 2,000 µA, at 10 s using Pd filter.

Mineralogy and stable carbon isotopes of carbonates. Carbonate samples were powdered and homogenized. Mineralogical analyses were performed by X-ray diffraction on un-oriented samples scanned by a Bruker D8 Advance diffractometer (Cu K_α radiation in 3–75° 2θ range). Quantitative data were obtained with the Rietveld algorithm-based code, Topas-4, provided by Bruker. Following a displacement correction of the spectrum made on the main quartz peak, the d_{104} displacement of calcite was used to estimate the $MgCO_3$ in mol% (ref. 38).

An aliquot of the powder prepared for X-ray diffraction was used for stable carbon and oxygen isotopic measurements using a GasBench II preparation line connected to a Thermo Scientific Delta V Advantage IRMS (Thermo Fisher Scientific). Carbon dioxide was produced by the reaction of the powdered sample with 103–105% concentrated phosphoric acid at 70 °C over 2 h. Reproducibility is better than ±0.15‰ for $\delta^{13}C$ values. Stable isotopic compositions are reported in conventional delta (δ) units relative to Vienna Pee Dee Belemnite reference. Values are reported in Supplementary Table 1.

^{14}C dating. About 2 mg of planktonic foraminifera (*Neogloboquadrina pachyderma*) was picked for each depth of ^{14}C dating. Their $\delta^{13}C$ values were determined at the Stable Isotope Laboratory in the Arctic University of Norway in Tromsø. before dating to ensure no influence of ancient carbon from methane precipitated as secondary carbonate overgrowth or replace the original shells of the foraminifera (Supplementary Table 2). Samples were sent to Beta Analytical for analyses. Both the radiocarbon ages and ages calibrated for local reservoir effect[39] were reported.

Phase boundary of structure I gas hydrate. We used CSMGem[1] to estimate the methane solubility (that is, maximum dissolved methane concentration with coexisting hydrate) and the thermodynamic equilibrium temperature of gas hydrate at the base of its stability zone. We assumed Structure I gas hydrate with pure methane and salinity of 35 mg g^{-1}. Stability temperature at 60 mbsf, that is, at base of GHSZ, was estimated to be 4.05 °C. We obtained a saturation value of 64 mM for average bottom water temperature (1.25 °C) and pressure (3.85 MPa) conditions. We assume this value is applicable to the shallow (~1 mbsf) gas hydrates we observed.

1-D transport-reaction model for porewater profiles. Two types of modelling were applied on porewater profiles in this work: a comprehensive transport-reaction model with full geochemical consideration and a reduced model considering only sulfate and methane. The comprehensive model was applied to investigate the nature of non-steady-state porewater profiles observed from three of the coring sites, whereas the reduced model was applied to estimate the timing of intensified methane flux at these sites.

For the comprehensive model, we coupled a FORTRAN routine, CrunchFlow[40], with a custom MATLAB routine to simulate different biological, hydrological and geological processes that may impact the porewater geochemistry. The strategy of coupling CrunchFlow with our custom MATLAB code has been proven successful in our previous work[12]. We used the porewater data from 911GC and 904MC (see Fig. 1 in the main text for location) as the constraints for deciding which scenario is most likely. A perfect fit with the observed porewater profiles is not necessary. Rather, the model should reproduce the main structure of the profiles which are: (1) bended sulfate, ΣHS, calcium, magnesium and TA profiles; (2) High Fe^{2+} only at the top cm; (3) elevated ammonium concentration throughout the core with no apparent kink as in other profiles.

Detailed mathematical formulation of reactions can be found elsewhere[41,42]. We included 12 primary and 5 secondary porewater species in the model (Supplementary Table 4). The primary and secondary species are bounded together through acid–base reactions, which also provide pH buffer to the porewater system (Supplementary Table 5). Six water-rock interactions were included to describe the precipitation/dissolution of various authigenic minerals (Supplementary Table 5). Redox pairs and other aqueous reactions are key to the overall reaction network. We included six such reactions in the model. For the redox pairs, we do not force the coupling among any of the pairs. Instead, electron transfer among the various hydrogen species (H_2, H^+ and H_2O) is the common 'currency' among all the redox reactions. For example, AOM is not strictly coupled with sulfate reduction in the model. Rather, molecular water is reduced to dissolve H_2 when methane is oxidized to the bicarbonate ion. Whichever reaction consumes dissolved H_2 will facilitate AOM. The tendency of all reactions, including water-rock reactions, are defined by the Gibbs free energy of reaction summarized in Supplementary Table 5.

Organic matter degradation is formulated as a two-step process. In the first step, hydrolysis of organic matter turns solid organic matter to glucose ($C_6H_{12}O_6$) (Supplementary Eq. 8). Fermentation then turns glucose into acetate, H_2 and bicarbonate (Supplementary Eq. 1). Acetate fuels both sulfate reduction (Supplementary Eq. 3) and methanogenesis (Supplementary Eq. 6) whereas $H_2 + HCO_3^-$ induces iron reduction (Supplementary Eq. 11), sulfate reduction (Supplementary Eq. 2) and methanogenesis (Supplementary Eq. 5). Both pathways of sulfate reduction are inhibited when Fe^{2+} concentration in the porewater is higher than 0.4 µM. Both methanogenesis pathways are also inhibited when sulfate concentration is higher than 0.4 mM. These inhibition concentrations were derived from our porewater profiles (Supplementary Table 6). When the condition permits, methane is oxidized to bicarbonate ion (Supplementary Eq. 4) which can be precipitated as authigenic carbonates, consuming calcium and magnesium (Supplementary Eq. 7). The sulfide produced from sulfate reduction will eventually form pyrite (Supplementary Eq. 9) and consumes the Fe^{2+} produced from either reduction of labile iron hydroxide (Supplementary Eq. 11) or dissolution of goethite (Supplementary Eq. 10) in the deeper sediments. We assumed a simplified pathway without considering some of the intermediate species during pyrite formation[43].

For the simulation of the five chosen scenarios, different initial conditions were assigned depending on the situation (grey lines for Scen1, Scen2 and Scen4 in Fig. 4). We applied the same top boundary condition to all scenarios, which was derived from the measurements of bottom water above the sites. No flux condition was assigned for the bottom boundary of all ions except for methane. To account for an additional methane source below the current investigated sediment column, methane was artificially generated in the deepest cell, with a governing parameter that controls the amount of methane that can enter the system.

We simulated a 3-m sediment column with 200 cells cover the first 2 m of the sediment and a 1-m cell dedicated to generate the additional methane needed in Scen4. The total simulation time varies among different scenarios: from 0.25 years (Scen1), 0.5 years (Scen2), 0.7 years (Scen5), 2.5 years (Scen4), to 900 years (Scen3). The model time for each case was determined based on the general fitting with the porewater profiles. We assumed a constant porosity (0.7) throughout the core except for Scen3, which has contrastingly low porosity (0.5) sediments depositing from the core top. Porosity was corrected for tortuosity by assigning a formation factor of 1.5 (ref. 44). Diffusion coefficients for ion were computed[45] assuming a constant temperature of 1.3 based on the average seafloor temperature in the area (Fig. 6a). We assumed a constant sedimentation rate for all scenarios (3.4E–4 m yr^{-1}) based on the average sedimentation in the area[46]. This value is slightly higher than that calculated based on the two ^{14}C dating of foraminifera from 1522GC (2.2E–4 m yr^{-1}, Fig. 2). We used the higher value as it is based on a larger data set, but note that using the lower value based on our two ^{14}C-dates does not impact our conclusion. Kinetic constants for all reactions were derived either from literature[47] or from data fitting as summarized in Supplementary Table 6.

As we simulated advection (bulk sediment burial in all cases with additional fluid advection in Scen1 and Scen5) apart from diffusion and reaction, the coupling frequency between the two software routines and the time discretization in our advection computation (Δt) are key parameters determining the numerical convergence of the results. Following the advice by Hong *et al.*[12], we decided a Δt of 0.02 years for the sediment burial in all scenarios, 0.001 years for the Δt of fluid advection in Scen1, and 0.05 years for the fluid advection in Scen5.

For our reduced 1-D transport-reaction model, we simulate a 60-m sediment column considering diffusion of dissolved methane and sulfate in addition to the consumption of both species by AOM. We consider only the water phase in our model (that is, no solid and gas phases). The governing equations are:

$$\frac{\partial C}{\partial t} = -\frac{1}{\phi}\frac{\partial F}{\partial x} + R_{\mathrm{AOM}} \tag{1}$$

$$F = -\phi D_s \frac{\mathrm{d}C}{\mathrm{d}x} \tag{2}$$

where ϕ, D_s and $\mathrm{d}C/\mathrm{d}x$ are sediment porosity (0.7), diffusion coefficient in porous media, and concentration gradient for the two target species, t is time in years, x is depth in metres below seafloor (mbsf), C is the concentration of porewater species in mol m^{-3} (volume of bulk sediments) and R_{AOM} is the AOM reaction rate in mol m^{-3} yr^{-1}. Diffusion coefficients for seawater media (D) were calculated with temperature set to be the bottom water values (0.56 °C) measured during CTD casts in May 2015. We estimated 0.0158 and 0.0301 m^2 yr^{-1} for the diffusion coefficients of sulfate and methane[45], respectively. No available information for tortuosity (θ) in this area limits the accuracy of our model results. To at least constrain the order of magnitude of our age estimation, we ran the model with tortuosity of 1.5 and 2.2, a range that covers the possible tortuosity for clayey sediments with 0.6–0.7 porosity[44]. These tortuosity values were then used to define diffusion coefficients in porous media (D_s) following:

$$D_S = \frac{D}{\theta^2} \tag{3}$$

We derive the initial conditions by progressing the model until sulfate profiles match the shallow part of the profiles at each site (Fig. 5). We use no flux boundary as the lower boundary condition for sulfate. Fixed methane concentrations were assigned at the bottom of the model frame as boundary conditions.

We did not include fluid advection induced by sediment burial and compaction as our comprehensive model results suggest no significant advection in the aqueous phase (Scen5 in Fig. 4). We solved equation (1) numerically by discretizing depth using a centreed forward finite difference scheme and time using an implicit Crank–Nicholson scheme. The depth and time discretization ($\mathrm{d}x = 0.025$ m for all three sites; $\mathrm{d}t = 0.01$ for 1520GC and 911GC; $\mathrm{d}t = 0.025$ for 940GC due to the long modelling time) were determined by running the model with progressively smaller discretization until the results were numerically stable and accurate.

We solved the R_{AOM} term in equation (1) explicitly as:

$$R_{\mathrm{AOM}} = R_{\mathrm{AOM}}^{\max}\frac{C_{\mathrm{SO_4}}}{C_{\mathrm{SO_4}} + k_{\mathrm{half-SO_4}}}\frac{C_{\mathrm{CH_4}}}{C_{\mathrm{CH_4}} + k_{\mathrm{half-CH_4}}} \tag{4}$$

where $k_{\mathrm{half-SO_4}}$ and $k_{\mathrm{half-CH_4}}$ are the half saturation constants for sulfate[48] (0.5 mol m^{-3}) and methane[49,50] (5 mol m^{-3}), respectively. $R_{\mathrm{AOM}}^{\max}$ is the theoretical maximum AOM rate obtained by fitting the sulfate profile (2 mol m^{-3} yr^{-1}). The magnitude of this value affects only the shape of profiles close to the SMTZ depth but not the rate of SMTZ migration. We assumed that AOM is the only diagenetic reaction involving sulfate and methane consumption in this first order simulation; sulfate consumption and methane production due to organic matter degradation were assumed to be not significant under the timescale investigated as these reactions are not likely to induce the dramatic change in porewater concentration gradients. There are two freely adjusted parameters in this model: boundary condition for methane concentration and the time since the inferred methane pulse initiated. The magnitude of methane flux required was constrained both by the curvature of the sulfate profiles and depth where gas hydrates and/or gas microfractures first appear. The methane flux has to be large enough to simulate AOM that can outcompete sulfate diffusion from seafloor. A methane flux that is too small will result in a sulfate profile that lacks the kink structure as observed. The methane concentration at the depth of first hydrate appearance, which should be equal to methane solubility, is an additional and independent constraint for the modelled methane profile. With methane flux being constrained, we can estimate the duration of the methane pulse required to fit the data. We also considered our results as a conservative estimation as no advection component was included. Additional sensitivity tests can be found in Supplementary Fig. 3.

1-D transport model for temperature propagation. We considered the heat propagation in a 60-m sediment column ($\mathrm{d}x = 0.025$ m and $\mathrm{d}t = 0.05$ year). The governing equations were all identical with the reduced model except for the diffusivity of heat in the bulk sediments which is defined as:

$$\kappa = \frac{\phi\lambda_w + (1-\phi)\lambda_s}{\phi\rho_w C_w + (1-\phi)\rho_s C_s} \tag{5}$$

where λ is the thermal conductivity, ϕ is porosity, C is the specific heat and ρ is density. The subscript w and s indicate water and dry sediments (assuming quartz). For water and dry sediments, we used 0.56 and 8.05 W m^{-1} K^{-1} for λ, 4.2 and 0.73 J g^{-1} K^{-1} for C, and $1.03 - 10^6$ and 2.60×10^6 g m^{-3} for ρ (ref. 51). The resulting heat diffusivity is 33.4273 m^2 yr^{-1}. We estimate the regional geothermal gradient to be 0.044 °C m^{-1}, based on an average seafloor temperature of 1.44 °C and the limit of gas hydrate stability (4.05 °C) calculated from CSMGem. This geothermal gradient is close to previously reported values (0.042–0.067 °C m^{-1} for sites in similar locations and water depth[5,52]).

Code availability. The computer code (CrunchFlow input files, database files and MATLAB routines) that support the findings of this study are available by contacting the corresponding author (W.-L.H.).

Data availability. The data that support the findings of this study are available from the corresponding author (W.-L.H.) upon reasonable request.

References

1. Sloan, Jr E. D. & Koh, C. *in Clathrate Hydrates of Natural Gases* 3rd edn. (CRC press, 2008).
2. Kretschmer, K., Biastoch, A., Rüpke, L. & Burwicz, E. Modeling the fate of methane hydrates under global warming. *Global Biogeochem. Cycles* **29,** 610–625 (2015).
3. Marín-Moreno, H., Giustiniani, M., Tinivella, U. & Piñero, E. The challenges of quantifying the carbon stored in Arctic marine gas hydrate. *Mar. Petroleum Geol.* **71,** 76–82 (2016).
4. Westbrook, G. K. *et al.* Escape of methane gas from the seabed along the West Spitsbergen continental margin. *Geophys. Res. Lett.* **36,** L15608 (2009).
5. Berndt, C. *et al.* Temporal constraints on hydrate-controlled methane seepage off Svalbard. *Science* **343,** 284–287 (2014).
6. Paull, C. *et al.* Active mud volcanoes on the continental slope of the Canadian Beaufort Sea. *Geochem., Geophys., Geosyst.* **16,** 3160–3181 (2015).

7. Smith, A. J., Mienert, J., Bunz, S. & Greinert, J. Thermogenic methane injection via bubble transport into the upper Arctic Ocean from the hydrate-charged Vestnesa Ridge, Svalbard. *Geochem. Geophys. Geosyst.* **15,** 1945–1959 (2014).
8. Andreassen, K., Hart, P. E. & Grantz, A. Seismic studies of a bottom simulating reflection related to gas hydrate beneath the continental margin of the Beaufort Sea. *J. Geophys. Res.: Solid Earth* **100,** 12659–12673 (1995).
9. Vadakkepuliyambatta, S., Bünz, S., Mienert, J. & Chand, S. Distribution of subsurface fluid-flow systems in the SW Barents Sea. *Mar. Petroleum Geol.* **43,** 208–221 (2013).
10. Andreassen, K., Hogstad, K. & Berteussen, K. Gas hydrate in the southern Barents Sea, indicated by a shallow seismic anomaly. *First Break* **8,** 235–245 (1990).
11. Hensen, C. *et al.* Control of sulfate pore-water profiles by sedimentary events and the significance of anaerobic oxidation of methane for the burial of sulfur in marine sediments. *Geochim. Cosmochim. Acta* **67,** 2631–2647 (2003).
12. Hong, W.-L. *et al.* Removal of methane though hydrological, microbial, and geochemical processes in the shallow sediments of pockmarks along eastern Vestnesa Ridge (Svalbard). *Limnol. Oceanogr.* **61,** S324–S343 (2016).
13. Hong, W.-L., Solomon, E. A. & Torres, M. E. A kinetic-model approach to quantify the effect of mass transport deposits on pore water profiles in the Krishna–Godavari basin, Bay of Bengal. *Mar. Petroleum Geol.* **58,** 223–232 (2014).
14. Borowski, W. S., Paull, C. K. & Ussler, W. Marine pore-water sulfate profiles indicate in situ methane flux from underlying gas hydrate. *Geology* **24,** 655–658 (1996).
15. Marcon, Y., Ondréas, H., Sahling, H., Bohrmann, G. & Olu, K. Fluid flow regimes and growth of a giant pockmark. *Geology* **42,** 63–66 (2014).
16. Daigle, H., Bangs, N. L. & Dugan, B. Transient hydraulic fracturing and gas release in methane hydrate settings: a case study from southern Hydrate Ridge. *Geochem. Geophys. Geosyst.* **12,** Q12022 (2011).
17. Bangs, N. L. B., Hornbach, M. J. & Berndt, C. The mechanics of intermittent methane venting at South Hydrate Ridge inferred from 4D seismic surveying. *Earth Planet. Sci. Lett.* **310,** 105–112 (2011).
18. Plaza-Faverola, A. *et al.* Role of tectonic stress in seepage evolution along the gas hydrate-charged Vestnesa Ridge, Fram Strait. *Geophys. Res. Lett.* **42,** 733–742 (2015).
19. Dypvik, H. & Harris, N. B. Geochemical facies analysis of fine-grained siliciclastics using Th/U, Zr/Rb and (Zr + Rb)/Sr ratios. *Chem. Geol.* **181,** 131–146 (2001).
20. Lucchi, R. G. *et al.* in *Submarine Mass Movements and their Consequences* 735–745 (Springer, 2012).
21. Schulz, H. D., Dahmke, A., Schinzel, U., Wallmann, K. & Zabel, M. Early diagenetic processes, fluxes, and reaction-rates in sediments of the South-Atlantic. *Geochim. Cosmochim. Acta* **58,** 2041–2060 (1994).
22. Haeckel, M., Suess, E., Wallmann, K. & Rickert, D. Rising methane gas bubbles form massive hydrate layers at the seafloor. *Geochim. Cosmochim. Acta* **68,** 4335–4345 (2004).
23. Fischer, D. *et al.* Subduction zone earthquake as potential trigger of submarine hydrocarbon seepage. *Nat. Geosci.* **6,** 647–651 (2013).
24. Tryon, M. D., Brown, K. M. & Torres, M. E. Fluid and chemical flux in and out of sediments hosting methane hydrate deposits on Hydrate Ridge, OR, II: hydrological processes. *Earth Planet. Sci. Lett.* **201,** 541–557 (2002).
25. Solomon, E. A., Kastner, M., Jannasch, H., Robertson, G. & Weinstein, Y. Dynamic fluid flow and chemical fluxes associated with a seafloor gas hydrate deposit on the northern Gulf of Mexico slope. *Earth Planet. Sci. Lett.* **270,** 95–105 (2008).
26. Tjallingii, R., Rohl, U., Kolling, M. & Bickert, T. Influence of the water content on X-ray fluorescence core-scanning measurements in soft marine sediments. *Geochem. Geophys. Geosyst.* **8,** Q02004 (2007).
27. Hennekam, R. & de Lange, G. X-ray fluorescence core scanning of wet marine sediments: methods to improve quality and reproducibility of high-resolution paleoenvironmental records. *Limnol. Oceanogr. Methods* **10,** 991–1003 (2012).
28. Kim, J. H. *et al.* Inferences on gas transport based on molecular and isotopic signatures of gases at acoustic chimneys and background sites in the Ulleung Basin. *Organic Geochem.* **43,** 26–38 (2012).
29. Boyer, T. P. *et al. World Ocean Database 2013, NOAA Atlas NESDIS 72* (eds Levitus, S & Mishonov, A.) 209 (Silver Spring, MD) http://doi.org/10.7289/V5NZ85MT (2013).
30. Skogseth, R., Haugan, P. M. & Jakobsson, M. Watermass transformations in Storfjorden. *Continental Shelf Res.* **25,** 667–695 (2005).
31. Cremiere, A. *et al.* Timescales of methane seepage on the Norwegian margin following collapse of the Scandinavian ice sheet. *Nat. Commun.* **7,** 11509 (2016).
32. Portnov, A., Vadakkepuliyambatta, S., Mienert, J. & Hubbard, A. Ice-sheet-driven methane storage and release in the Arctic. *Nat. Commun.* **7,** 10314 (2016).
33. Mau, S. *et al.* Widespread methane seepage along the continental margin off Svalbard-from Bjørnøya to Kongsfjorden. *Sci. Rep.* **7,** 42997 (2017).
34. Dickens, G. R. Rethinking the global carbon cycle with a large, dynamic and microbially mediated gas hydrate capacitor. *Earth Planet. Sci. Lett.* **213,** 169–183 (2003).
35. Steinle, L. *et al.* Water column methanotrophy controlled by a rapid oceanographic switch. *Nat. Geosci.* **8,** 378–382 (2015).
36. Cline, J. D. Spectrophotometric determination of hydrogen sulfide in natural waters. *Anal. Chem.* **21,** 1005–1009 (1969).
37. EPA, C. EPA 600/4-79-020 Methods for Chemical Analysis of Water and Wastes http://www.wbdg.org/ffc/epa/criteria/epa-600-4-79-020 (1983).
38. Goldsmith, J. & Graf, D. Relation between lattice constants and composition of the Ca-Mg carbonates. *Am. Mineral.* **43,** 84–101 (1958).
39. Reimer, P. J. *et al.* IntCal13 and Marine13 radiocarbon age calibration curves 0–50,000 years cal BP. *Radiocarbon* **55,** 1869–1887 (2013).
40. Steefel, C. *et al.* Reactive transport codes for subsurface environmental simulation. *Computational Geosciences* **19,** 445–478 (2015).
41. Steefel, C. I. *CrunchFlow software for modeling multicomponent reactive flow and transport. User's manual. Earth Sciences Division.* 12–91 (Lawrence Berkeley, National Laboratory, Berkeley, CA, 2009).
42. Hong, W.-L., Torres, M. E., Kim, J.-H., Choi, J. & Bahk, J.-J. Towards quantifying the reaction network around the sulfate–methane-transition-zone in the Ulleung Basin, East Sea, with a kinetic modeling approach. *Geochim. Cosmochim. Acta* **140,** 127–141 (2014).
43. Rickard, D. Kinetics of pyrite formation by the H2S oxidation of iron (II) monosulfide in aqueous solutions between 25 and 125 degrees C: the rate equation. *Geochim. Cosmochim. Acta* **61,** 115–134 (1997).
44. Manheim, Frank T. & Lee, S. in *Initial reports of the Deep Sea Drilling Project* (ed. Waterman) 663-670 (1974).
45. Boudreau, B. P. *Diagenetic Models and their Implementation: modeling Transport and Reactions in Aquatic Sediments.* 414 (Springer, 1997).
46. Rasmussen, T. L. *et al.* Paleoceanographic evolution of the SW Svalbard margin (76 N) since 20,000 14 C yr BP. *Quat. Res.* **67,** 100–114 (2007).
47. Dale, A. W., Regnier, P., Knab, N. J., Jorgensen, B. B. & Van Cappellen, P. Anaerobic oxidation of methane (AOM) in marine sediments from the Skagerrak (Denmark): II. Reaction-transport modeling. *Geochim. Cosmochim. Acta* **72,** 2880–2894 (2008).
48. Wegener, G. & Boetius, A. An experimental study on short-term changes in the anaerobic oxidation of methane in response to varying methane and sulfate fluxes. *Biogeosciences* **6,** 867–876 (2009).
49. Nauhaus, K., Boetius, A., Kruger, M. & Widdel, F. *In vitro* demonstration of anaerobic oxidation of methane coupled to sulphate reduction in sediment from a marine gas hydrate area. *Environ. Microbiol.* **4,** 296–305 (2002).
50. Vavilin, V. Estimating changes of isotopic fractionation based on chemical kinetics and microbial dynamics during anaerobic methane oxidation: apparent zero-and first-order kinetics at high and low initial methane concentrations. *Antonie van Leeuwenhoek* **103,** 375–383 (2013).
51. Waite, W. F. *et al.* Physical properties of hydrate-bearing sediments. *Rev. Geophys.* **47,** RG4003 (2009).
52. Crane, K. *et al.* Thermal evolution of the western Svalbard margin. *Mar. Geophys. Res.* **9,** 165–194 (1988).

Acknowledgements

The authors would like to acknowledge the captains and crew members onboard *R/V Helmer Hanssen* for coring assistance, Dr Daniel J. Fornari from WHOI for operating the MISO TowCam deep-sea imaging system, and Dr Jochen Knies from the Geological Survey of Norway (NGU) for the assistance on ion chromatography, and Dr Matthias Forwick from UiT for the assistance on XRF. The authors also acknowledge the lab technicians, engineers from the Department of Geology (UiT) and NGU for assistance with the analyses. Torger Grytå supported the preparation of figures. This work was supported by the Research Council of Norway through its Centres of Excellence funding scheme (project number 223259) and NORCRUST (project number 255150) as well as the US Department of Energy (DE-FE0013531). M.E.T. acknowledges additional support through a fellowship from the Hanse Wissenschaftskolleg, Germany.

Author contributions

W.-L.H. collected porewater samples, performed X-ray and XRF analyses, and developed the simulation for sulfate profiles and heat propagation. M.E.T. contributed porewater sampling, analyses, and the design of porewater modelling. J.C. supported the overall analyses and contributed to the construction of the manuscript. A.C. performed the analyses of sulfate concentration, carbonate mineralogy and stable carbon isotopes. G.P. provided carbonate samples and assist the establishment of age model for the investigated cores. H.Y. prepared the materials for ^{14}C dating and assist the establishment of age model for the investigated cores. P.S. contributed the bathymetry and chirp data as well as the interpretation of these data. All authors contributed to the discussion of the paper at different stages.

Additional information

Supplementary Information accompanies this paper at http://www.nature.com/naturecommunications

Competing interests: The authors declare no competing financial interests.

How to cite this article: Hong, W.-L. *et al.* Seepage from an arctic shallow marine gas hydrate reservoir is insensitive to momentary ocean warming. *Nat. Commun.* **8,** 15745 doi: 10.1038/ncomms15745 (2017).

nature COMMUNICATIONS

DOI: 10.1038/ncomms16126 OPEN

Erratum: Seepage from an arctic shallow marine gas hydrate reservoir is insensitive to momentary ocean warming

Wei-Li Hong, Marta E. Torres, JoLynn Carroll, Antoine Crémière, Giuliana Panieri, Haoyi Yao & Pavel Serov

Nature Communications 8:15745 doi: 10.1038/ncomms15745 (2017) Published 7 Jun 2017; Updated 30 Jun 2017

The financial support for this Article was not fully acknowledged. The Acknowledgements should have included the following:

The publication charges for this article have been funded by a grant from the publication fund of UiT The Arctic University of Norway.